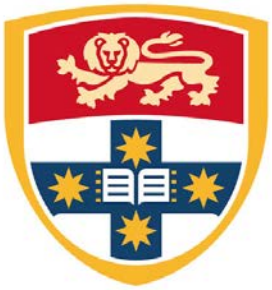

THE UNIVERSITY OF SYDNEY

Patient-specific Design of the Right Ventricle to Pulmonary Artery Conduit via Computational Analysis

By

Pegah Ebrahimi

A THESIS SUBMITTED IN FULFILMENT OF THE REQUIREMENTS FOR THE DEGREE OF MASTER OF PHILOSOPHY

In

The School of Chemical and Biomolecular Engineering
The University of Sydney

May 2019

Declaration

I declare that the work presented in this thesis is, to the best of my knowledge original, except as acknowledged in the text, and has not been submitted for another degree at any other university before.

Pegah Ebrahimi

May 2019

Ethical approvals for using human retrospective clinical data

All the cross-sectional imaging data and cardiac ultrasounds utilised in the study were obtained from imaging performed for routine clinical indications. Information was supplied in electronic form and provided by medical staff after de-identification of DICOM files. Patient information were obtained from the medical records, as well as Departmental databases within the Heart Centre at The Children's Hospital at Westmead. Only de-identified information was stored, within a secure Excel spread sheet on the restricted access Kids Heart Research 'K drive' accessible only by approved investigators.

A comprehensive protocol was submitted to The Sydney Children's Hospital Network Ethics Committee, and ethical approvals have been granted with the project identifier 2018/ETH00683.

List of publications

Journal paper

1. Iman Manavitehrani, Pegah Ebrahimi, Irene Yang, Sean Daly, Aaron Schindeler, Akshat Saxena, David G Little, David F Fletcher, Fariba Dehghani, David S Winlaw, “Current Challenges and Emergent Technologies for Manufacturing Artificial Right Ventricle to Pulmonary Artery (RV-PA) Cardiac Conduits”, Journal of Cardiovascular Engineering and Technology, published online February 2019. DOI: 10.1007/s13239-019-00406-5.

Conference presentations

1. Pegah Ebrahimi, Farshad Oveissi, Iman Manavitehrani, Sina Naficy, Fariba Dehghani, David F Fletcher, David S Winlaw, “In Silico Modelling of Existing and Ideal Right Ventricle to Pulmonary Artery Conduits”, Oral presentation at NIH Cardiovascular Bioengineering (CVBE) Symposium, March 2019, Sydney, Australia.

2. Pegah Ebrahimi, Iman Manavitehrani, David Youssef, Aeryne Lee, Farshad Oveissi, Sina Naficy, Julian Ayer, David F Fletcher, Fariba Dehghani, David S Winlaw, “Design of Optimal Right Ventricle to Pulmonary Conduits for Use in Surgery for Congenital Heart Disease”, won poster competition at Heart Valve Society (HVS) meeting, April 2019, Sitges, Barcelona.

Acknowledgements

I would like to express the deepest appreciation to my supervisors Professor David Fletcher and Professor David Winlaw for their unwavering support, guidance, and insight throughout this research project. The door to Professor Fletcher's office was always open to all students when they had questions or ran into a trouble spot. Professor Winlaw's immense knowledge, expertise, and professional attitude was very enlightening for me.

I would like to acknowledge all the collaborators and team members, without the support of whom this interdisciplinary project would not have been possible. My sincere thanks go to Dr Iman Manavi-Tehrani, who guided me through the initial stages of the research. In addition, a thank you to Dr Gananjay Salve, Dr David Youssef, and Dr Julian Ayer of the Heart Centre for Children, The Children's Hospital at Westmead, for their assistance and expert inputs on the clinical side of the project.

I would also like to express my gratitude to the tissue engineering team members at the School of Chemical and Biomolecular Engineering, The University of Sydney: Farshad Oveissi, Dr Sina Naficy, Dr Loan Le, Aeryne Lee, and above all Professor Fariba Dehghani.

I would also like to thank the staff of School of Chemical and Biomolecular Engineering at The University of Sydney, and The Children's Hospital at Westmead for providing an encouraging and a friendly environment.

Finally, it is with immense gratitude that I acknowledge all my close friends and family, who have always believed in me and encouraged me through this rewarding and enriching process. My parents and grandparents, who were my first role models and supporters in seeking knowledge, my aunt and uncle, who selflessly supported me through all the transformations of moving from my home country, and my loving brother for always boosting my morale.

Abstract

Cardiovascular prostheses are routinely used in surgical procedures to address congenital malformations, for example establishing a pathway from the right ventricle to the pulmonary arteries (RV-PA) in pulmonary atresia and truncus arteriosus. Currently available options including homograft (human donor) and xenograft (animal products) have limited biocompatibility and durability, and their fixed size necessitates multiple subsequent re-operations to upsize the conduit to match the patients' growth and address structural deterioration of the valved conduit. Moreover, the pre-set shape of these implants increases the complexity of operation to accommodate patient specific anatomy. The ultimate goal of the research group is to address these limitations by 3D printing geometrically customised implants with growth capacity.

This study addresses design aspects of this goal with material science aspects being addressed by other researchers. It is sought to integrate tissue engineering techniques with modern medical imaging and image processing tools, together with mathematical modelling. In this study, patient-specific geometrical models of the heart were constructed by performing segmentation on MRI data of patients using Mimics inPrint 2.0. Segmentation is a method of constructing the shape of the region of interest by defining its boundaries. Computational Fluid Dynamics (CFD) analysis was performed, using ANSYS CFX, to design customised geometries with better haemodynamic performance. Material design was also modified by feedback from computational modelling, using ANSYS Mechanical, of various material characteristics.

CFD simulations showed that customisation of a replacement RV-PA conduit can improve the haemodynamic performance of the implant, which may reduce right ventricular work and improve durability by minimising biomechanical stresses. For example, it was demonstrated in

this study that the mechanical energy dissipation and wall shear stress can be significantly reduced by optimising design. Finite Element modelling also allowed prediction of the optimised thickness of a synthetic material to replicate the behaviour of pulmonary artery wall under arterial pressures. This has helped by eliminating potentially costly and time-consuming experiments, largely based on trial-and-error, with as much work done *in silico* as possible.

In conclusion, we have demonstrated that patient-specific design is feasible and that derived designs are likely to improve the flow dynamics of the novel RV-PA connection. Modelling also provides information relevant to optimisation of the novel biomaterial. In time, 3D printing a customised implant may simplify replacement procedures and potentially reduce the number of operations required over a life time, bringing substantial improvements in quality of life to patients with RV-PA conduits.

Table of contents

List of tables

List of figures

1 Introduction

1.1 Background

Congenital heart disease (CHD) is an abnormality affecting the structure of the heart that is present at birth. Defects can involve formation of the cardiac chambers themselves, the inflow or outflow valves, or the arteries and the veins that carry the blood to and from the heart and lungs. CHD is the most common congenital disorder in newborns with a prevalence of approximately 1% of live births [1]. About 25% of babies with CHD have a critical condition requiring surgery or other invasive procedures in their first year of life [2]. Of particular relevance to our study are the CHD subtypes pulmonary atresia with ventricular septal defect (PA/VSD) and truncus arteriosus (TA). For both conditions, procedures are required to restore continuity between right ventricle and pulmonary artery (RV-PA), usually involving placement of a valved conduit.

The conduit procedure normally takes place early in the first year of life, hence, children outgrow the implanted conduit and require replacement of the conduit later in life. Although the mortality rate has decreased significantly as a result of developments in clinical practice and technical performance, there are still long-term physiological and economic impacts on the children with these conditions [3, 4]. Imperfect haemodynamic conditions, with a common transition involving valve competence to valve incompetence and progressive narrowing of the conduit are well tolerated by the right ventricle for a long period of time. Adaptations include right ventricular hypertrophy and/or dilatation. To address this, replacement of the valved conduit is required, involving several further open-heart operations or other invasive interventions, such as catheter-based procedures.

The ideal RV-PA valved conduit implant should have close to normal haemodynamic characteristics, resistance to thrombosis, durability and freedom from structural valve deterioration (SVD), and above all, an ability to grow in proportion to the patient's somatic growth. Current implant options are homografts and xenografts, which are human tissue and

animal products, respectively. Limited supply and fixed size of the conduits are major shortcomings of homografts and to a lesser extent, xenografts. Tissue engineering (TE) seeks to address these limitations through synthesis of a biocompatible material that replicates the mechanical properties of the native tissue. Planned degradation of the biomaterial over time and replacement with host tissue may produce apparent enlargement of the RV-PA connection, although true 'growth' has yet to be realised. Tunability of the material properties and the possibility of 3D printing customised designs are additional advantages of tissue engineered conduits compared with homografts and xenografts. However, biocompatibility or non-immunogenicity remains an important issue before clinical translation of tissue engineered conduits is possible [5].

Computational models provide insights into mechanisms that may accelerate structural valve and conduit deterioration and shorten the useful life of the implanted valved conduit. In conjunction with patient-specific optimisation of design, computational models allow iterative improvements in conduit shape and impact of various novel biomaterials. Wall shear stress (WSS) and its minimisation in conduit design is central to minimisation of structural deterioration and its impact on the right ventricle.

Currently, the main determinant of the conduit diameter is body surface area (BSA), and nomograms linking 'normal' pulmonary arterial size to BSA guide surgeons in determination of 'ideal' size. As current conduits don't grow, an attempt to 'oversize' with respect to the BSA at the time of operation is usually undertaken. Factors other than simple conduit diameter, including turbulence of flow and energy loss, as well as the position of the sternum and aorta should be considered in design of conduit shape. Consideration of these factors could be expected to increase the durability and reduce right ventricular work. Reduction of right ventricular pressures will also reduce the risk of aneurysm formation in the proximal conduit. These considerations are especially important for the RV-PA implant as the pathway from the

right ventricle to the pulmonary artery is inherently convoluted due to the different antero-posterior planes that the surface of the right ventricle and pulmonary arteries are in, as well as the fixed position of the sternum and aorta that may cause geometric distortion or compression. Patient-specific modelling and simulation can therefore lead to a better design and performance as they provide insight into factors, such as mechanical energy loss, stress distribution, and flow turbulence, that are otherwise difficult to model.

Computational methods decrease the need for *in vitro* and animal tests in the design process as they provide a preliminary assessment of the performance of the prostheses by changing design factors. Simulations are much less time consuming and costly than other testing methods and the parameters in simulations can be changed effortlessly.

Moreover, integration of computational methods with current medical imaging techniques allows patient-specific design optimisation of the implants according to each individual's anatomy. It provides invaluable clinical information that streamlines diagnosis and treatment. It should be noted that these data are more reliable when the models are not oversimplified or incomplete. This is inherently challenging in clinical circumstances, due to the lack of precisely measured cardiovascular data to feed into the models, the complexity of the geometries, and the multiscale nature of the system [6].

1.2 Objectives

This study is part of a larger project with the ambition of 3D printing customised RV-PA conduits with growth capacity for use in surgery for the treatment of a subset of congenital heart diseases. The focus of this study was on developing a methodology for integration of clinical data with engineering techniques to construct patient-specific models that can be used for optimisation of the geometrical design of the conduit. Patient-specific models were constructed using the clinical data of six patients and Computational Fluid Dynamics (CFD)

analysis was employed for design modification. Structural analysis was also utilised to evaluate the performance and optimise the dimensions of a tissue engineered material developed by other team members.

1.3 Thesis structure

The remainder of this thesis is structured as follows:

- Chapter 2 (Literature review): presents a review of relevant studies on computational methods for simulating blood flow through the arteries, the geometry construction process, biological data and boundary conditions to be used in simulations.
- Chapter 3 (Methods): describes the methodology employed in this study for construction of patient-specific models to replicate blood flow through the RV-PA conduit and design customisation of the conduit. It also elaborates on the indices that have been used to evaluate the performance of the modified designs and compare them with current clinically used conduits.
- Chapter 4 (Results and discussion): compares the performance of proposed patient-specific designs of the conduit with current clinically used options using the methods developed in Chapter 3.
- Chapter 5 (Computational modelling in material assessment): describes the application of computational modelling in expediting the process of material design by providing a rapid means of performance prediction and evaluation. It also provides a comparison of initial and modified geometries using structural analysis.
- Chapter 6 presents the conclusions arising from this study and some ideas for future work.

2 Literature review

2.1 Overview

This Chapter seeks to provide a comprehensive review of advancements in computational modelling of the cardiac arteries and implants with a focus on the applications for the design of the RV-PA conduit. In section 2.2, background physiological information is provided. Computational methods for simulation of blood flow in arteries are the subject of section 2.3. The geometry construction process is presented in section 2.4. In sections 2.5 and 2.6, biological data and boundary conditions used in simulations are described. Section 2.7 reviews the performance indices that characterise the performance of the conduit. In section 2.8, similar studies on integrating medical imaging and computational modelling for design modification of cardiac implants are reviewed.

2.2 Physiology of the heart and its defects

A normal heart consists of four chambers: two atria and two ventricles. During diastole, the heart chambers are relaxed, and blood fills the two atria. During systole, the heart muscle contracts and blood is pumped from the left and right ventricles to systemic and pulmonary circulation, respectively. The systemic circulation sends oxygenated blood to the body parts and the pulmonary circulation sends deoxygenated blood to the lungs to become oxygenated. The main focus of this study is the subgroup of CHDs that require implantation of a right ventricle to pulmonary artery (RV-PA) conduit as part of the surgical pathway. Examples include truncus arteriosus and pulmonary atresia with ventricular septal defect (VSD).

Complete absence or valvar obstruction of the pulmonary artery is named pulmonary atresia (Figure 2.1A), and when a ventricular septal defect is present, interventricular mixing allows apparently normal left and right ventricular chamber development *in utero*. The survival of patients with this condition is dependent on the persistent patency of the ductus arteriosus between the aorta and the pulmonary arteries that carry the blood to the lungs [7]. In the absence

of this connection, there is profound cyanosis (low oxygen levels), often manifesting in the first hours of life.

Truncus arteriosus arises as a failure of the normal processes of separation of the systemic and pulmonary outflows, with persistence of a single outflow structure (the truncus) from the heart, feeding both the systemic and pulmonary circulations (Figure 2.1B). It is almost always associated with a VSD.

The definitive repair procedure for both PA-VSD and TA involves patch closure of the ventricular septal defect and creation of an extra-anatomic connection between the right ventricle and the pulmonary arteries, utilising a RV-PA conduit (Figure 2.1C, PA-VSD repair demonstrated). Patients benefit from a valved conduit, as the right ventricle copes better in the absence of pulmonary regurgitation.

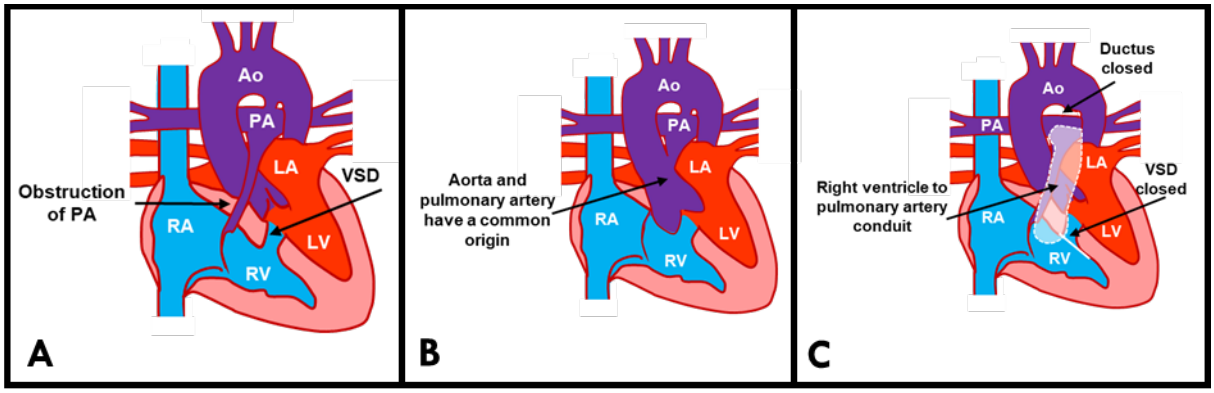

Figure 2.1 Common heart defects: (A) pulmonary atresia with VSD, (B) truncus arteriosus with VSD, (C) the combination of procedures required to repair the defects.

The proximal part of the conduit is connected to the margins of a right ventriculotomy, an incision made by the surgeon to access the ventricular septal defect through which the right ventricle will expel the blood, into the conduit, as the RV then has no other outlet. To ease the pathway from RV to the conduit, and to allow the valve to sit distally and away from potential sternal compression, a ‘hood’ is often required to roof over the connection between the RV and the conduit. Bovine pericardium is often used to create such ‘hoods’ and the technical

performance of this connection is subject to substantial variation as a result of differing patient anatomy and surgical approach. It is an example of the modifications that are required, sometimes at both ends of the conduit, to accommodate the available conduit into the individual patient. Details of the creation of RV-PA connection in truncus arteriosus are illustrated in Figure 2.2, images are taken from [8].

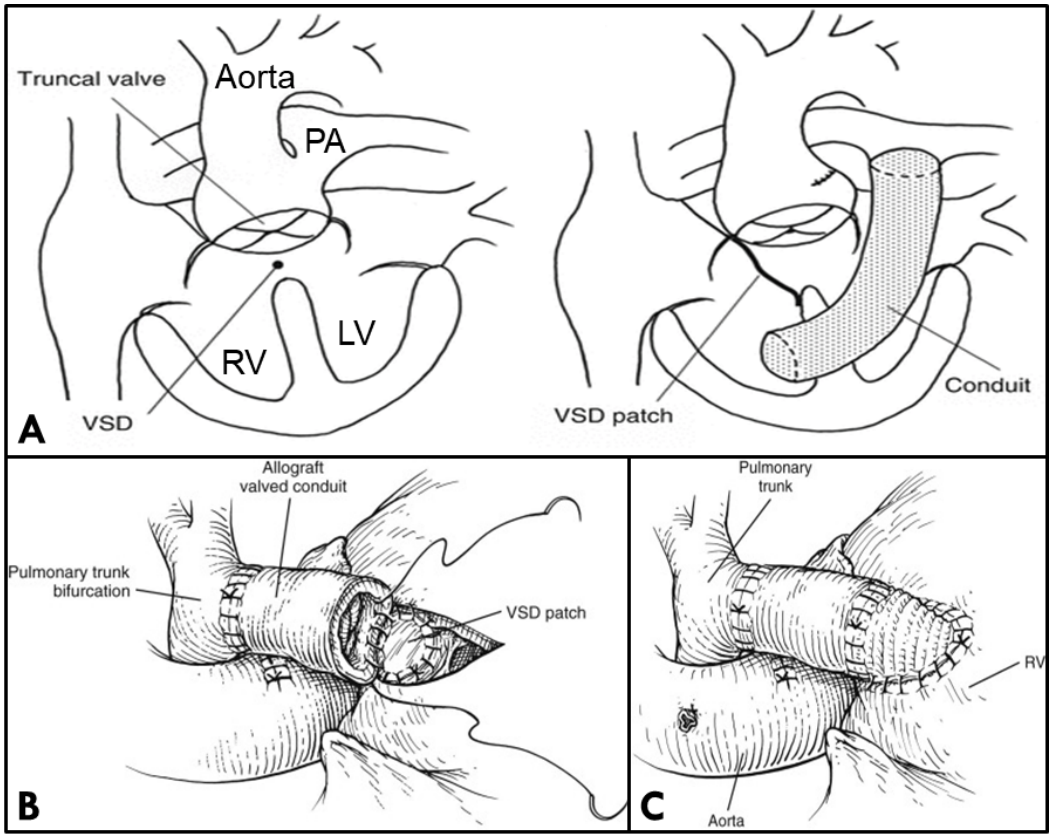

Figure 2.2 Creation of RV-PA conduit in truncus arteriosus: (A) starting pathology (on the left), repaired truncus – VSD closed and RV to PA connection made (on the right), (B) the VSD is closed through an incision in the RV and the homograft is used to create the distal part of the RV-PA pathway, (C) the pathway is completed with a patch to close over and augment the opening in the RV.

Both definitive operations may be performed in the days to weeks following birth and this is the contemporary approach to repair of TA. Conventional approaches to PA-VSD usually involves creation of a temporary source of pulmonary blood flow, either by creation of a systemic to pulmonary arterial shunt or stenting of the ductus arteriosus (not shown). This

allows deferral of the larger ‘repair’ operation for 3-9 months and may promote growth of the native pulmonary arteries.

2.3 Computational methods for simulation of blood flow in arteries

Simulation of the blood flow through the implants under physiological conditions can provide valuable insights into underlying factors that can be utilised to enhance conduit design. Computerised simulations provide information about the haemodynamic attributes, stress distributions and other data that are derived attributes and not captured through evaluation of physical structures. They assist with predicting and optimising post-operative haemodynamic characteristics and therefore enhancing the procedure outcome. In this section, a brief overview of computational methods that can be utilised for the study of the cardiovascular system is provided.

Computational techniques in modelling RV-PA conduits require these components (Figure 2.3): (1) geometry acquisition/construction (Section 2.4), (2) biological data including blood model and material model of the artery walls (Section 2.5), and (3) defining realistic boundary conditions over the cardiac cycle (Section 2.6).

In this work, CFD analysis is employed. CFD is a method for simulating fluid passing through or around an object, in this case the conduit. Generally, CFD models are based on solving the Navier-Stokes and other continuum equations; the inputs are usually flow rates, internal forces and stresses and the resulting outputs can be deformations of the vessel wall and fluid dynamics. For a very few special geometries and boundary conditions, these equations are simplified in a way that their solution can be obtained as a function of space and time using analytical methods. Otherwise, the solution generally needs to be obtained by numerical approximation, where the solving process starts from a rough estimation of the solution and an iterative algorithm is employed to modify the solution at each step. The algorithm stops when

two consecutive solutions show an insignificant change. Elaborate theory exists surrounding the stability and convergence of numerical approaches that is outside of the scope of this Section. There are several open-source and commercially-available CFD software packages that facilitate the completion of these calculations [9-11].

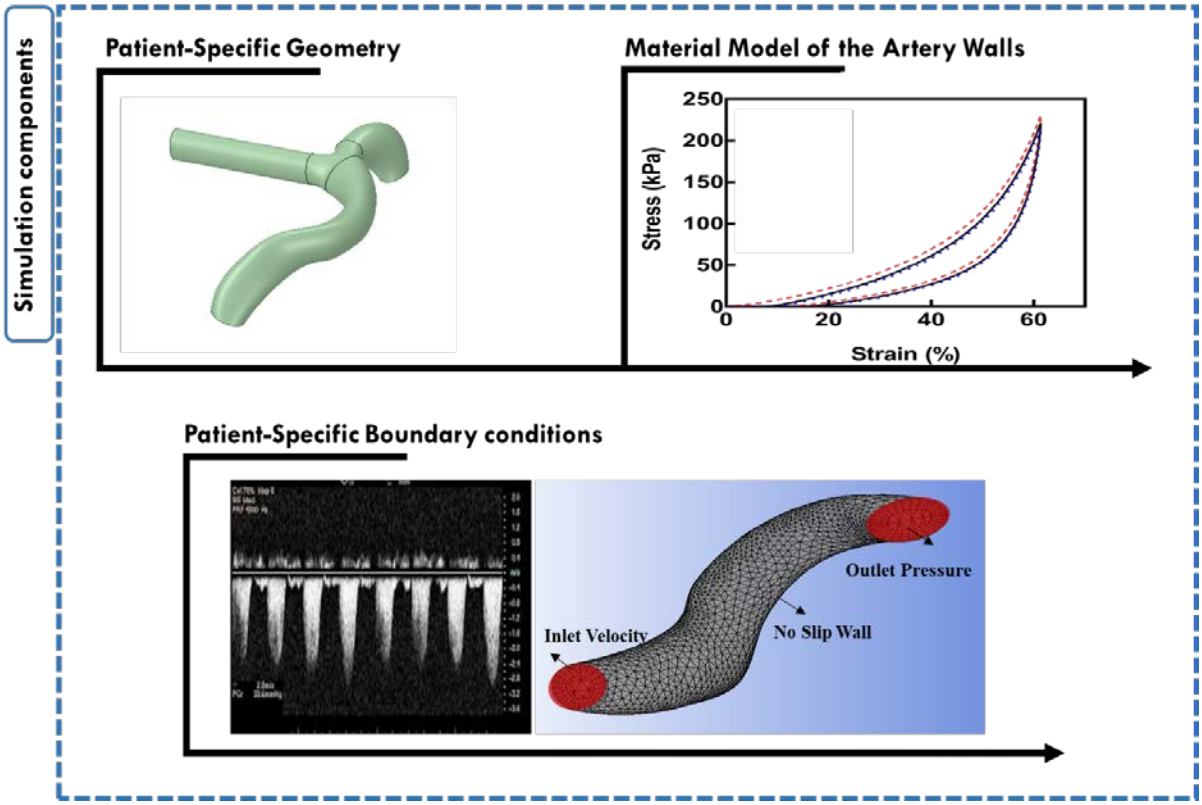

Figure 2.3 Simulation components. The patient-specific geometry in this figure is constructed from segmentation performed on a patient's MRI data (top, left). Mechanical properties of the artery walls need to be added to the model (top, right). An example of patient-specific boundary conditions is shown on the bottom. Velocity obtained from patients' echocardiogram (left) can be imposed as an inlet boundary condition (right). Selection of boundary conditions can vary in each case.

Numerical flow calculations require splitting the flow domain into many small volumes. The governing equations are then approximated and solved to provide values for each of the volumes (usually called the mesh). Various discretisation methods can be employed. Space discretisation methods are based on dividing the solution space into a finite set of points. The 'Finite Differences' approach uses a local Taylor expansion to approximate the differential

equations on the discretised points [12], and ‘Finite Volume’ method uses the integral form of the equation over discretised volumes [13].

Another set of numerical approaches are Galerkin methods, which include Spectral Methods and Finite Element analysis. These methods are based on approximating the solution by assuming it is a function of a finite set of basic functions [14]. These approaches are theoretically stronger than spatial discretisation and guarantee more accuracy, although application to complex geometry is more difficult.

Regardless of the method employed, the result will be a set of coupled, non-linear algebraic equations that are solved iteratively until convergence is obtained. For a reliable simulation practice, mesh-independence tests should be performed to ensure that the solution does not show significant changes with mesh refinement.

Researchers have also endeavoured to develop computational methods that have capabilities beyond that of traditional Finite Elements Analysis approaches. An example of these advancements is IsoGeometric Analysis (IGA) [15]. IGA uses CAD tool “NURBS” (Non-Uniform Rational B-Splines) to construct the exact geometry. The mesh is also created using NURBS elements. This eliminates the need for communication with CAD for further mesh refinements once it is constructed. Another advantage of IGA is the geometrical accuracy of the model despite the coarseness of discretisation.

In a case where a solid structure interacts with the flow, and deforms and moves according to flow, such as biological valves, a Fluid-Structure Interaction (FSI) analysis is required. This analysis is more complicated as it needs to account for transfer of information between solid and fluid subdomains (meshes). FSI algorithms can be mainly categorised as conforming mesh and non-conforming mesh approaches.

The general concept behind conforming mesh methods is dividing the region of interest into liquid and solid part and solving each part separately according to Navier-Stokes and stress-deformation equations, respectively. Here, re-meshing is required as a result of solid deformations and transformations to liquid or vice versa. The immersed boundary method [16] is the most popular of the conforming mesh approaches. Non-conforming mesh methods, however, solve the solid and fluid equations independently by adding the interactions (forces and deformations) between the fluid and the solid as terms in the momentum equation.

A major limitation of both approaches is their inability to solve problems where transitions between solid and fluid part occurs, such as blood clotting and calcification. Introduction of a mesh-free approach [17] strives to overcome this limitation by treating both solid and fluid as computational particles. The distinction between the domains, in this method, is applied by acknowledging the different forces that act on particles: pressure and viscous forces for liquid and elastic forces for the structure.

2.4 Geometry construction

The geometry construction can be done in four steps: 1) medical imaging, 2) image enhancement, 3) segmentation, and 4) meshing. Each of these steps are elaborated upon hereunder.

2.4.1 Medical imaging modalities

Angiography and ultrasound are two imaging methods that are used mostly to acquire 2D images, however reconstructing a 3D volume from 2D slices is also possible. Ultrasound exploits the reflections of high-frequency sound waves transmitted into the body to construct images. Ultrasound is the cheapest and the least invasive method of medical imaging, however, its spatial resolution is the poorest [6].

In angiography, a radio-opaque dye is injected into a small tube or catheter that is put in the body, and after the injection, pictures are taken using an X-ray machine by projecting X-ray beams on the body. Rotational angiography (RA) allows construction of 3D volumes by rotating a C-shaped arm around the subject to acquire a few hundred 2D slices. A reconstruction algorithm is then used to construct a 3D volume [18].

Another widely used technique for image acquisition based on X-ray angiography is computed tomography or CT-scan. A CT scan processes many X-ray measurements taken from multiple rotating X-ray sources and detectors using advanced reconstruction algorithms to produce many cross-sectional images of specific areas of the scanned object. Current CT devices provide sub-millimetre spatial resolution, which in combination with CFD can enable calculation of flow and pressure fields [19]. Recently, a dynamic CT has been developed that allows one to evaluate flow dynamics by constructing multiple 3D volumes through a heartbeat [20]. The drawbacks of CT include high radiation levels, which can have negative effects on patients.

Doppler echocardiography is an imaging technique that is used for acquisition of images of the cardiovascular system. Doppler echocardiography creates images of the heart by utilising high frequency ultrasonic sound waves, while the direction and the speed of blood flow is acquired using the Doppler effect. This is a non-invasive tool that provides insight into haemodynamic evaluation of the heart by allowing measurement of pressure gradients, intracardiac pressures, valve areas, regurgitant and shunt volume [21]. The major limitation of 2D echocardiography is that the measurements are angle-dependent as they are calculated under a planar flow assumption, and the ultrasound beam should be as parallel to the blood flow direction as possible, which increases the potential for user-error. Echocardiography is used clinically as a bedside tool for assessment of structure and function and is the initial modality employed to evaluate conduits serially over years of patient follow up. When significant stenosis is

identified, clinicians usually arrange a form of cross-sectional imaging (CT or MRI) to confirm expected findings and assist in surgical planning for replacement of the conduit.

Finally, cardiovascular magnetic resonance (CMR) is mentioned. CMR creates images from atomic nuclei with uneven spin in the presence of a magnetic field using radio waves. The difference between the ratio of reflected energy from various body structures is the principle MR is based on. The flexibility in tuning the RF stimuli allows elucidation of soft tissues. MR is less invasive than angiography as it does not require injecting foreign agents into the body. However, a contrast agent can be injected in the blood to enhance the quality of the images. MR is also safer than X-ray analysis and allows acquisition of highly-resolved spatial and temporal data simultaneously, which in turn enables direct 3D visualization of blood velocities, flow rate, and even WSS. Flow rate data are available in CMR since the cross-sectional area of the vessels is captured in addition to velocities. CMR does not require ionising radiation.

A variety of CMR types exist that use various physical rules to produce case-specific data. Examples are cine CMR, flow CMR, tagged CMR, DENSE CMR, etc., descriptions of which and their applications can be found in [22]. New 4D flow sequences, allow for examination of more complex fluid dynamic characteristics, such as helical flow patterns, however they require long acquisition time and complex post-processing [19]. 4D phase contrast (PC)_MRI can be used to compare the imaging data and CFD-derived velocity fields. Also, the velocity mapping resulting from PC_MRI can be applied to obtain volumetric flow measurements, detect stenotic flow, derive velocity and flow patterns, as well as vessel WSS and pulse wave velocity [23].

2.4.2 Image enhancement

Medical imaging, as with any other imaging, is prone to noise that affects the quality of the data. The main objective of image enhancement is to boost the quality of the images by

removing the noise and providing better data for future image processing. Image enhancement techniques can mainly be categorised as spatial domain and frequency domain methods.

Spatial domain methods, such as log transformation, piecewise linear transformation and power law transformation, operate directly on the pixels and enhance the contrast. Frequency domain methods, however, work with the Fourier transform of the image. Both approaches have low computational complexity. However, the frequency domain method can only focus on specific parts of the image and cannot improve the entire image. The major drawback of the spatial domain method is the lack of robustness [24]. The choice of enhancement technique is dependent on the type of noise and interference, as well as the application.

The noise in the medical images may be due to thermal effects in the signal processing electronics or other undesired sources [6]. Regardless of the source, most image processing techniques assume the noise to be additive with a zero-mean, and to have a constant variance with a Gaussian or Poisson distribution. These assumptions generally assist with simplifying the image filtering. However, to achieve a better quality of processed images, a more informed model of the noise is required. For instance, a study [25] suggests modelling noise variance by a nonlinear function of the image intensity that is dependent on parameters related to the image acquisition method.

Contrast enhancement is an important element in improving medical images, since it is the main factor that makes objects in the body separate from their surrounding structures. Algorithms such as INT Operator, Type-1 Fuzzy and Type-2 Fuzzy can be utilised to perform contrast enhancement. INT has been shown to be the most effective in simple medical images [26]. Histogram modification and tone mapping are two other contrast enhancement techniques that have been used for image processing for medical applications [24].

By the end of image enhancement process, a modified image intensity matrix is obtained that contains the image data that can be used for the next steps that lead to the construction of the geometry. Obviously, the number of points in the matrix of the enhanced image is greater than the number of points in the matrix of the initial image.

2.4.3 Image segmentation

CFD simulation can be done on a high-resolution geometrical model of the region of interest. This means that the data acquired from medical imaging should be processed and segmented to be suitable for simulation purposes. Therefore, image segmentation is a key element in the image processing steps. It is used to construct the shape of the region of interest by defining its boundary. The precise definition of the boundary is a challenging task and when working with medical images requires considerable experience and knowledge of the anatomy from the user. There are various automatic and semi-automatic approaches for segmentation that are based on different fundamental principles [22].

Thresholding is a method based on the intensity histogram of the image. It assumes that pixels belonging to the same intensity interval correspond to the same tissue, and on this assumption divides the image into several modes. This method is only effective when there is a significant gap between the intensity of the desired region of interest and its background, for instance if the target is bone. However, in most cases the intensity of different tissue types is very close, hence, thresholding needs to be combined with other approaches to improve the results.

Another technique for segmentation is region-growing that is often integrated with thresholding [27, 28]. This technique starts at a point in the image matrix and tries to find similar pixels in the neighbourhood and adds them to the region. The region stops growing when none of the points in the neighbourhood qualify for becoming a member of the region.

One of the deficiencies of this method is ‘overgrowing’ when there is similarity between target tissue and its surrounding tissue.

Pixel-voxel classification is another version of segmentation that categorises pixels in 2D or voxels in 3D based on their features (e.g., contrast, area, and circularity). To do this, a manually labelled training data set is needed, however, some methods such as K-means clustering, or expectation-maximization do not require training data. Another set of methods that are based on active contours search for target walls instead of categorizing the regions. A comprehensive review of segmentation methods can be found in [22].

Most of the abovementioned methods require user input in the form of manual segmentation on training sets or placing landmarks or specifying some boundary contours. However, automatic 3D segmentation tools, such as MITK, seg3D, and ITK-Snap, have been developed that can be used to construct geometrical models with little or no user input. The custom package CRIMSON [9] offers semi-automatic segmentation tools whereby manually constructed centrelines and two-dimensional (2D) segmentations of the vessel lumen are used to create a CAD model of the vessels of interest via lofting operations. The commercial product Materialise Mimics [29] and the open source Vascular Modelling toolkit [30] are other notable examples of semi-automatic segmentation software.

In addition, automatic 2D segmentation can be applied at several discrete locations of the interested area, which then can be lofted together using B-splines (NURBS) to produce a smooth model of the vessels that can be used for meshing. The sharp edges between branching vessels should be removed through blending techniques [31]. Another method is triangulation of the surface of the model using direct 3D segmentation, which is suitable for 3D-printing as it is lightweight.

These tools only work well in the case of high-resolution image data or they might create artefacts that then need to be repaired manually, which requires a high technical capability of the user. The intrinsic complexity of the heart, high interpatient-variability, and unavoidable imaging imperfections are some of the challenges that must be overcome before automatic segmentation can produce reliable data.

2.4.4 Meshing

Segmentation allows us to identify the boundaries of the region of interest. The next step is meshing of the volume that will make CFD modelling and finite element analysis possible. Tetrahedrons are one of the best options for meshing of medical geometries due to their flexibility in filling volumes with complex shape. Delaunay triangulation and advanced front (AF) are two main approaches for construction of unstructured tetrahedral mesh [32].

Triangulation makes a surface mesh. In AF, first a boundary surface mesh is generated. Then mesh elements are created by inserting one new point or merging different existing points. The major drawback of this approach is the complexity of the analysis of the target region and surroundings of mesh elements. Delaunay can directly generate volumetric mesh using special algorithms that are discussed in detail in [33].

The mesh quality is important in both accuracy and convergence of algorithms for the solution of the PDE of interest. There are several quality determinants that can be utilised to assess the mesh quality, such as node point distribution, smoothness, and skewness. Skewness is the most significant as it quantifies mesh distortion, which is caused by the presence of very small angles that will affect the convergence and degrade the solution accuracy.

The mesh refinement process usually continues until no significant changes in the output results is noticed. WSS is one of the important target outputs that is studied in simulations of the blood flow in the arteries. To capture WSS accurately even at low Reynold numbers [34],

employment of a boundary layer mesh is necessary [35]. Three or four layers of boundary mesh are normally adequate.

2.5 Biological data

The values of physical parameters appearing in the differential equations that describe the flow in a conduit should be determined. This can be categorised into fluid and solid properties.

2.5.1 Fluid domain

If a fluid is considered Newtonian, the flow simulation can be characterised by its density and dynamic viscosity (blood). Blood density does not noticeably deviate from an average value of 1.06 g cm^{-3}. Typical Reynolds numbers in large arteries are in the laminar range [36]. Viscosity, however, can vary between 0.03-0.04 g cm^{-1} s^{-1} [6]. But, no patient-specific measurements are usually made, and a value in this range is normally chosen.

Experimental studies, however, show that blood is a non-Newtonian fluid and it can exhibit shear thinning, thixotropic, viscoelasticity and yield stress characteristics depending on flow shear rate history [37]. However, at shear rates greater than 50 s^{-1} the blood viscosity remains constant, hence often justifying the assumption of Newtonian flow in the model [38]. The shear rate in turn depends on the size of the blood vessels and flow behaviour. Generally, shear rates in large arteries are high. However, conditions such as stenosis that lead to recirculating zones and stagnant regions cause a decrease in shear rate, which gives rise to the need for non-Newtonian modelling [39]. In addition, it is shown that the non-Newtonian properties of blood in a pulsatile flow are remarkable around the time when the velocity and velocity gradients approach zero [40].

Generalised Newtonian models are amongst the most popular models that are very efficient for modelling healthy arteries. Examples are Carreau, Carreau-Yasuda, Cross, and Powell-Eyring. For modelling capillaries and porous structures with very low shear rates, yield stress models

such as Casson, Bingham and Quemada are more suitable. Viscoelastic models, such as the Maxwell model, are the only options that are capable of including shear-thinning and stress-relaxation features of fluid. A comprehensive review of non-Newtonian blood models can be found in [36].

Studies have endeavoured to investigate the effects of using various blood models on the results of simulations of different parts of cardiovascular systems. While many of these studies conclude that non-Newtonian blood models have a significant effect on haemodynamic parameters, many find the discrepancies between the results of Newtonian and non-Newtonian simulations insignificant [37]. This reconfirms the statement that the influence of blood model on results is case-dependent. For instance, Johnston et al. [41] and Weddell et al. [42] studied femoral artery tree and coronary artery, respectively, and showed significant change in WSS distribution. However, studies on bypass arteries grafts [43], aorto-coronary bypasses [44], and abdominal aortic aneurysm [45] have shown modest changes in haemodynamic parameters.

Valencia et al. [46] suggests that a non-Newtonian model of blood flow is more relevant in modelling of a carotid artery with aneurysm. Many other studies on arteries with aneurysm [47, 48] have reached the same conclusion, therefore Ho et al. [49] suggests employing non-Newtonian model in pathological conditions.

2.5.2 Conduit material

Ideally, the implant material is durable, has the capacity to grow with the child and does not provoke an immune response in the body. A large gap exists between current options and the ideal implant, each option has their own strengths and weaknesses. Today, human pulmonary artery tissue or ‘homograft’ is commonly used for RV-PA connection. However, limited supply, especially in smaller sizes appropriate for infant procedures, has led to utilisation of substitutes from animal products that are known as xenografts [50]. An example is bovine

jugular vein (BJV) graft [51], which is popular due to its availability in a range of sizes. However, compared with homografts, xenografts may be associated with development of distal stenosis and a higher rate of infective endocarditis [52-54]. Expanded polytetrafluoroethylene (ePTFE) and polyethylene terephthalate (Dacron) are other materials that have been used for right ventricle outflow tract (RVOT) reconstruction however PTFE is not usually a valved connection and Dacron is no longer in widespread use [55, 56].

The mechanical properties of the graft material have a significant impact on its performance. Ideally the graft would replicate the behaviour of the native artery. The impedance of the vessel, which represents its resistance to pulsatile flow is a key mechanical feature of the vessel. The impedance depends on resistance to constant flow and the fluid inertance, which are constant, and the compliance of the conduit that is modifiable [57]. Hence, a compliance study can provide insight into the effectivity of the graft. Compliance expresses a dimensional change with respect to luminal pressure change and is defined by the following equation:

Equation 2.1: Compliance = $\frac{d}{2Et}$

in which *d* is the vessel diameter, *t* is the wall thickness, and *E* is the Young's modulus of the wall tissue. Compliance mismatch between the host and the graft might bring about damage to endothelial cells, increase oscillatory forces that weaken the graft, and lead to areas of relative stasis [58]. Hence, the goal is to minimise the mismatch between compliances of the native artery and the graft noting that current materials used clinically are almost always seen to be rigid at the time of explantation for structural deterioration.

The mechanical properties of the conduit material need to be included in the model. Proper definition of these properties is not an easy task, since the data measured from limited samples can hardly be generalised to all cases due to the broad range of variations. Moreover, decellularization and maintenance methods can affect the mechanical properties [59]. Even if

measurements are done on the exact same material, it is unlikely that those properties remain the same when put in the body.

There are methods for patient-specific measurement of mechanical properties. An example is elastography where elastic modulus is obtained by solving an inverse problem from the available displacement field [60]. Another method is characterisation of the arterial wall structure by estimating pulse wave velocity using MR imaging [61].

The parameters required to define mechanical properties for the model depend on the constitutive law that is used to describe the behaviour of the material. The most common parameters used are density, elasticity and incompressibility. If a linear elastic model is used, the latter two are quantified by the Young's modulus and Poisson ratio, respectively. An acceptable Poisson ratio for all options is 0.49 that is quasi-incompressible instead of the value of 0.5 that gives incompressibility and can lead to computational instability [6].

Linear elastic models, however, are only suitable if the displacement gradient is small and the stress-strain relationship is linear. This is not always the case, particularly in modelling of the valve motion, where simplistic material models can result in misleading results. Hyperelastic models are more sophisticated alternatives to linear models that have been commonly used for characterising many soft biological tissues [62, 63]. The most popular hyperelastic material model is the exponential model introduced by Fung [64]. Moreover, including anisotropic features of the material in the model can affect the stress distribution [65], which is a significant determinant in valve design. A review of material models for valve leaflets can be found elsewhere [66].

2.6 Boundary conditions

For a properly defined simulation boundary conditions should be prescribed on all inlets, outlets and walls. Boundary conditions are derived either from physical principles or medical

measurements. An example of application of physical rules is assuming fluid particles adhere to the conduit wall perfectly, therefore the velocity of the flow at boundary layer is zero. Therefore, the no-slip condition can be prescribed on the conduit wall. At the inlet and outlet of the conduit velocity or pressure data acquired from clinical measurements can be applied.

Ultrasound is a non-invasive method of acquiring boundary condition data. By exploiting the Doppler effect, the velocity of the blood in the direction of the ultrasound beam can be obtained. The velocity data can also be converted into flow rate data across a specific cross-section if required. Another non-invasive method of measuring volumetric flow rate is using thermal imaging [67]. This method exploits the convective heat transfer relationship between the flow rate and the temperature of the flowing liquid.

More elaborate boundary conditions can be employed when velocity data at several points (as opposed to single point in previous methods) on the same cross-section are available. PC_MRI is an example of where velocities at several points on the same cross-section can be decoded from images that are taken at several instants during the heartbeat.

The spatial resolution of modern PC_MRI is often lower than the appropriate mesh size. Hence, to obtain a usable boundary condition, interpolation may be needed. An advantage of 4D flow methods such as PC_MRI and 4D_CT is that they can provide information about parameters such as displacement of the conduit wall, where physical principles are already used to prescribe boundary conditions, or internal velocities. In this case, the extra information can be utilised for validation of the numerical results.

Pressure is another clinically acquired parameter that can be used as a boundary condition. This can be obtained non-invasively, using sphygmomanometer, echocardiography, applanation tonometry, or invasively, using catheterization.

Applanation tonometry (AT) extracts the shape of the central pulse pressure waveform from the radial artery and therefore overcomes the limitations of peripheral pressure measurement [68]. In the AT process, mild pressure is applied on the radial artery by placing a strain gauge pressure sensor (tonometer) over the artery. The recordings of the sensor are then transformed using validated transfer functions to calculate central pressure indices [69]. In cases where continuous monitoring of the pressure or measurement of lower pressures is required, a catheter with a transducer can be placed in the region of interest that can measure the average pressure over a cross-section.

A limitation of simultaneously prescribing time-varying velocity or pressure profile at the inlet and outlet, which is exploited in many studies, is that acquiring accurate data simultaneously at multiple outlet branches and synchronizing them is impractical. Also, the distribution of flow and pressure is part of the desired solution, and prescribing values at the outlet might prevent a realistic outcome of the simulation. Instead, applying the relationship between flow and pressure as outflow boundary condition can increase accuracy of the simulations. For this matter and in cases where sufficient clinical data are not available, reduced order or lumped parameter models are used to prescribe the boundary conditions on the region of interest.

One of the most popular lumped parameter models in cardiovascular studies is the Windkessel model [68]. This model derives an analogy between arteries and an RCR electric circuit with a series proximal resistance with a parallel arrangement of distal resistance and a capacitance. The pressure and flow in the artery are analogous to the voltage and current in an electrical circuit, respectively. These models have the capability to capture transient responses of the system. For example, a study [70] uses a RCR model and shows that this model can account for aperiodicity of the inlet waveform, which can arise from many factors such as respiration, heart rate variability, and exercise. Another study [71] compares the aortic flow resulting from

five methods of prescribing outflow boundary conditions and shows good agreement between the haemodynamic achieved by the Windkessel model and in vivo data.

Finally, another remaining restriction in surgical planning is using pre-operative flow waveforms and other clinical measurements as boundary conditions for the proposed surgical option to simulate blood flow through the new connection and calculate relevant parameters. This method is clearly limited from a physiological view.

2.7 Indices characterising the performance of cardiovascular implants

In this section, the indices that characterise the performance of the cardiovascular implants is described. An important haemodynamic element in design optimisation of implants is WSS. In human coronary arteries, WSS is correlated with clotting, haemolysis, blood damage, plaque destabilization, thrombosis, and rupture [72]. Blood clotting plays an important role in many cardiovascular complications and causes of death as relates to small vessels, including coronary vessels. Platelet activation is an indicator of blood clotting and has been shown to be a function of high WSS and exposure times [73]. Although less of a problem in larger vessels because of the larger luminal size, such sequelae of elevated wall stress are also relevant to large vessels including the RV-PA connection. A study on aortic coarctation [74] draws correlation between long-term morbidity and time-averaged WSS and oscillatory shear index. Determination of the stress distribution also identifies the points at which the implant is more susceptible to structural deterioration and hence reduced durability.

Evaluation of conduit design related to the Fontan circulation, where IVC-PA connection is required, also illustrates concepts that are relevant to the modelling in the RV-PA context. The performance of an IVC to PA connection can also be characterised by other factors, such as power loss (PL) and hepatic flow distribution (HFD). Unbalanced HFD leads to differential growth of pulmonary arteries, which in turn affects the resistance to blood flow and alters

distribution of blood to each lung [75]. PL is indicative of efficiency of the implant. It is speculated that high PL would correlate with low exercise capacity and exert high pressure on the ventricle as it needs to compensate for the lost energy.

Therefore, if the design of the implant can be improved to achieve balanced HFD, minimise PL, and optimise stress distribution to increase the durability, it may be beneficial for the patient. Furthermore, utilising computational models in the design and optimisation process, decreases the number of in-vitro experiments required to evaluate the design.

It should be noted that PL is dependent on multiple factors. A study [76] derived an indexed energy dissipation model that illuminates effects of governing variables such as cardiac output, flow split, Reynolds number, and minimum PA size on PL. Therefore, one can normalise PL to achieve an expression that is solely a function of geometrical factors, such as curvatures, angles and orientation of the vessels.

Returning to the RV-PA context, additional factors can be studied to evaluate both the performance of the conduit but also the circulatory circumstances into which a new conduit is placed. Volume-based indices such as RV ejection fraction, end-diastolic and end-systolic volumes, RV mass, and peak ejection and filling rate, and pressure-based indices can be investigated to predict the RV-PA dysfunction. However, for comprehensive assessment of RV-PA function, energy-based analyses that incorporate both pressure and volume are most reliable. Examples include the ventricular pressure-volume relationship, ventricular stroke work and efficiency.

Studies addressing the aortic valve and root complex also provide information relevant to the RV-PA context. Simulation of blood flow using CFD has given researchers more freedom to introduce case-specific energy-based indices, such as circulation energy dissipation, aortic valve energy dissipation and total TCPC energy dissipation index. In addition, emergence of

4D phased contrast MRI allows for complex blood flow visualization and calculating haemodynamic metrics, such as WSS, flow distribution, and more complex energy indices, such as turbulence kinetic energy [77, 78].

CFD and 4D-MRI can supplement each other to provide invaluable information, as 4D MRI can be used to validate CFD results and CFD can help overcome inaccuracies of 4D MRI that stem from low resolution and noise [79]. Computational modelling and 4D phase contrast MRI based methods have the advantage of being non-invasive and therefore more clinically valuable.

2.8 Similar studies

Although the number of studies that have used CFD to investigate RVOT flow dynamics are limited, many lessons can be learned from studies that have employed CFD to evaluate and optimise the geometrical design of systemic-to-pulmonary shunts, and Fontan geometries. This is because the performance metrics, such as energy efficiency and stress distribution, and the mechanisms that affect the durability of the implant, including the host response including platelet activation and potential for thrombosis, are similar in these cases. In this section, it is intended to give an overview of similar studies that have utilised patient-specific models and CFD analysis for cardiac surgical planning and implant design.

Only a few studies have used finite volume methods to predict the flow dynamics in the RV-PA conduit, specifically. Results of such simulations have shown good agreement with the observed clinical data, which proves the practicality of these methods in surgical planning [80]. A recent study [81] argues that pre-operative haemodynamic assessment of various surgical options can enhance the decision-making process provided that pre-operative boundary conditions are similar enough to post-operative states. It also highlights the contributions that

automation can make in streamlining surgical planning process. The time required for execution of each component of surgical planning is also estimated in that study.

In first stage surgery for single ventricle conditions (a related condition but different to our focus on the RV-PA connection in pulmonary atresia and truncus arteriosus), small calibre non-valved RV-PA PTFE grafts are used to create a source of pulmonary blood flow. Whilst the clinical context is very different there are learning points identified that are relevant to the surgical planning process. The radius of the RV-PA shunt has been shown to have a significant effect on pulmonary blood flow [80]. According to five geometries investigated in [82], the diameter of the graft is a stronger determinant of the fractional volume of the flow that is under pathologically high WSS, than the shape of the graft [82].

Many studies have investigated the influence of power loss and hepatic flow distribution on an implants' performance and used these two factors to achieve better designs. Soerensen *et al.* introduced a haemodynamically-optimised total cavopulmonary connection with bifurcated caval connections using equi-sized connections to both PAs (Y-shaped graft or Y-graft) [83]. It was shown using CFD with simplified geometric models that the new design with curved junctions leads to more streamlined flow paths and lower fluid mechanical power losses compared with a 1D idealised model [84]. Yang et al. focused on hepatic flow distribution (HFD) in shape optimisation of the Y-grafts [85]. The impact of the pulmonary flow split, IVC/SVC (superior vena cava) flow ratio, and SVC flaring were examined for multiple designs. A flared SVC design was preferred over unequal-sized branches due to energy loss in the latter case. The optimised designs improved HFD by 79% and 94% in two patient-specific models studied. In a later study [86], they validated the abovementioned predictions by comparing simulation-derived HFD with *in vivo* lung perfusion data of the patients undergoing the procedure. However, the clinical implications, feasibility of implantation, risk of thrombosis and growth were not investigated.

Another patient-specific study [87], compares hepatic venous flow distribution of two surgical options pre-operatively using CFD, to suggest the better option. Fourteen surgical options in terms of HFD and PL are compared, and the work suggests that aiming for the mid pulmonary artery is robust strategy in achieving a balanced HFD, however, power loss did not change significantly between various options [75]. Another study [88] proposed a Y-graft with more clinical considerations allowing it to be used in procedures without cavopulmonary bypass, be custom manufactured, and specifically modified for individual patients. This approach improved the accuracy of haemodynamic evaluation of the graft by incorporating greater level of pulmonary branching, and the effects of respiration and cardiac contraction, as well as including resistance, impedance and lumped model boundary conditions. The study took advantage of the computational tools to compare pressures, energy efficiencies, flow distributions and wall shear stress (WSS) of the Y-graft, T-junction, and offset model. It demonstrated lower Fontan pressures, increased efficiency, and improved inferior vena cava (IVC) flow distribution in the proposed Y-graft design. The use of a rigid wall in the simulations and lack of patient-specific data for validation are some limitations of this study.

In another study [89], the authors attributed the occurrence of thrombosis in one patient to low WSS and flow stasis and highlighted the effects of patient-specific factors on the performance of Y-grafts. However, thrombosis is a multifactorial problem. Also, effects of a deformable wall and suture lines involved in the grafting process were not investigated in the WSS calculations. A study of the carotid artery [90] compares the results of rigid-wall model with FSI simulation and shows larger backflow zone for the rigid-wall flow, hence highlighting the importance of accounting for deformability of the wall.

In a recent study, a new approach was developed that integrated image data acquisition, simulation-based design, and validation of simulation results through *in vitro* testing. This was used to optimise patient-specific graft designs before manufacturing based on a balanced HFD

and minimal energy loss [91]. Utilization of electro-spun tissue-engineered vascular grafts in this study increased the degrees of freedom for graft design. The WSS profile and its effect on thrombosis, along with long-term durability of the graft are yet to be investigated.

Capelli et al. [92] endeavoured to take a step towards clinical translation of FE simulations and CFD analyses by constructing patient-specific models of various CHD cases from 12 patients and validated the results of simulations against real immediate post-procedural results. Patients underwent procedures only when there was an agreement between the clinical decision and optimised surgical plan acquired from the simulations. This is one of the few studies that takes stents into account while constructing the model. Table 2.1 demonstrates model specifications and the parameters that were investigated in some of the above studies for surgical planning and design modification.

With reference to design of the valve elements, the thrombogenic response to foreign bodies also represents a major clinical challenge that is currently chiefly managed by anticoagulants [93]. Surface factors, hemostatic factors, and haemodynamic factors are the main contributors to thrombosis. Many studies on prosthetic heart valves have employed CFD to evaluate and optimise their design, yielding the optimal haemodynamic and lowest achievable risk of design-related thrombosis [94]. However, prediction of thrombotic risks demand incorporation of a fluid structure interaction to account for wall deformations and to evaluate WSS accurately.

The “Device Thrombogenicity Emulator (DTE)” has been proposed as a method that integrates numerical and experimental approaches to evaluate the design of prosthetic valves to achieve a better thrombo-resistance performance [95]. In the experimental phase, platelets are exposed to rapidly changing dynamic shear stress loading waveforms extracted from detailed numerical simulations. The extreme flow conditions are imposed and the resultant platelet activity, which

is indicative of blood clotting and thrombosis, is then measured. Similar approaches can be adopted to achieve lower risks of thrombosis in conduit geometries.

The abovementioned strategies that have been previously used for the design of Fontan and TCPC geometries apply to RV-PA conduit too. However, despite its importance, fewer studies have focused on this specific geometry. In fact, RV-PA conduit might need more investigation due to its geometrical complexity and higher flow pressures as compared with Fontan and TCPC geometries. Patient-specific design of RV-PA conduits is especially important to avoid sternal and aortal compression. However, this has been mostly neglected in previous studies. This study endeavours to address this gap. The clinical translation of studies on implant design would be possible by integration of clinical data with tissue engineering and computational modelling techniques. This study also aims to take a step towards clinical translation by utilising computational modelling for evaluating the performance of a proposed synthetic material for the conduit, hence, expediting the material design process.

Table 2.1 Details of the modeling studies performed to date

Region of study	Geometry acquisition	Simulation output	Boundary conditions	FSI*	Reference
Azygos vein, Fontan conduit, right and left pulmonary arteries, left and right innominate vein	CT imaging and CRIMSON software	HFD**	Flow and pressure data from PC-MRI and cardiac catheterization, respectively. Three element Windkessel model	no	[87]
Glenn model including pulmonary arterial branches and carotid bifurcation	Magnetic resonance angiography and cineangiography	Pressure velocity streamline WSS***	Inlet: echo-Doppler ultrasound normalised by flow from catheterization Outlet (various branches): RCR model	yes	[70]
Fontan anatomy	MRI or CT and Geomagic Studio 9.0	HFD power loss	Inlet: time-averaged flow curves Outlet: flow ratio from PC_MRI	No	[75]
Modified Blalock-Taussig shunt	Handmade according to CT	WSS pressure drop	Inlet: velocity wave form Outlet: ratio of mass flow	No	[82]
RVOT, pulmonary trunk and the proximal branch of the pulmonary arteries along with the aortic root and coronary arteries	CT or MR and Mimics, Simpleware ScanIp, VMTKLab, ITK-SNAP and OsiriX	Pressure gradients maximum velocity	Flow data from MR 2D phase contrast images and echocardiography.	No	[92]

Carotid artery	CT Mimics Solidworks	WSS pressure velocity	Inlet: typical parabolic velocity Outlet: zero static pressure Wall: no-slip	Yes	[90]
Aorta	Mimics ANSYS ICEM	Pressure flow and velocity distribution WSS	Inlet: pressure waveform and 3D velocity profiles from PC-MRI Outlet: Windkessel, fixed flow division, pressure waveform, zero pressure	No	[71]
Aorta	MRA or CT Simvascular MeshSim	Cyclic strain WSS Oscillatory shear index	Inlet: volumetric blood flow from PC_MRI Outlet: Windkessel	Yes	[74]

3 Methods

3.1 Introduction

Six patients, three with PA/VSD (patients A, B, C) and three with TA (patients D, E, F) were selected. These patients had undergone surgery that included implanting a RV-PA conduit. The aim of this Section is to describe a method for customising the geometrical design of the implant to be used for replacement of the current conduit. Patient E had already undergone replacement of the initial RV-PA connection. The age of the patients at the time of the acquisition of MRI varies between 3-10 years. The details of their clinical situation and history are abbreviated in Table 3.1.

Table 3.1 Patients' age, condition and clinical history

Patient	Age at imaging date (years)	Diagnosis	Clinical history
A	9	PA/VSD	Age of 5 days: Central shunt Age of 1 year: Redo central shunt Age of 2 years: VSD closure, RV-PA conduit (Contegra* 22 mm)
B	10	PA/VSD	Age of 2 days: Left BT shunt Age of 1 year: VSD closure, RV-PA conduit (aortic homograft 19 mm)
C	9	PA/VSD	Age of 10 days: Primary repair and RVOT patch (at another institution) Age of 1 year: RV-PA conduit (homograft 12 mm), and LPA plasty (at another institution)
D	8	TA	Age of 12 days: Repair of TA, RV-PA conduit (pulmonary homograft 10 mm)
E	6	TA/ aortic interruption (type B)	Age of 6 days: Repair of TA and interrupted aorta (Goretex** tube graft) Age of 2 years: Replacement of conduit (aortic homograft 17 mm)
F	3	TA	Age of 15 days: Repair of TA, (Non-valved Goretex tube graft 10 mm)

* Bovine jugular vein

** Expanded polytetrafluoroethylene (ePTFE)

3.2 MRI acquisitions and pre-processing

Segmentation was performed on each patients' MRI data (DICOM files) using the Mimics inPrint 2.0 and Mimics research 20.0 software to create a 3D model of the heart. The heart toolkit enabled semi-automatic segmentation using a pre-defined 5-step workflow that allows specifying landmarks on the heart chambers and main arteries (aorta and pulmonary). It should be noted that the software is designed for a normal heart. Hence, for accurate recognition and extraction of the current conduit in the heart, knowledge of the anatomy and the ability to distinguish blood flow pathways in MRI 2D images from the user was required. The resulting 3D model is generally satisfactory when the image data are of sufficiently high resolution. However, in this study, only archived imaging files were available, resulting in suboptimal resolution for semi-automatic segmentation. Hence, for all cases, manual modification of the heart regions and flow pathways on 2D images and interpolation between them were needed to ensure the accuracy of the model. Results of segmentation on data from 6 patients are shown in Figure 3.1. The models were checked by clinical colleagues for anatomical accuracy. At the end of segmentation process, various regions, namely right ventricle, left ventricle, right atrium, left atrium, aorta, pulmonary artery, and above all, RVOT including right ventricle, RV-PA conduit and pulmonary artery, were separated and saved in different files. This is important for the next step, which is geometry construction.

3.3 Geometry construction

The STL file generated from segmentation process includes the 3D model of each region in the heart. This file can be imported to ANSYS SpaceClaim for further analysis. However, this file in its original form is not useful for simulation purposes as it contains numerous segments that are not necessarily connected to each other smoothly. This will give rise to computational complexity and might lead to non-physical flows. Furthermore, including more details does not necessarily mean that the model is closer to the reality, as in the segmentation process,

these segments could have been mistakenly recognised as the blood pool due to low resolution or imperfect settings of thresholds. It should be noted that selection of threshold settings always encounters a trade-off between overgrown regions and improper extraction of the regions, due to imperfect resolution of the medical images.

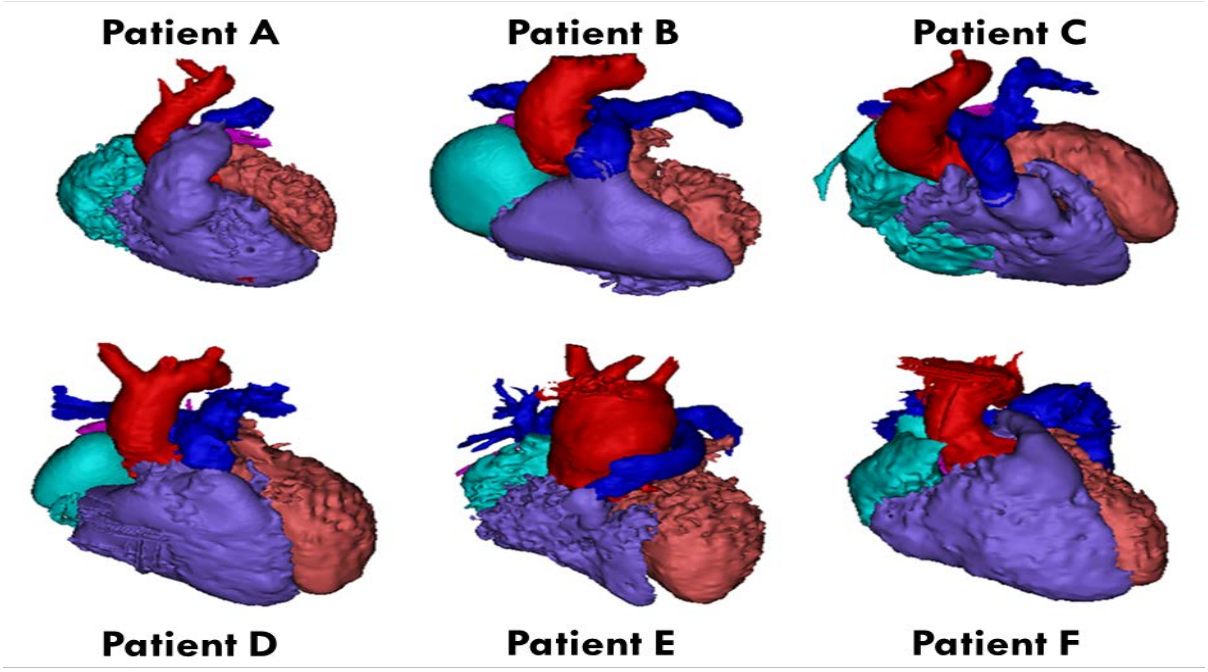

Figure 3.1 3D models of the patients' hearts created by segmentation. Top: patients with PA/VSD, Bottom: patients with TA. Green: right atrium, fuchsia: left atrium, red: aorta, peach: left ventricle, purple + blue: RVOT including right ventricle, RV-PA conduit, right and left pulmonary arteries. RVOT is the region of interest in this study. Left atrium is mostly hidden from the perspective of the model shown in this Figure.

Hence, it was necessary to make a simplified model of the conduit that utilises extract curves and has the correct dimensions, while being smooth and therefore appropriate for computational purposes. First, skin surface tools were tried, which also resulted in unnecessary details. Therefore, models were created by interpolating between several cross-sections (Figure 3.2B) of the conduit extracted from segmented models. The resulting geometries were iteratively modified to replicate the original shape. The models created by this method could approximate the original conduit shape to a satisfactory degree, while being simple and

avoiding sharp changes as much as possible (Figure 3.2B). The geometry extraction process is demonstrated in Figure 3.2. The same approach was used to include the branches in the model. The aim was to compare the performance of the current implant with a proposed modified implant. Hence, a method of enhancing the geometry was needed. The first step was choosing a suitable diameter. The appropriate choice of the diameter of the implant conduit is based on weight, height, body surface area (BSA) measurements, age, and gender.

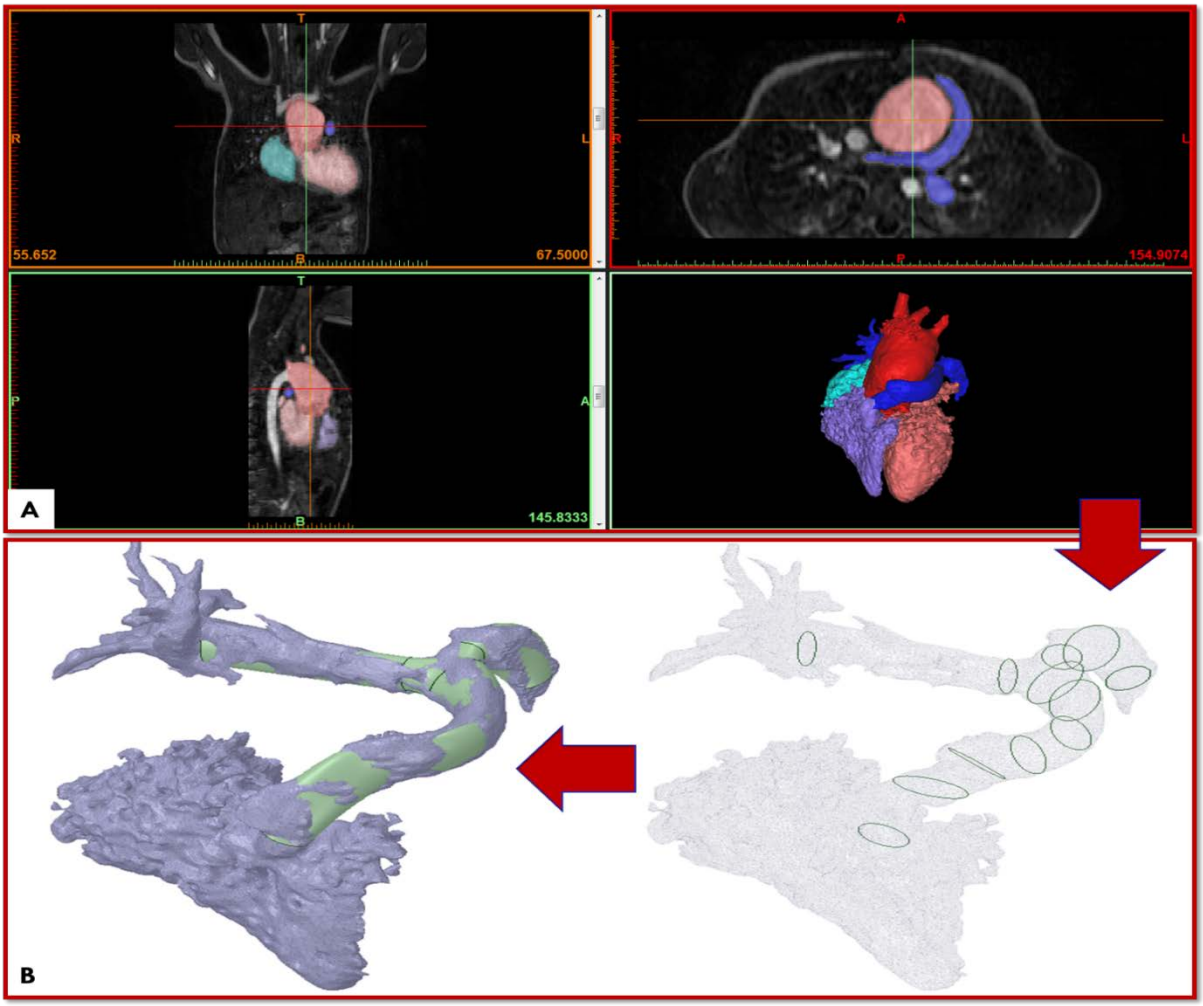

Figure 3.2 The geometry construction process. (A) Constructing 3D model of the whole heart by performing segmentation on patients' MRI. (B) Constructing conduit's geometry by interpolating between extracted cross-sections. On the right: Extracting crucial cross-sections. On the left: The constructed geometry (green geometry) shows a satisfactory approximation of the original conduit shape obtained from segmentation (grey geometry).

The diameter of the reconstructed mid pulmonary artery (MPA) can be an appropriate indicator of the diameter of the conduit. Using the method described in [96], the standard range for MPA

is calculated. Using the current diameter of MPA mentioned in MRI reports, its Z-Score is calculated. Z-score is a standardised value that indicates by how many standard deviations a value is above or below the mean in a normally distributed population. It is desirable that the Z-Score remains between –2 and 2. A Z-score above 2 or below -2 indicates too large or too small diameter, respectively. It should be noted that MPA cross-sections are mainly oval not perfect circles. Therefore, the equivalent diameter was introduced (D_{eq}) as the diameter of a circle that has the same area as the oval cross-section. When measurements vary in proximal and distal locations, the total D_{eq} is calculated by averaging proximal and distal D_{eq}. The equations are shown below.

Equation 3.1: D_{eq} of oval cross $-$ section $= \sqrt{(\text{major radius } \times \text{ minor radius})}$

Equation 3.2: $D_{eq}\ of\ MPA = \frac{\text{Proximal } D_{eq} + \text{Distal } D_{eq}}{2}$

The ultimate diameter of the modified geometry was then chosen considering two markers: the average of the proposed range using the method described in [97], and the current diameter of the conduit in the patient. The aim is to upsize the conduit commensurate with the patient's growth. The proposed diameter is calculated as below:

Equation 3.3: $\text{Proposed diameter} = \frac{3\times(\text{MPA interval average})+\text{Current } D_{eq} \text{ of MPA}}{4}$

Also, with clinical guidance, the largest diameter that was chosen was 22 mm, even if the calculation led to a higher value, since larger diameter could be clinically problematic, due to the position of aorta and sternum. The details of the parameters used in calculations and proposed diameter for each patient is demonstrated in Table 3.2. The flow split displayed in Table 3.2 shows what fraction of the flow in the MPA goes towards the right pulmonary artery (RPA) and what fraction flows through the left pulmonary artery (LPA). This information is necessary when including the branches in the model.

Table 3.2 Patient data used in diameter calculation

Patient	Height (cm)	Weight (kg)	BSA	MPA or RV-PA diameter (mm)	MPA D_{eq} (mm)	Flow Split RPA/LPA	Proposed MPA diameter range (mm)	Z-score of MPA	Proposed conduit diameter (mm)
A	128	23.6	0.909	25×34	29.2	8/92	14.57-22.6	4.25	22
B	144	34	1.159	Proximal: 8×10 Distal: 16×19	13.2	80/20	16.41-25.45	–3.9	19
C	153	49	1.445	23×29	25.8	66/34	18.28-28.35	1.12	22
D	126	25.4	0.940	Proximal: 9×10 Distal: 13×18	12.4	52/48	14.81-22.97	–3.54	18
E	112	18	0.745	11×17	13.7	64/36	13.22-20.51	–1.64	17
F	84.3	11.4	0.521	9×11	9.94	60/40	11.1-17.21	–2.98	17

The proposed method for choosing the appropriate diameter is not to be used without reviewing clinical data. For example, for patient F, the result of calculations suggested a conduit with a diameter of 13 mm, however, it was noted that this patient is only 3 years old, and since substantial somatic growth rate is expected, a diameter of 17 mm was proposed.

After choosing the appropriate diameter, centre-line of the current conduit was extracted, and constant cross-section was lofted along it. This assists with removing sharp curves and angles that might result in high shear stress and energy loss, while ensuring the pathway is physiologically feasible and is not restricted by the location of other organs. An example of an initial conduit and its associated modified geometry is shown in Figure 3.3.

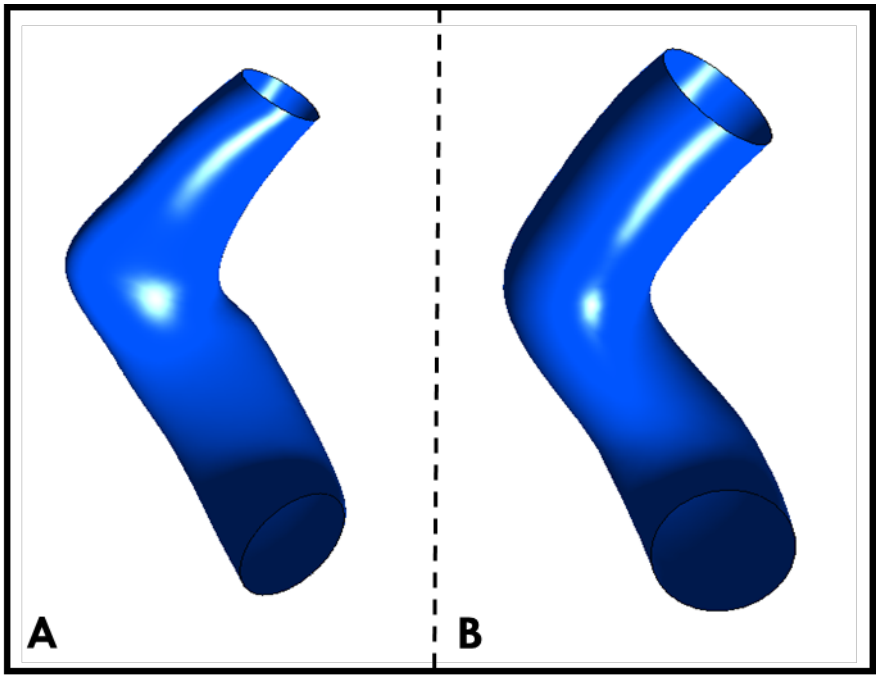

Figure 3.3 An example of geometry modification. (A) initial conduit (B) proposed geometry.

3.4 Simulation process

A patch-conforming method was used to generate the surface mesh and 5 layers of inflation with a growth rate of 1.2 and maximum thickness of 2.5 mm were applied at the walls (Figure 3.4). The target skewness was set to 0.6.

Blood flow through the geometry was assumed to be a three-dimensional, time-dependent, incompressible, laminar flow [98]. A no slip boundary condition was assigned at the walls of the conduit, and the velocity profile was imposed at the inlet. The outlet was defined as an opening and the relative pressure at the outlet was set to zero.

The area averaged velocity at various cross-sections of the conduit over time is acquired from the echocardiograms of the patients (Figure 3.5) and is converted to the mass flow rate according to the cross-section at which it was measured. The velocity at the inlet is then set to yield the calculated mass flow rate. As the full velocity data over time were not accessible, it was necessary to estimate these data. To this end, the peak positive and negative velocity and the rising and falling durations were extracted. In first attempts, the velocity curve with a triangular wave as of Figure 3.6 was approximated.

In this case, the sharp changes in the first derivative of the velocity (at peak velocities and the beginning and end of each cycle) is not physiological and causes computational instability. To address this problem, the triangular wave was approximated by the first *n* terms of its Fourier series to obtain a smoother velocity profile. The MATLAB code used for this purpose can be found in Appendix A. Figure 3.7 shows the triangular waveform estimated from echocardiogram of the test patient and the Fourier series approximations with various numbers of coefficients. As demonstrated, the difference between the curves with $n = 3$, and $n = 4$ is negligible. Hence, it sufficed to set $n = 3$, which gives a 7 term Fourier series, that was used for the test case. The number of coefficients of Fourier series that was used for each patient varies. The rule of thumb is that the number of coefficients is increased until no significant change is noticed in two consecutive series.

Lastly, output controls were set to monitor WSS and total pressure loss. As previously discussed, high WSS has been associated with luminal events and vessel instability in small vessels [72, 73]. Furthermore, the higher the energy loss, the more the ventricle needs to work to compensate for the loss of energy, which will be associated with hypertrophy and a higher oxygen consumption, and if not addressed, ultimately impairment of ventricular function. Total pressure loss is a good indicator of energy loss. Therefore, it is desirable to minimise WSS and total pressure loss.

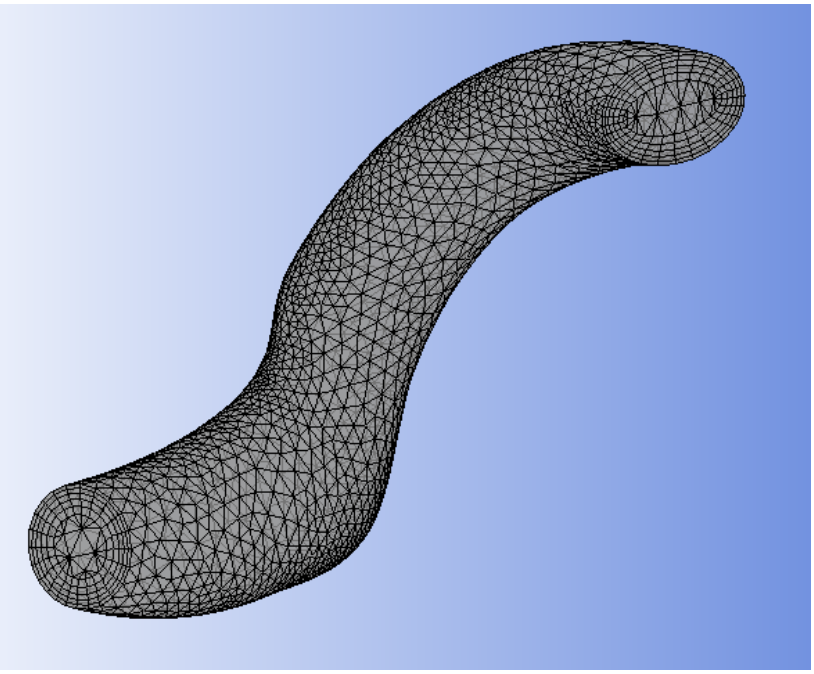

Figure 3.4 An example of meshing on one of the geometries.

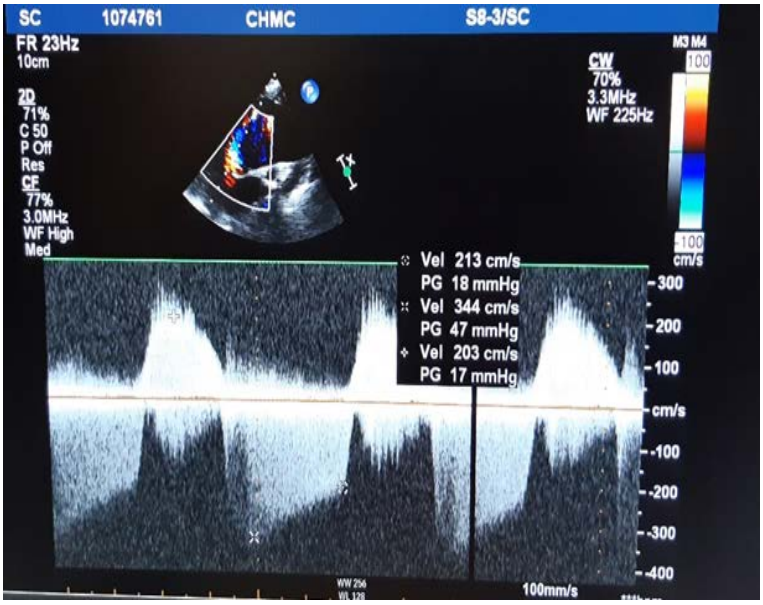

Figure 3.5 Acquisition of velocity and pressure data from echocardiogram.

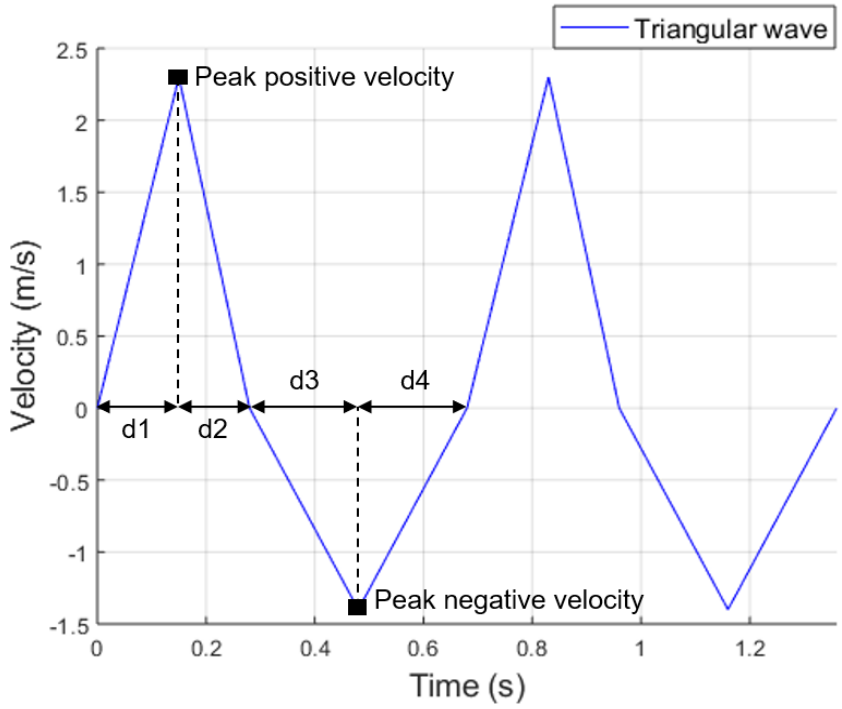

Figure 3.6 Demonstration of the parameters that define the velocity curve.

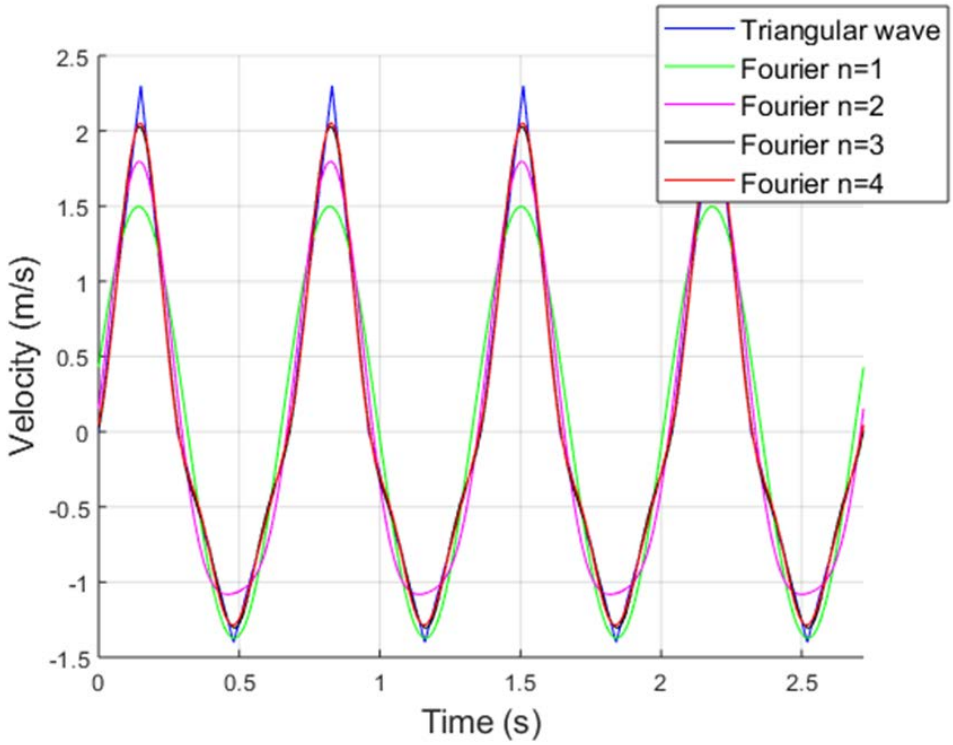

Figure 3.7 Triangular velocity waveform and its Fourier series approximation for different number of terms. In this case, $\boldsymbol{n = 3}$ provides sufficient accuracy.

3.5 Fluid domain

3.5.1 Reynolds and Womersley numbers

To justify the assumption of laminar flow, the Reynolds number ($\mathcal{R}e$) for the geometries used in this study were calculated. This dimensionless quantity was obtained from Equation 3.4 for initial and modified geometries of each patient and the results are shown in Table 3.3. Laminar flow occurs when $\mathcal{R}e < 2300$ and turbulent flow happens above this. The results in Table 3.3 shows that the Reynolds numbers are below 2300, hence, the assumption of laminar flow is valid for the cases investigated in this study.

Equation 3.4: $\mathcal{R}e = \frac{\rho u L}{\mu}$

where ρ is the density of the blood, u is the average velocity of the fluid, L is a characteristic dimension, which here is the diameter of the conduit, and μ is the dynamic viscosity of the fluid.

Table 3.3 Reynolds number for geometries included in this study

Patient	$\mathcal{R}e$ for initial geometries	$\mathcal{R}e$ for modified geometries
A	2213	1534
B	1351	1538
C	1799	897
D	2033	2125
E	252	150
F	600	1139

Womersley number (α) is another dimensionless number that characterises a flow system. It determines the ratio of the maximum flow developed for a given oscillating pressure to the corresponding steady flow, and the phase lag between the applied pressure and the flow [99].

In practice, similar magnitude of Womersley number for a given geometry in experimental studies and the patient guarantees kinematic similarity of the flow. The Womersley number determines the form of the flow, but not the magnitude.

The Womersley number was also estimated for all the geometries used in this study using Equation 3.5. The results shown in Table 3.4 show high Womersley numbers (more than 10) for most cases. High Womersley numbers mean that the frequency of the pulsatile flow is too large to allow parabolic velocity profile to be developed over a cycle. Instead, the velocity profile is relatively flat.

Equation 3.5: $\alpha = L\left(\frac{\omega\rho}{\mu}\right)^{\frac{1}{2}}$

where L is the diameter of the conduit, ω is the frequency of the oscillations, ρ is the density and μ is the dynamic viscosity of the blood.

Table 3.4 Womersley number for geometries included in this study

Patient	α for initial geometries	α for modified geometries
A	19.95	15.03
B	8.95	12.89
C	16.4	13.99
D	8.13	11.8
E	9.56	11.87
F	7.93	13.57

3.5.2 Effect of viscosity model

As mentioned before, while a Newtonian model assumes a linear relationship between the applied stress and the rate of strain of blood, non-Newtonian models take into account the

changes happening to the viscosity with shear rate. Although in reality the viscosity is not constant, in section 2.5.1, it was concluded that the significance of employing a non-Newtonian blood model on the simulation results is case dependent. Hence, both a Newtonian and a non-Newtonian blood model were tested for the case of RV-PA conduit to understand the effects of viscosity models on the results. In the case of a Newtonian model a density of 1060 kg m^{-3} and dynamic viscosity of 0.0035 Pa s [6] was applied. However, it is possibly too simplistic to assume that the blood viscosity is constant, as it varies with the shear rate. To model the non-Newtonian behaviour of the blood, the Carreau-Yasuda model is employed [100].

Equation 3.6: $\mu(\dot{\gamma}) = \mu_\infty + (\mu_0 - \mu_\infty)[1 + (\lambda\dot{\gamma})^a]^{(n-1)/a}$

where μ is the dynamic viscosity, λ is a time constant, n is the power law index, a is the Yasuda exponent, $\dot{\gamma}$ represents a scalar measure of the rate of deformation or so-called shear rate, and μ_0 and μ_∞ denote the viscosity at zero and infinity shear rate, respectively. These parameters have been experimentally obtained to be: $\mu_0 = 0.056$ Pa s, $\mu_\infty = 0.00345$ Pa s, $\lambda = 1.902$ s, $n = 0.22$, $a = 1.25$ [36].

For the test case considered here (patient E), no significant discrepancies were noticed between total pressure loss and tangential forces for the Newtonian and non-Newtonian blood model. This means that the changes in the simulation in the case of RV-PA conduit are insignificant, and Newtonian models are sufficient for capturing accurate outputs. However, for completeness, the non-Newtonian model was applied for the remainder of the study. Results of this test are shown in Figures 3.8 and 3.9. Since the water and blood have similar densities and different viscosities, the large difference between the results of water and blood models shows the effect of the liquid viscosity on pressure loss and tangential forces. Hence, the accuracy of determining the viscosity value is important.

The reason for choosing patient E as the test case was the geometrical complexity of the implanted RV-PA conduit. It is assumed that if the mesh and time-step independence are demonstrated for this case, they will be valid for the simpler geometries.

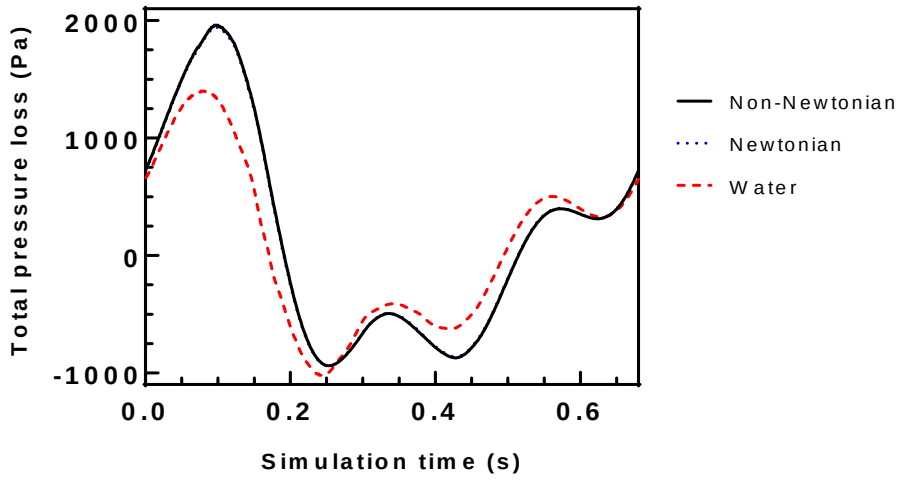

Figure 3.8 Total pressure loss over a cardiac cycle for water and Newtonian and non-Newtonian blood model.

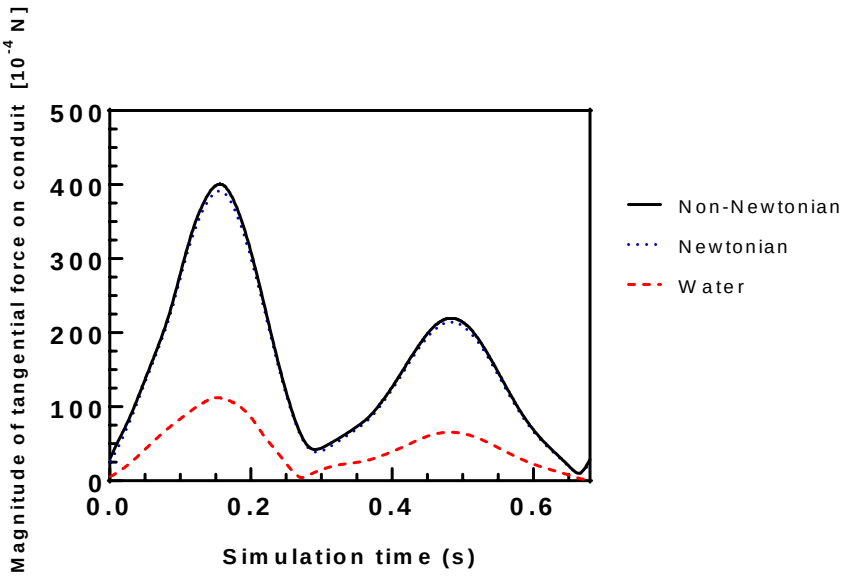

Figure 3.9 Magnitude of tangential force on conduit over a cardiac cycle for water and Newtonian and non-Newtonian blood model.

3.6 Mesh and time-step independence validation

In order to confirm mesh-independence of the simulation results, three element sizes were used, namely 2, 1.5 and 1 mm. The following parameters over a cardiac cycle were monitored: tangential forces and total pressure loss through the conduit. Figures 3.10 - 3.12 show that total pressure loss, the magnitude of the tangential force, and WSS on the conduit are very close regardless of the mesh size. Hence, mesh-independence can be concluded. Based on this study an element size of 1.5 mm was selected.

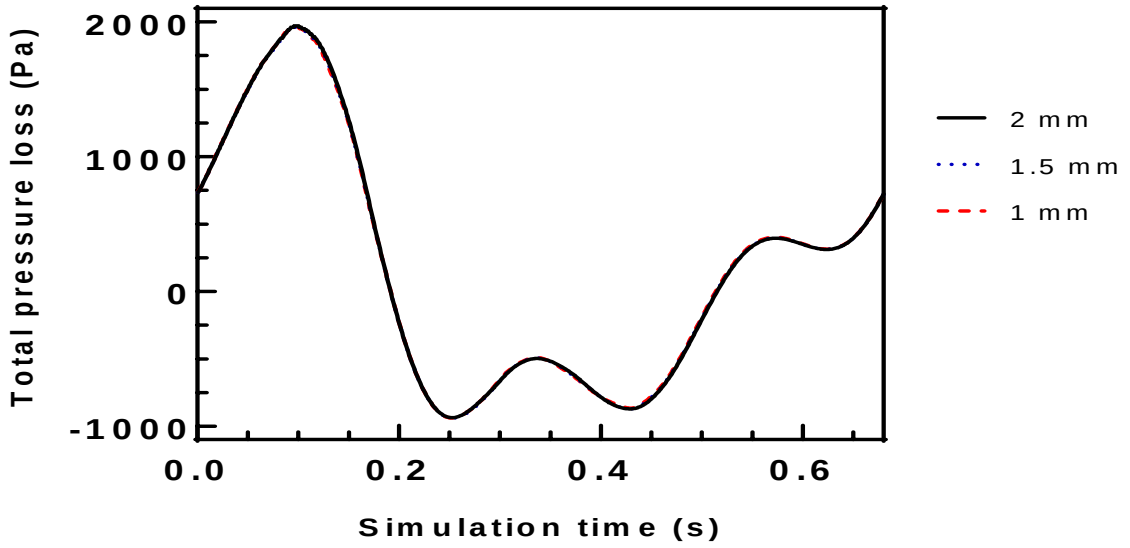

Figure 3.10 Total pressure loss over the conduit over a cardiac cycle resulting from different mesh element sizes.

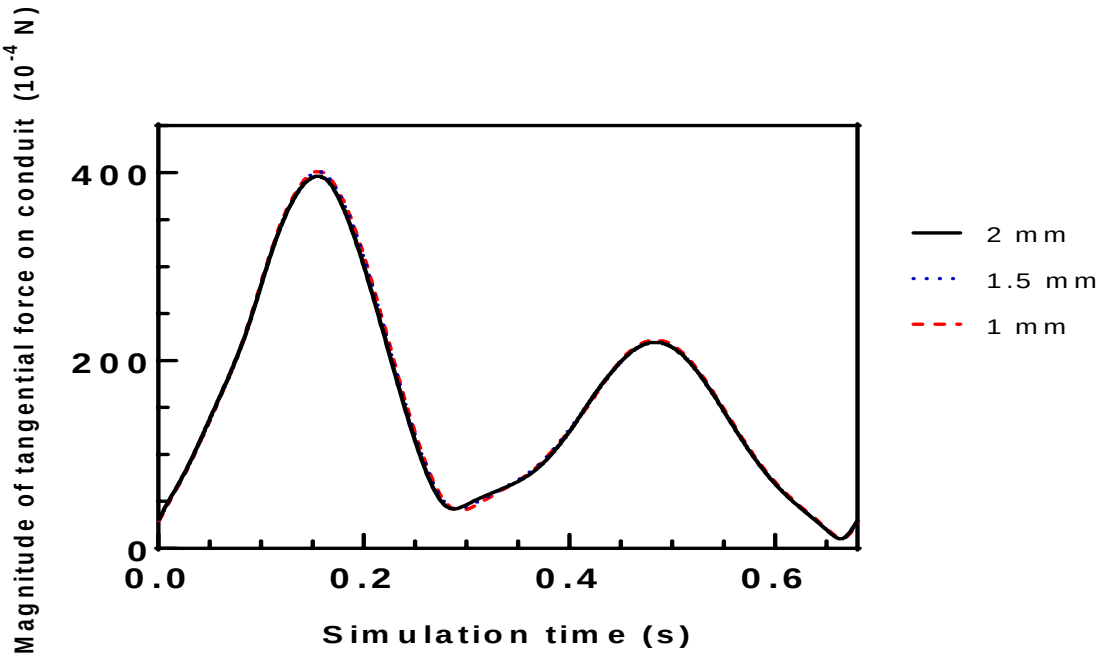

Figure 3.11 Magnitude of tangential force on the conduit over a cardiac cycle resulting from different mesh element sizes**.**

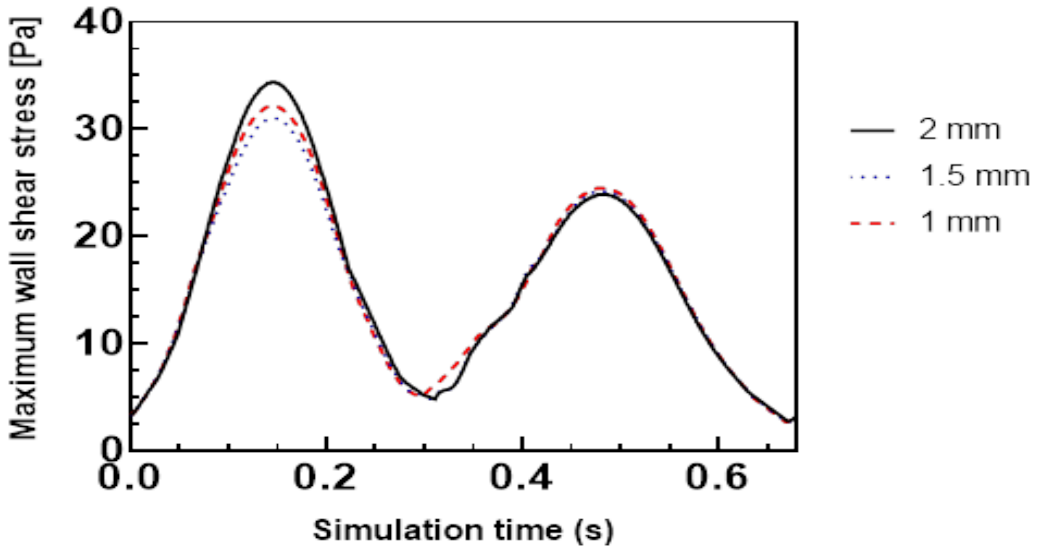

Figure 3.12 Maximum wall shear stress on the conduit over a cardiac cycle resulting from different mesh element sizes.

In addition to mesh-independence, time-step independence of the results needs to be established to ensure the computational validity of the results. To this end, with the mesh size of 1.5 mm that was obtained from the mesh-independence test, simulations were performed using varying time steps of 0.5, 1 and 2 ms. In order to confirm that all the simulations lead to same results, the same parameters as for mesh-independence test were monitored: tangential forces on the walls and total pressure loss through the conduit over a cardiac cycle. In all cases, the second cardiac cycle, which for the test case is from 0.68-1.36 s is demonstrated. This is due to the fact that at the beginning of the first cycle of the simulation, some instability in the results is always noticed at start-up. From Figures 3.13 and 3.14 it can be seen that there is no significant change in the abovementioned output monitors for selected time-step sizes. Therefore, time-step independence can be concluded, and from here on a time-step size of 1 ms is selected for all simulations.

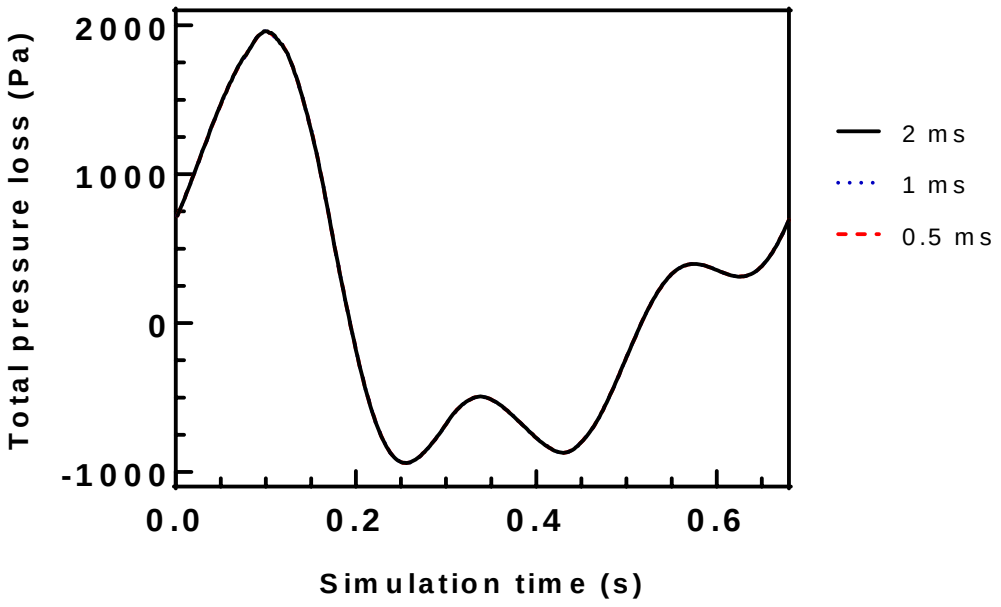

Figure 3.13 Total pressure loss over the conduit over a cardiac cycle resulting from different time-step sizes.

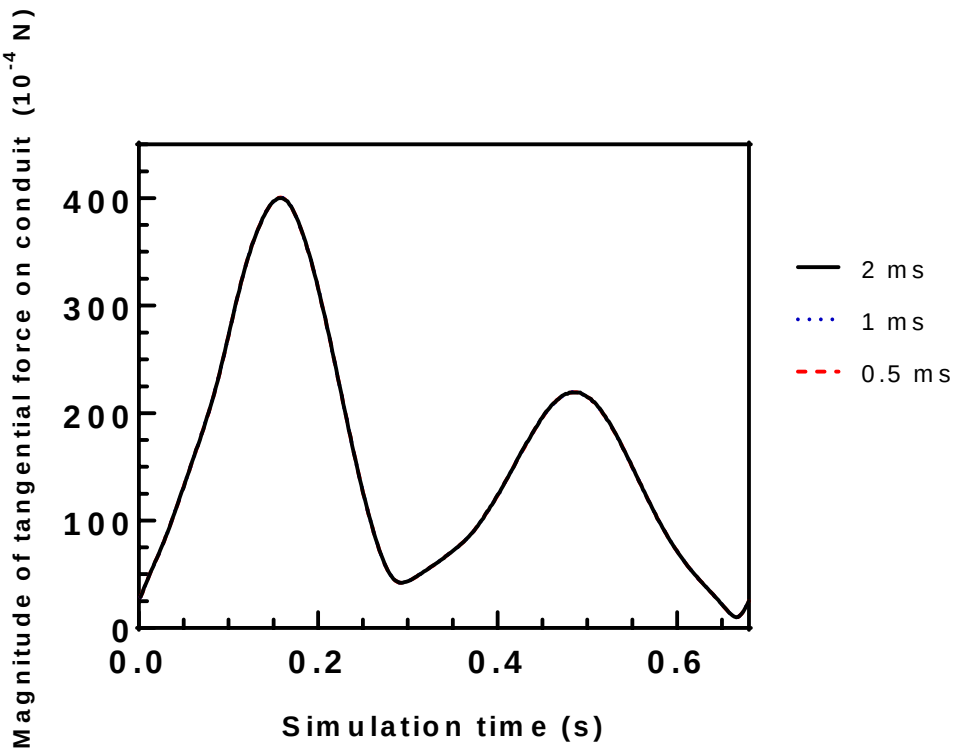

Figure 3.14 Magnitude of tangential force on the conduit over a cardiac cycle resulting from different time-step sizes.

3.7 Methods to compare the efficacy of different geometries

3.7.1 Wall shear and pressure loss

As the aim is to compare the performance of an initial clinically-used conduit with a proposed modified implant, the WSS and total pressure loss over the conduit were determined. The importance of minimising WSS was elaborated upon in Section 2.7. Total pressure loss is indictive of energy loss when the mass flow rate does not change. In this study, it was assumed that the mass flow rate does not change before and after the surgery. This is a reasonable assumption, since the mass flow rate depends on the volumetric capacity of the right ventricle, which is determined by physiological characteristics of the patients and is unlikely to change. The mass flow rate profile before surgery is obtained by multiplying the velocity profile obtained from the echocardiograms of the patients, by the cross-sectional area at which the velocity was measured, by density (Equation 3.7).

Equation 3.7: $\dot{m} = \rho . \dot{V} = \rho . v . A$

where $\dot{m}$ is the mass flow rate, $\dot{V}$ is the volume flow rate, v is the flow velocity of the mass elements, and A is the cross-sectional area. The velocity at the inlet for the initial and modified geometries is then set accordingly to yield the calculated mass flow. In cases where the exact location of the velocity measurement is not specified, it is sensible to define an indicative cross-sectional area by averaging several cross-sectional areas over the conduit.

With these considerations, area-averaged WSS on conduit wall and total pressure loss throughout the conduit over a cardiac cycle for initial and modified geometries were monitored and compared. It was necessary to introduce a metric to measure the scale of the changes of WSS. The effective wall shear on the conduit wall in one second per unit area was calculated using the equation below:

Equation 3.8: Effective $WSS = \frac{\int_{\tau} WSS_{Ave}\, dt}{\tau}$

where WSS_{Ave} is the area-averaged WSS and τ is the period of the cardiac cycle. This equation gives the time and area averaged WSS over a cardiac cycle.

3.7.2 Energy dissipation

In clinical settings, non-computational fluid dynamics options merely allow evaluation of ventricular volumes, flow, and pressure. Even these data are only available on specifically chosen planes, as opposed to the whole volume and their acquisition might require invasive procedures. CFD allows energy-based metrics for assessment of ventricular haemodynamic performance. Energy-based metrics such as energy loss and ventricular stroke work (SW) and efficiency, can integrate several haemodynamic indicators, for instance pulmonary flow and pressure data into a single parameter.

Fewer studies have focused on utilising computational models for performance evaluation of the right heart as it was considered less critical for patients' health. However, extra RV work as a result of conduit dysfunction (stenosis and/or regurgitation) may in turn lead to RV hypertrophy and/or dilation and progressive RV dysfunction [101, 102]. Hence, providing a metric for assessing the energy efficiency of the proposed conduit is necessary. Mechanical energy dissipation rate was selected as an energy-based metric for comparison of initial and modified geometries' performance. The derivation of the expression for mechanical energy dissipation is detailed in Appendix B. Since patients have different periods of cardiac cycle, for comparison, the rate of energy dissipation per second was then obtained by dividing the total energy dissipation over a cardiac cycle by the period.

Simulations were performed using the methods described in this chapter and the results are presented in the next chapter.

4 Results and discussion

4.1 Geometry modification results

Using the methodology described in Section 3.3, the current clinically-used conduit geometry was extracted, and a modified geometry was proposed for each of the six patients. The results are shown in Figure 4.1A-4.1F.

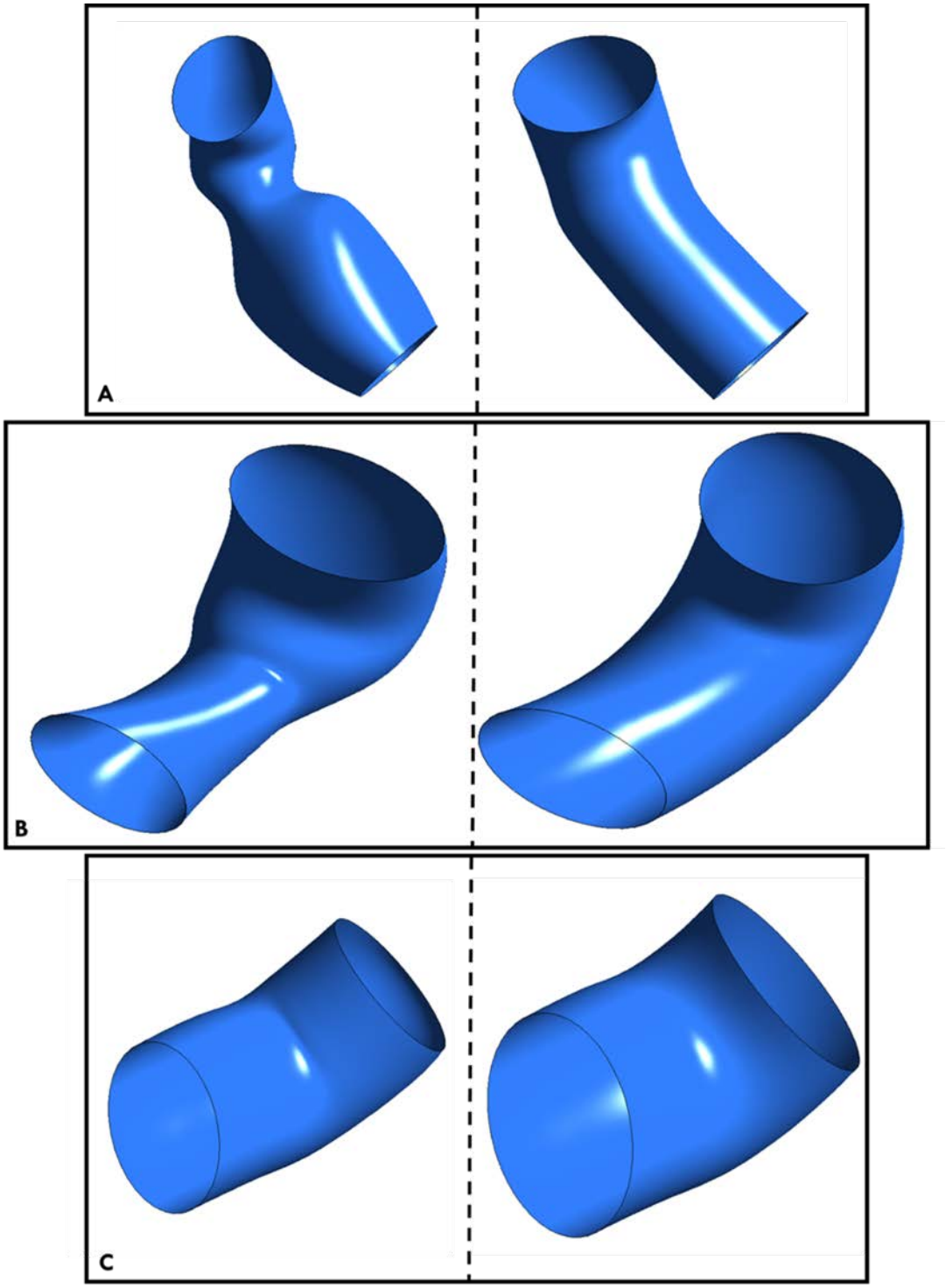

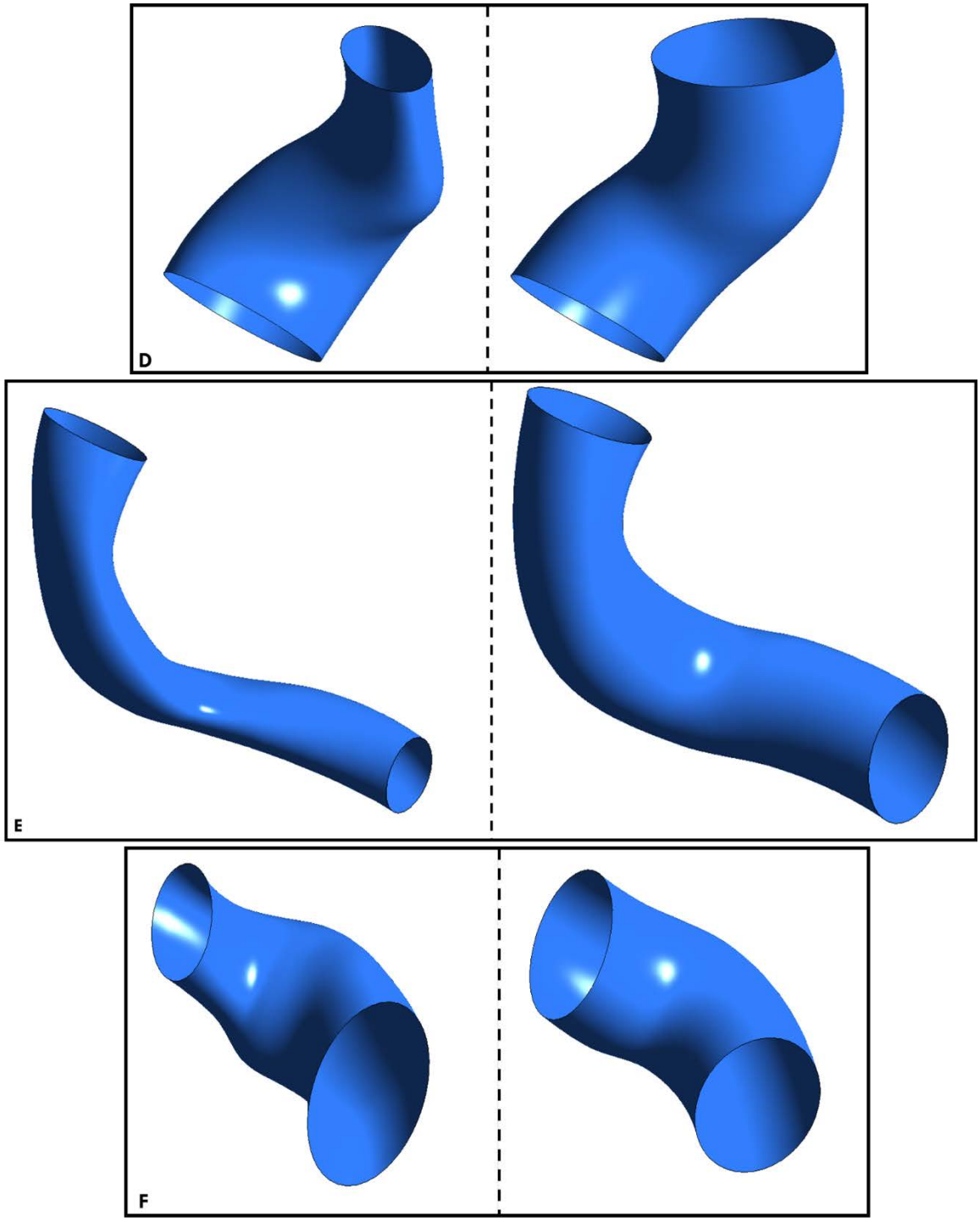

Figure 4.1 Clinically used conduits (left) and proposed modified geometries (right) for patients A-F.

4.2 Flow results

Typical flow (at the beginning of a cardiac cycle) through the initial and modified conduit geometries is shown in Figure 4.2. It is evident from the figure that the flow through the modified geometries is improved as it is more streamlined and has lower velocities. Enlarging

the diameter of the conduit has resulted in lower velocities. Smoothing the sharp curves has reduced or eliminated the circulating flow. This can be seen clearly in patients A and D.

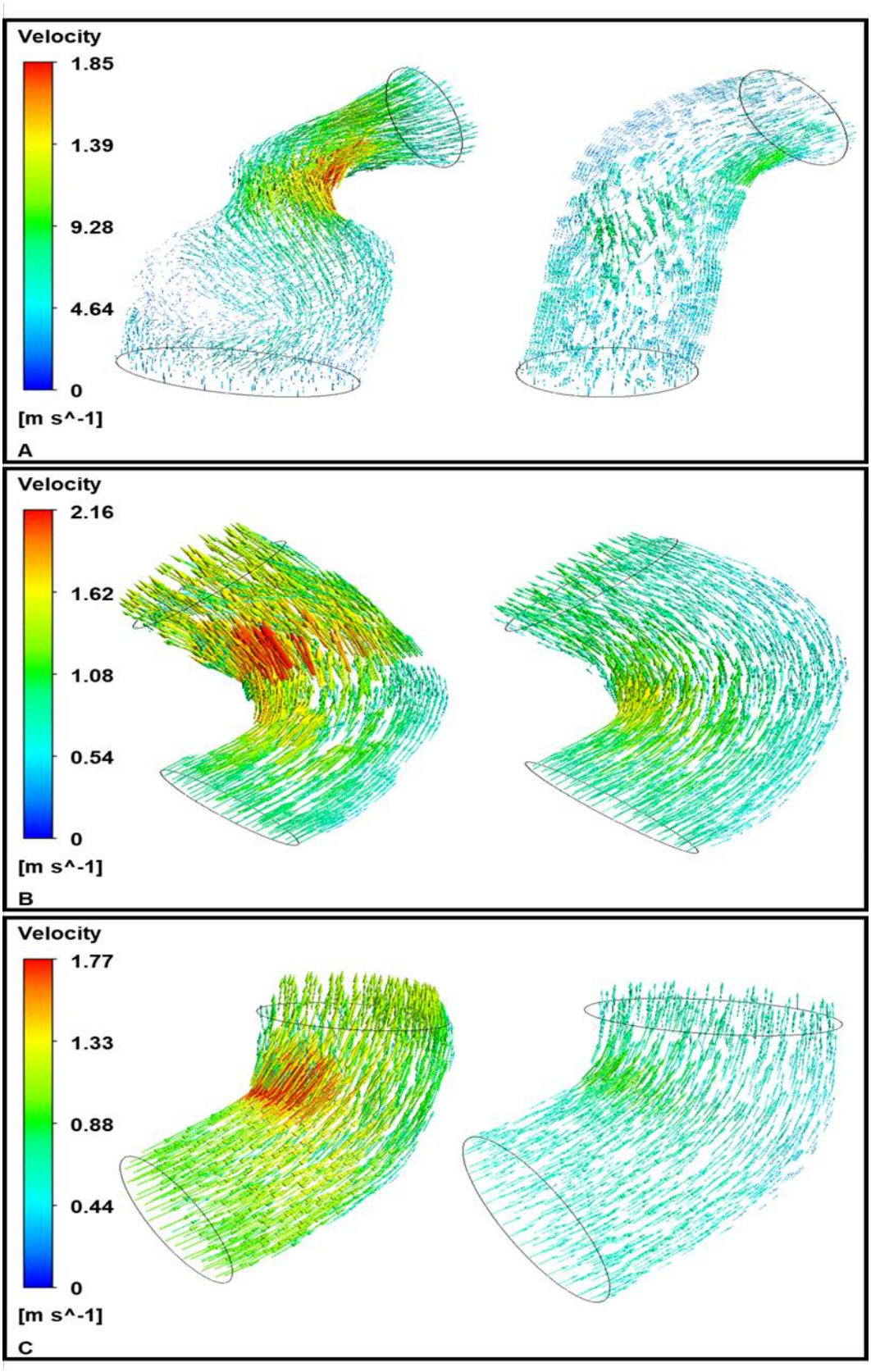

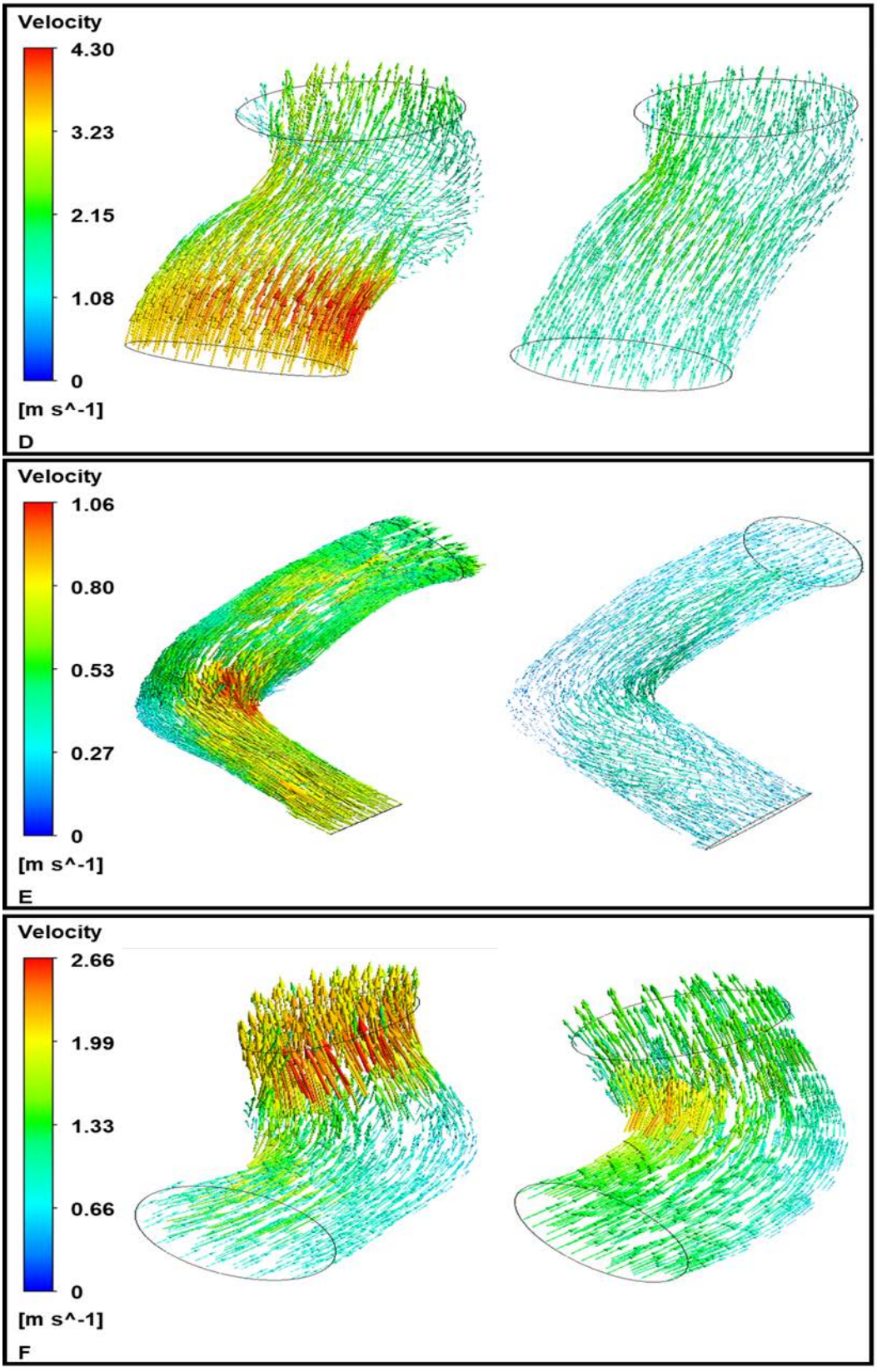

Figure 4.2 Flow through clinically-used conduits (left) and proposed modified geometries (right) for patients A-F.

4.3 Qualitative simulation results

The aim of this section is to compare the performance of the current RV-PA conduits in patient's body with a proposed modified conduit to be used for its replacement. The hypothesis was that upsizing the conduit and smoothing the sharp curves and angles would improve the performance indices, such as total pressure loss and WSS.

The results shown in Figures 4.3-4.8 suggest qualitatively that the implant modification assisted in decreasing the WSS and total pressure loss for all six patients. In all cases, the simulations were performed for 3 cycles to allow stable results, and the results are shown for the first cycle that shows no noticeable change from the previous one.

The changes in total pressure loss are more noticeable than WSS. The reason for this is that upsizing the conduit reduces the velocity substantially, and this has a direct effect on pressure loss. However, multiple factors affect WSS.

WSS changes proportionate to the amount of tangential forces caused by the flow affecting the wall regardless of their direction, hence in the Figures, two peaks are noticed for WSS at points which maximum inward and outward flow happens.

For patient F, it was noticed that different results were produced from those of other patients (Figure 4.8). The first proposed modification of the geometry with the diameter of 17 mm, increased the total pressure loss and area-averaged WSS in contradiction with expectations. Hence, a second modification of the geometry was proposed using the same curves and angles but with an enlarged diameter of 19 mm. This time, similar results to other patients were observed in accordance with expectations.

This case accentuates the crucial influence of the diameter of the conduit on important haemodynamic factors. In addition, it underscores the importance of patient-specific modelling in design of the modified implant. Here, the hypothesised appropriate diameter did not enhance

the performance of the implant, hence, a second geometry was proposed to resolve this issue. This was impossible to foresee without the employment of a patient-specific model. Lastly, 3D model of the heart ensures that patient's anatomy is capable of accommodating the proposed conduit geometry.

It is evident from the following figures that smoothening and upsizing the conduit geometries decreased the total pressure loss and WSS, hence improved their performance.

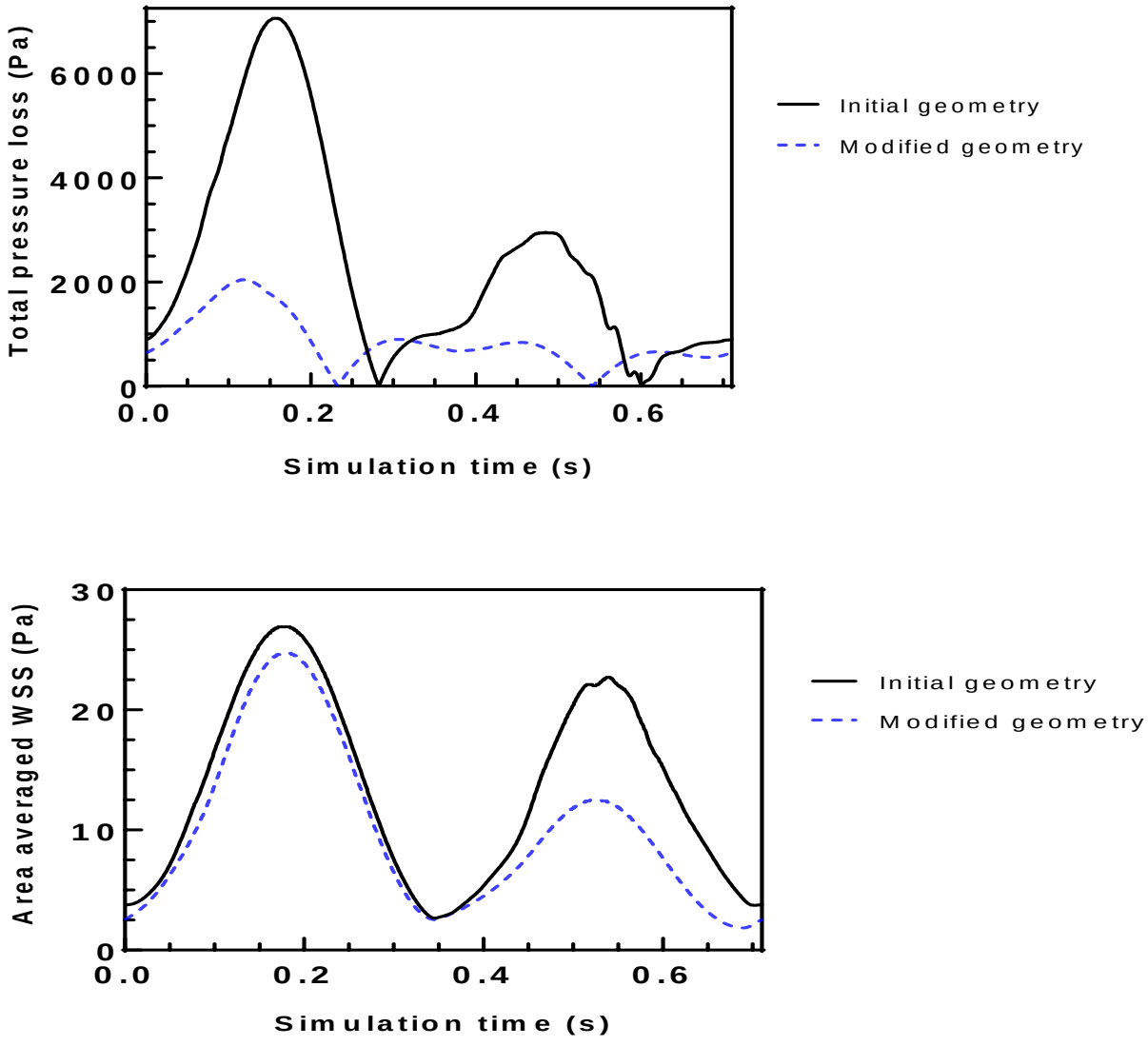

Figure 4.3 Comparison of haemodynamic parameters through the initial implant and proposed modified geometry for patient A. Total pressure loss over the conduit (top) and area-averaged WSS on the conduit (bottom) are shown for a cardiac cycle.

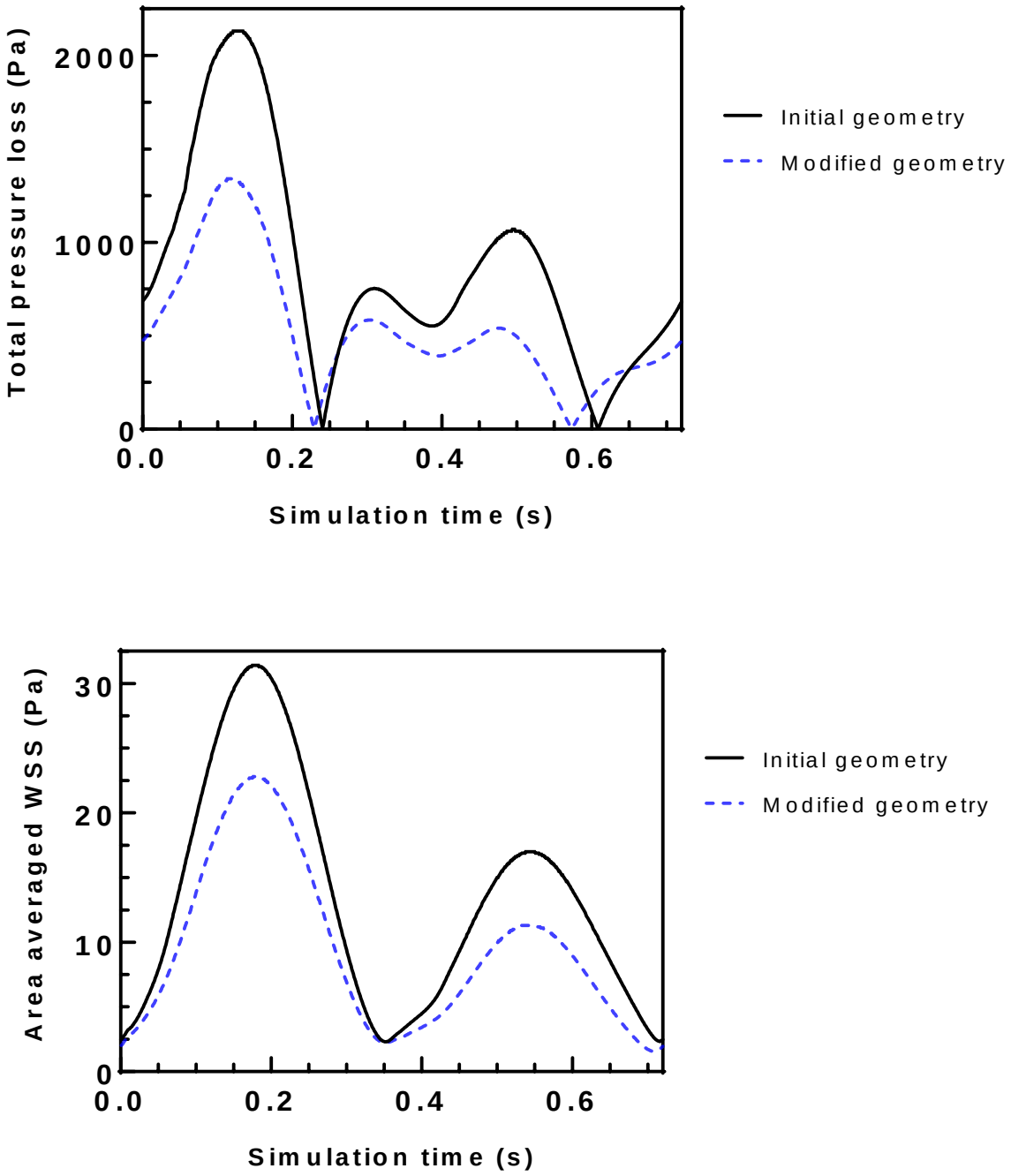

Figure 4.4 Comparison of haemodynamic parameters through the initial implant and proposed modified geometry for patient B. Total pressure loss over the conduit (top) and area-averaged WSS on the conduit (bottom) are shown for a cardiac cycle.

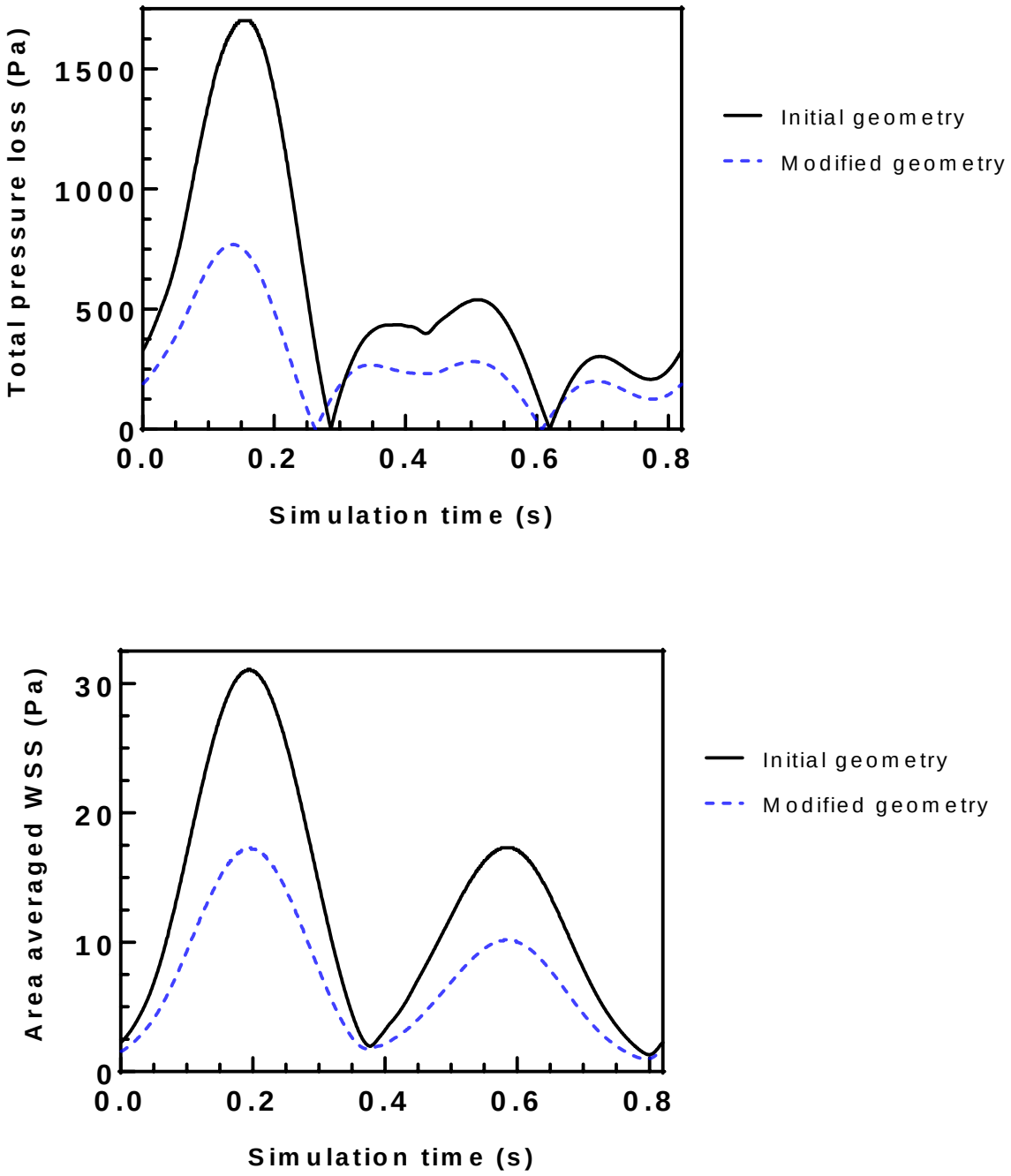

Figure 4.5 Comparison of haemodynamic parameters through the initial implant and proposed modified geometry for patient C. Total pressure loss over the conduit (top) and area-averaged WSS on the conduit (bottom) are shown for a cardiac cycle.

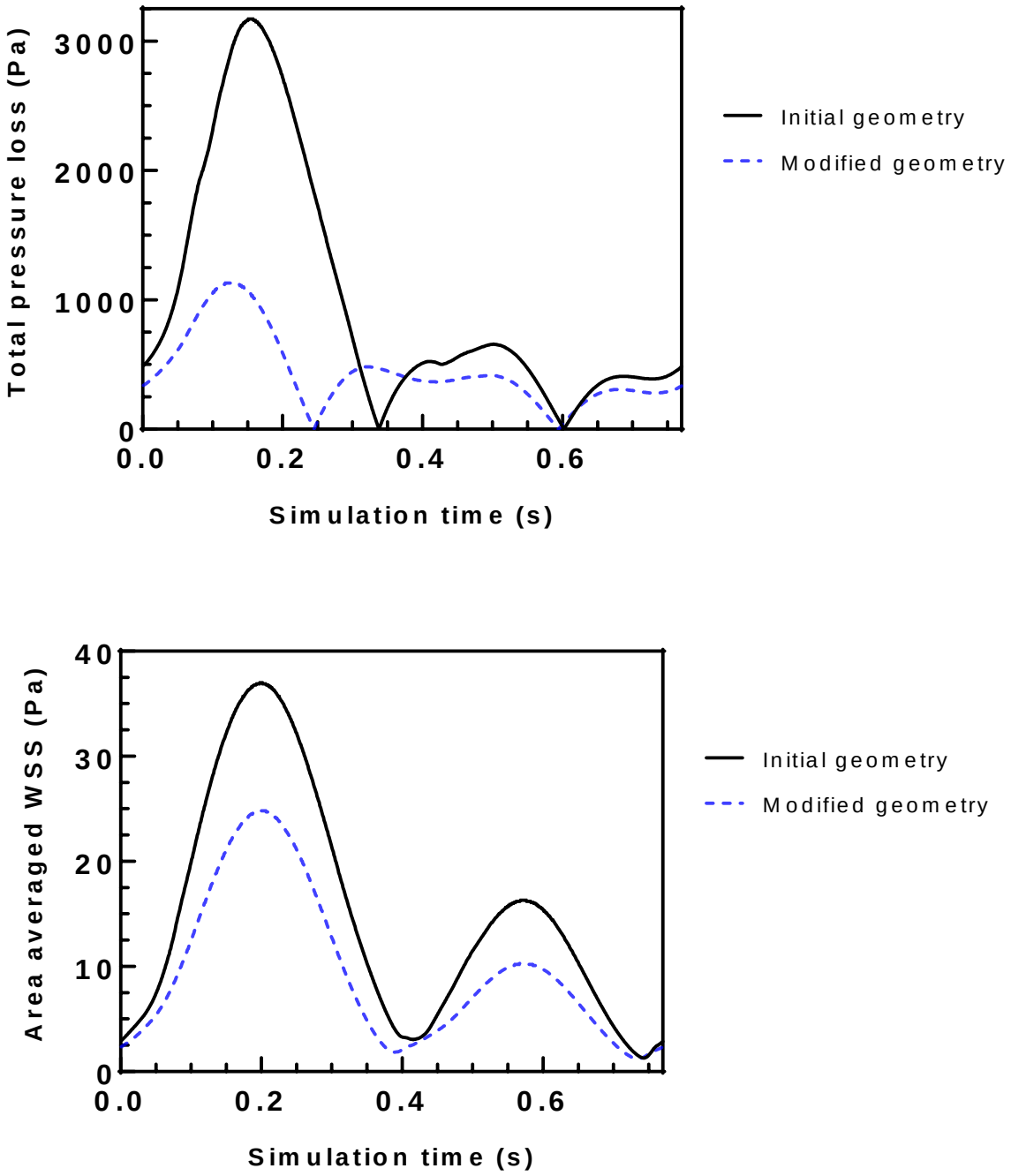

Figure 4.6 Comparison of haemodynamic parameters through the initial implant and proposed modified geometry for patient D. Total pressure loss over the conduit (top) and area-averaged WSS on the conduit (bottom) are shown for a cardiac cycle.

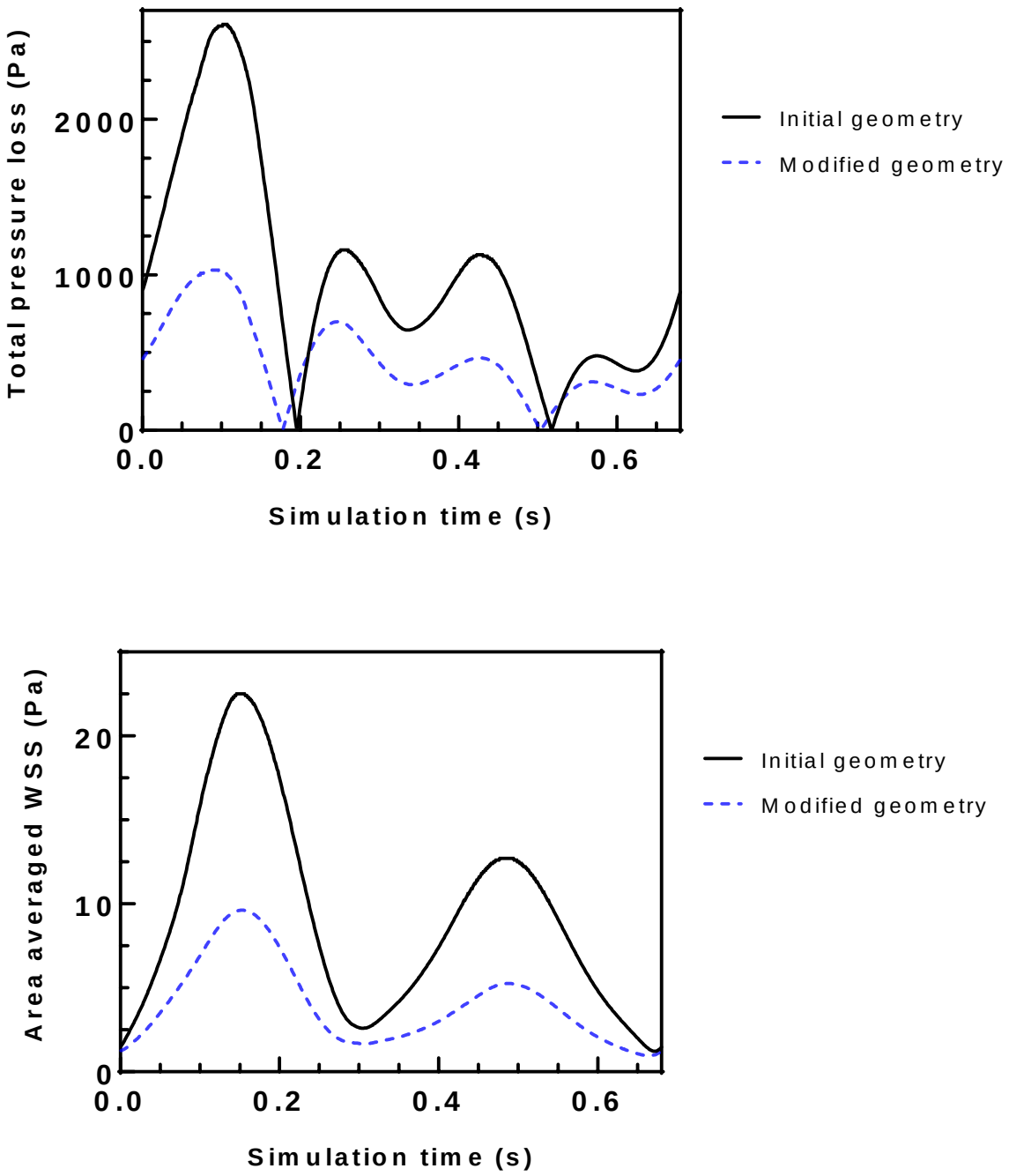

Figure 4.7 Comparison of haemodynamic parameters through the initial implant and proposed modified geometry for patient E. Total pressure loss over the conduit (top) and area-averaged WSS on the conduit (bottom) are shown for a cardiac cycle.

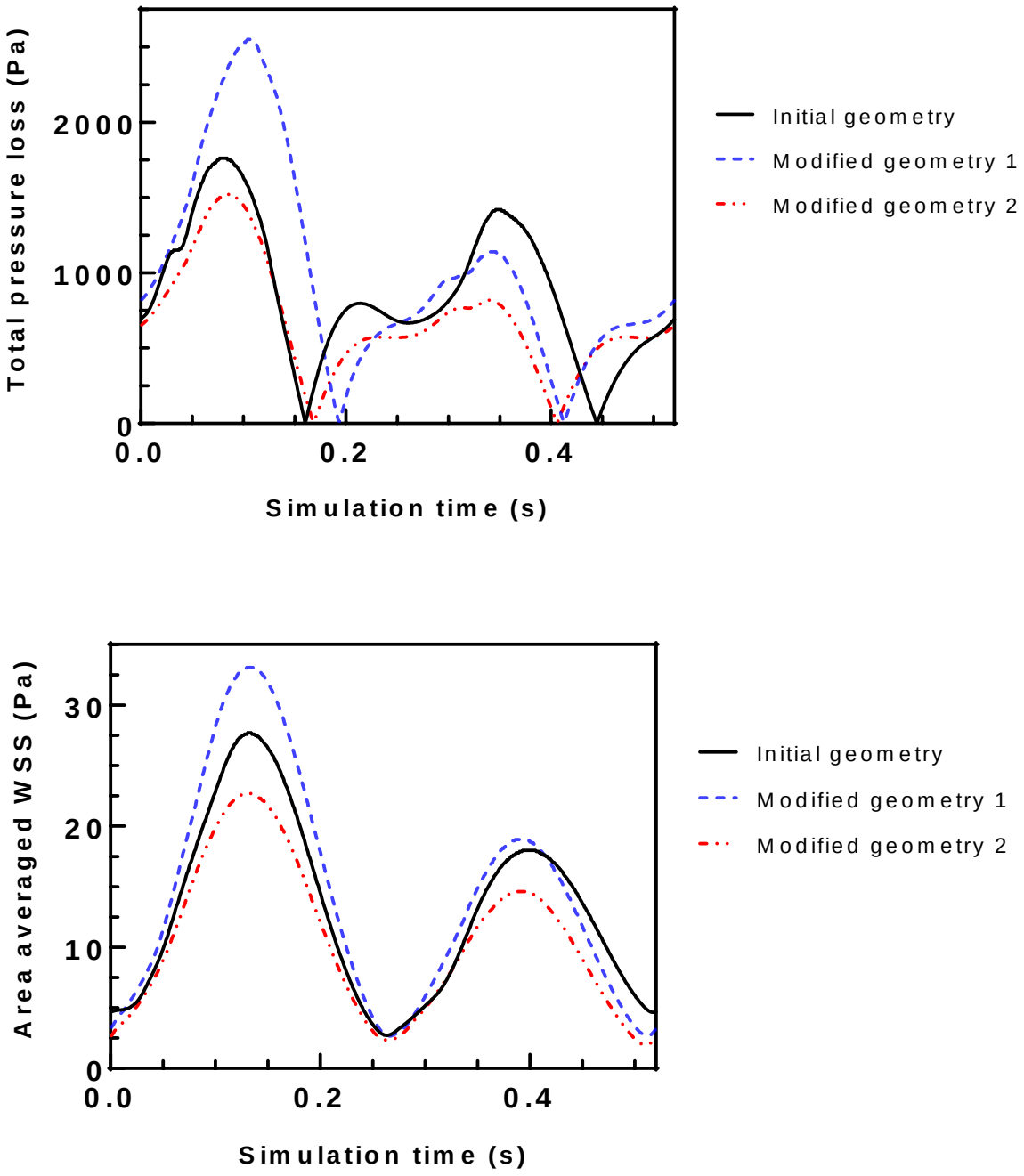

Figure 4.8 Comparison of haemodynamic parameters through the initial implant and proposed modified geometry for patient F. Total pressure loss over the conduit (top) and area-averaged WSS on the conduit (bottom) are shown for a cardiac cycle**.**

Figure 4.9 (A-F) illustrates typical distributions of WSS at the beginning of a cardiac cycle for the initial and modified conduit geometries for all patients. The decrease in WSS in modified geometries is also apparent here.

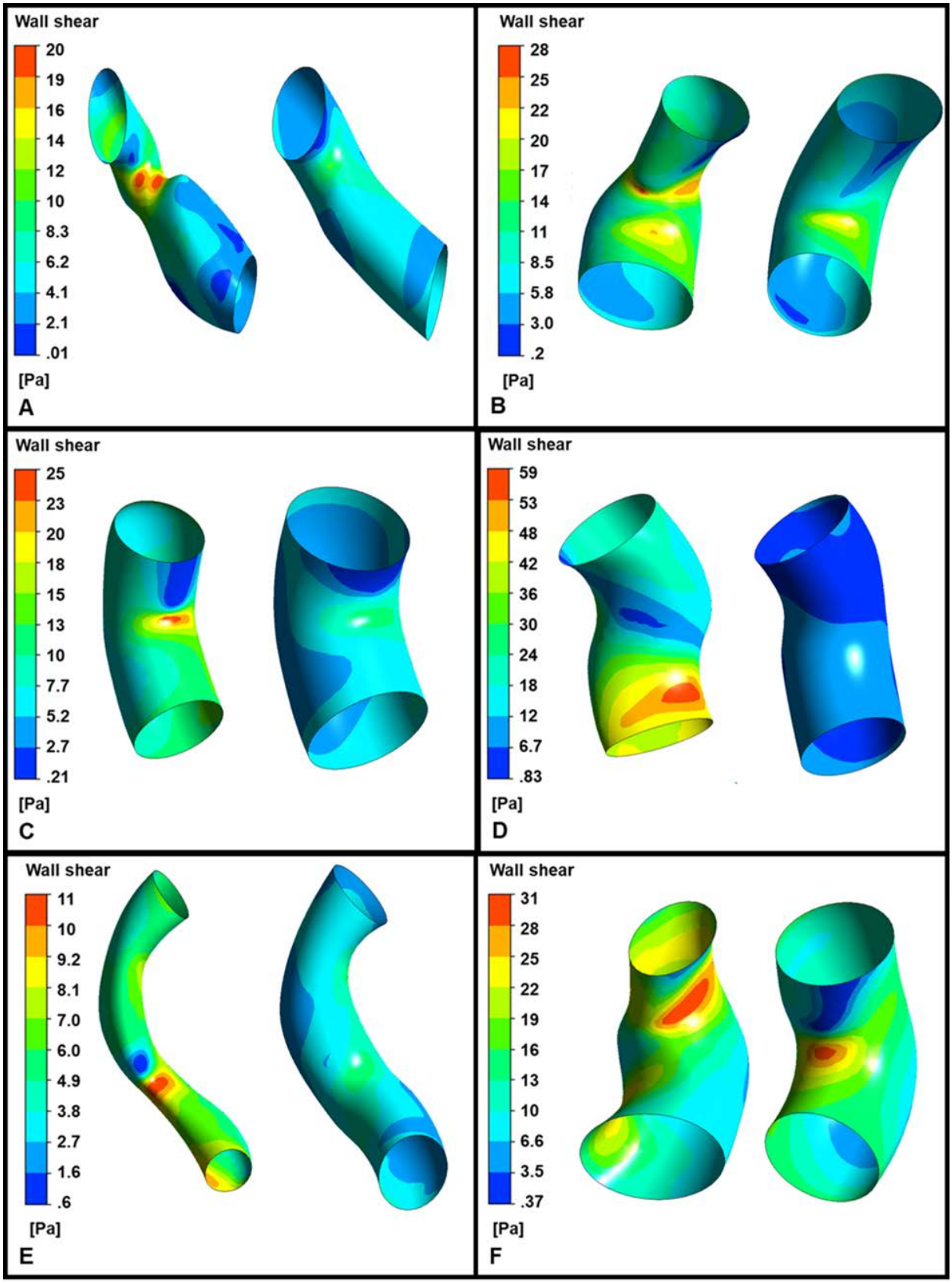

Figure 4.9 Comparison of WSS distribution between initial (left) and modified geometries (right) for patients A-F.

4.4 Quantitative analysis

The values of Effective WSS and energy dissipation as described in section 3.7 were calculated for the initial and modified geometries for each patient. Results are summarised in Table 4.1. Table 4.2 gives the improvement of these parameters for the modified geometries compared with the initial geometries as a percentage.

Table 4.1 Comparison of Effective WSS and energy dissipation for initial and modified geometries for all six patients.

Patient	Effective WSS on initial geometry (Pa)	Effective WSS on modified geometry (Pa)	Rate of energy dissipation in initial geometry (W)	Rate of Energy dissipation of modified geometry (W)
A	13.39	9.97	5.13	0.650
B	13.46	9.41	1.92	1.07
C	12.8	7.26	1.99	0.423
D	14.93	9.54	1.65	0.977
E	9.2	4.03	0.247	0.078
F	13.02	10.58	1.54	1.17

Table 4.2 Improvement in Effective WSS and energy dissipation for modified geometries compared with initial geometries in percentage for all six patients.

Patient	Decrease in Effective WSS (%)	Decrease in energy dissipation (%)
A	25	87
B	30	44
C	43	78
D	36	40
E	56	68
F	18	24

From Table 4.2 it can be seen that the geometry modification process resulted in up to 56% decrease in the effective wall shear and decreased the mechanical energy dissipation through the conduit by up to 87%. These results suggest that if the proposed design of the implant is to be 3D printed and utilised in the surgery to replace the current implant, it is likely to improve the procedure outcome from a fluid dynamics perspective. The most conspicuous benefits of the proposed method would be reduced structural deterioration as a result of reduced WSS which may enhance durability of the conduit. Improvements in energy loss may also translate to improvements in right ventricular performance over time although that has not been tested in our model or by others. 3D printing the proposed conduit will ensure that the anatomy of the patient can accommodate the design, hence eliminating the need for modifications, such as using an additional hood, through the surgery.

In addition, in Appendix C, the performance of the modified geometries is benchmarked against three variations of straight pipes.

5 Computational modelling in material assessment

5.1 Chapter overview

Current off-the-shelf solutions for RV-PA conduit material involve the use of human or animal tissue which fail rapidly and do not grow with the young patient [103, 104]. Therefore, there is an urgent need to develop an alternative implant for vascular conduit that mimic innate tissue. Supramolecular elastomers are appealing materials for fabrication of tissue engineered vascular grafts as such implants mimic the mechanical properties of human arteries. However, elastomeric biodegradable scaffolds have yet to gain wide clinical use.

Computational modelling has a role to play in development of more efficient RV-PA conduits. It can expedite the design optimisation process in tissue engineering by predicting structural mechanics and eliminating the need for mechanical testing at the trial-and-error stages. In this section, this functionality of computational modelling is employed to determine the performance of a biodegradable elastomer developed by our research group. The development, synthesis and mechanical testing of the material was performed by other team members [105], and the contribution of this author is the computational modelling and simulations that are further described in this chapter.

5.2 Introduction

Tissue engineering is an emerging field that may address the ever-increasing demand for *in vitro* engineered tissue [106, 107]. Biodegradable polymers provide the convenience of prosthetics with the functionality of homograft, producing a broadly available therapy for paediatric patients [108]. Bioresorbable polymeric valved tubes have been deployed in human trials by commercial teams such as Xeltis (ClinicalTrials.gov identifier NCT03022708), TEH-Tube program (https://www.teh-tube.eu) and research groups such as those led by Shinoka [109, 110]. Aliphatic biodegradable polyesters, such as polyglycolic acid and polylactic acid are the dominant composition in the reconstruction of their RV-PA conduit [111, 112]. Clinical

concerns include variable scaffold degradation rate (influencing 'growth' and structural integrity), and development of local inflammation causing stenosis (narrowing of the conduit), possibly because of accumulation of toxic by-products or generation of low pH micro-environments, as shown previously [113, 114].

Poly (propylene carbonate) (PPC) is a copolymer that degrades into benign products of water, and carbon dioxide. It is hypothesised that PPC with biologically neutral degradation products can eradicate the associated risks with conventional biodegradable synthetic polymers [113]. However, the mechanical performance of PPC is not within the acceptable range for vascular applications [115]. Physical blending or chemical modifications of PPC is a convenient method to improve the polymer's limitations. For instance, a copolymer of PPC and poly(caprolactone) (PCL) was developed by Spoljaric *et al*. via an efficient one-pot, two-step method with superior toughness and biodegradation properties [116]. PCL has been successfully used to tune the mechanical properties of poly(lactic acid) (PLA) and to establish biodegradation in various polyurethane (PU) systems [117-120]. For vascular tissue engineering, a biodegradable PU with tuneable mechanical properties is favourable with an appropriate functional end group, such as NCO terminated PU without using any toxic catalyst [121, 122]. Therefore, it was speculated that a tri-block copolymer consisting of PPC, PCL and PU could be a promising biomaterial for fabricating biodegradable implants that mimic the natural structure of pulmonary artery.

Hence, PPC-PCL-PU was synthesised by our team members and its suitability for RV-PA implant construction was investigated by characterising its mechanical and biological performances. A one-pot catalyst-free chemical reaction comprising polycondensation followed by esterification was used for synthesis of this triblock copolymer with the NCO-terminated groups. *In vitro* assays using human endothelial cells confirmed survival, proliferation, and exertion of angiogenesis properties. A subcutaneous implantation mice

model demonstrated the biocompatibility of the synthetic elastomer. These findings support the utility of this triblock copolymer for tissue engineering pulmonary arteries. Herein, the application of computational modelling for *in situ* evaluation of the synthesised material performed by the author is described.

The conduit structure was modelled to compare the performance of the synthetic material with that of the original material in similar conditions using computer simulations, which also allowed the determination of appropriate dimensions of the synthetic material to mimic the behaviour of a homograft pulmonary wall. The material with the optimised dimensions obtained from simulations was then synthesised [105]. The results of mechanical testing on this material showed similar properties to that predicted from simulations. Computer simulations had the advantage of being less time and cost consuming than laboratory and animal experiments.

5.3 Application of computational modelling in tuning mechanical properties of the synthesised material to achieve optimal results

5.3.1 Initial mechanical tests

In re-creation of the pulmonary artery, it is critical to design a material with similar mechanical and surface properties. A stiffer and less elastic structure can cause deterioration, calcification, and stenosis when used in cardiovascular applications [123, 124]. The design of the triblock copolymer was initially guided by the measurement and analysis of a human pulmonary artery wall (Figure 5.1A to 5.1D).

The human pulmonary artery wall and the invented material were tested mechanically using an Instron (model 5543) with a 1000 N load cell [117]. The elongation (mm) and load (N) were obtained at a crosshead speed of 30 μm/s and up to 0.5 mm/mm of strain level. The ultimate tensile strength, tensile modulus, and elongation at break were then calculated using

stress−strain curves and the linear strain region of 0.1 to 0.2 mm/mm. The mechanical properties of both pulmonary artery wall and synthetic materials are given in Table 5.1.

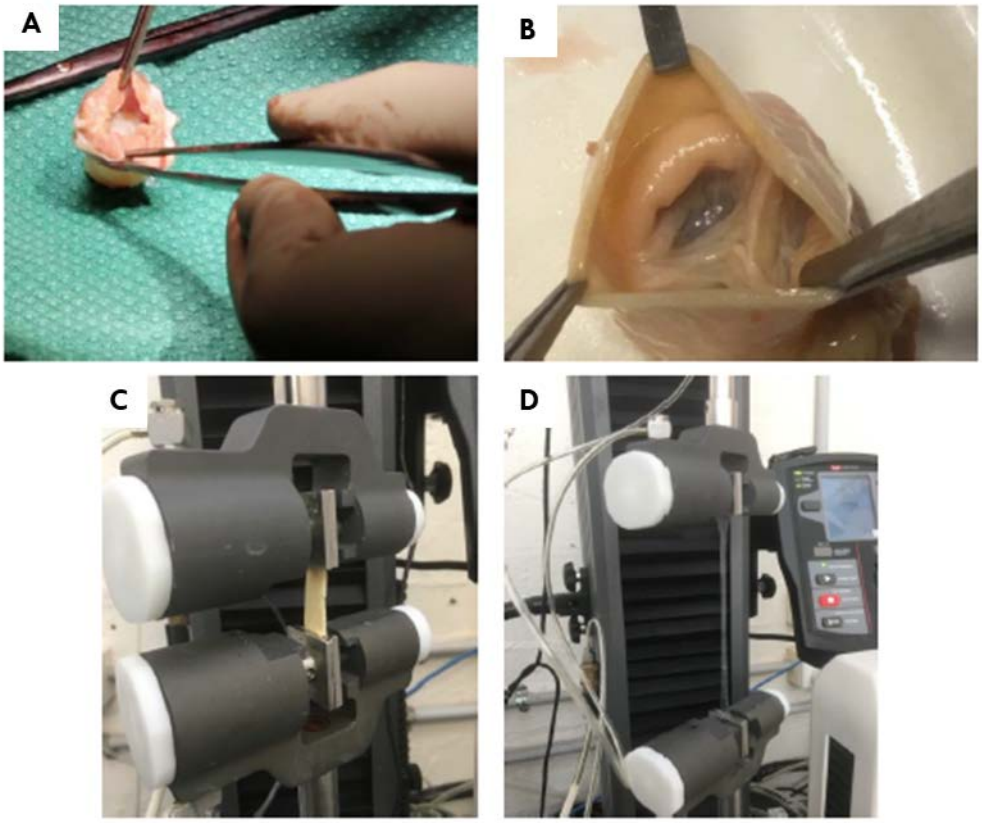

Figure 5.1 Mechanical properties. (A) and (B) a pulmonary artery sourced from human cadaverous tissue; (C) tensile testing of the homograft tissue; and (D) tensile testing of the tri-block copolymer.

Table 5.1 A summary of the mechanical performances of the pulmonary artery wall and synthetic polymers at different steps [117].

Sample	Tensile modulus (MPa)	Ultimate tensile strength (MPa)	Elongation at break (%)
Pulmonary artery wall	1.69 ± 0.36	0.71 ± 0.08	73 ± 0.85
PPC	17.12 ± 0.89	6.65 ± 1.01	8.6 ± 1.8
PPC-PL	13.87 ± 0.97	3 ± 0.14	14 ± 0.71
PPC-PL-PU	0.61 ± 0.12	0.69 ± 0.02	880 ± 24.3

The tensile test showed that the ultimate strength and elongation at break of the homograft tissue are 0.71 ± 0.08 MPa and 73 ± 0.85 %, while the sample possessed a tensile modulus of 1.69 ± 0.36 MPa (Table 5.1). These values for PPC as the primary material were 17.12 ± 0.89 MPa, 8.6 ± 1.8 % and 6.65 ± 1.01 MPa, respectively. The chemical modification of PPC using PCL and PU led to the formation of a synthetic structure that mimics the mechanical properties of the human pulmonary artery wall. The tensile modulus and ultimate tensile strength of the biodegradable polymer dropped to 0.61 ± 0.12 and 0.69 ± 0.02 MPa with a significantly higher elongation at break at 880 ± 24.3 %. These values were measured for a polymer sheet 0.1 mm in thickness. All the results are reported as mean ± SD acquired from at least three independent experiments at each condition. Statistical analysis (N = 3) was performed using a one-way analysis of variance (ANOVA) with a Tukey's multiple comparisons tests for a significance level of $p < 0.05$.

5.3.2 Modelling and Simulation

Both physicochemical properties and the thickness of the material have impacts on mechanical strength and function of materials used for the construction of a valvular conduit. Therefore, structural analysis was used to predict the optimised thickness of a conduit made from materials developed to reduce the risk of failure. To this end, the deformation of the innate conduit under the maximum arterial pressure of 16.6 kPa (125 mmHg) was set as a reference (Figure 5.3A) and compared with the deformation of the conduit made from synthesised material with varying thicknesses ranging from 0.1 to 1.4 mm (Figure 5.3B to 5.3E). The objective was to ensure the synthetic material mimics the innate tissue and remains durable in physiological conditions. The lower deformation at the maximum pressure endorse stability of the materials.

Static structural analysis was performed using ANSYS Mechanical V19 to compare the behaviour of innate tissue and synthetic polymer and to predict the optimised thickness of the polymer. To this end, a cylindrical geometry was considered in the modelling with length of

50 mm and inner diameter of 15 mm that was estimated based on the average size of common implants for children (12-18 mm). The geometry was constructed using ANSYS SpaceClaim and meshed with shell elements (Figure 5.2). The mechanical properties of the innate material and the synthesised tissue were then imposed on the model. The Young's modulus was measured using an Instron, while the densities were measure using conventional Archimedes method [105]. The Poisson's ratio value (0.5) was adopted from [125]. The maximum arterial pressure in the region of interest, which is 125 mmHg (16.6 kPa), was applied uniformly on the inner surface of the conduit. Therefore, the maximum deformation on the wall of conduit can be measured to reduce the risk of failure. Fixed supports were applied at both ends, which results in maximum deformations and satisfies the objectives of replicating the original material behaviour. Furthermore, the wall material was assumed to have linear characteristics in both cases. In this study, the length and diameter for cryopreserved human pulmonary artery and synthetic material were constant at 50 and 15 mm, respectively. The wall thickness for the pulmonary artery was kept constant at 0.5 mm, while this value for synthetic material was variable.

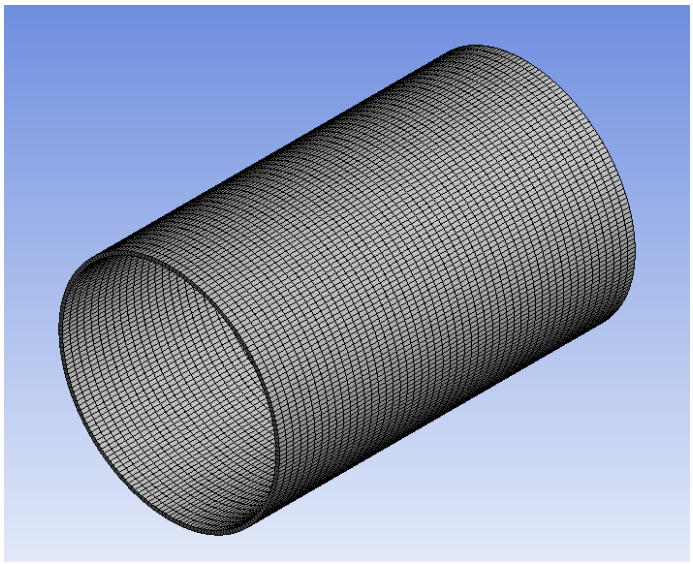

Figure 5.2 Shell element mesh for the simplified conduit geometry.

The maximum arterial pressure in physiological condition for the region of interest is 16.6 kPa. As shown in Figure 5.3A, the maximum deformation of the native conduit material for an

internal pressure of 16.6 kPa was 1.1 mm. The simulation of the synthetic material with a thickness of 0.1 mm under this pressure led to high deformations that prevented model convergence (data not shown). It means that under these boundary conditions, the synthetic material does not replicate the functionality of innate conduit tissue. For the synthetic material it was desirable to avoid conditions that deformation was 5-fold greater than 1.1 mm (e.g. 5.5 mm deformation). The thickness of the synthetic material and the applied internal pressure of the conduit were then manipulated to satisfy this condition. In the following numerical experiments, it was assumed that the Young's modulus was independent of the thickness.

Simulations were conducted on the synthetic material with the initial thickness at lower pressures. The maximum pressure that resulted in less than 5.5 mm was 2.2 kPa (Figure 5.3B). This was only 13% of the maximum pressure and demonstrated that the deformations for the synthetic polymer were higher compared with the innate tissue under the maximum pressure. Hence, material performance had to be improved in terms of durability. It was hypothesised that increasing the thickness of the synthetic material might decrease the deformation. To this end, in the simulation the maximum pressure (16.6 kPa) was applied while the thickness of the polymer was gradually increased until similar behaviour to that of the innate tissue was achieved at a thickness of 1.3 mm (Figure 5.3C). The thickness of the synthetic material was then increased further to 1.4 mm, and this produced a 10% reduction in deformation (Figure 5.3D). Results of a simulation of the synthetic material with 0.5 mm thickness, the same thickness as the native conduit material, is displayed in Figure 5.3E. The maximum pressure that resulted in the desirable deformation as described before was 9 kPa, which is nearly half of the maximum pressure in the conduit. It was observed that the total deformation was still higher than the innate tissue for the maximum pressure of 16.6 kPa (Figure 5.3A). Therefore, increasing the thickness of the synthetic material to 1.4 mm was deemed likely to replicate the native tissue's behaviour.

The mechanical properties of the PCL-PPC-PU materials after increasing the thickness to 1.4 mm showed similar behaviour in tensile modulus to the native pulmonary artery. The tensile modulus was elevated to 1.43 ± 0.78 MPa, while the ultimate strength and elongation at break remained constant. Therefore, the deformation behaviour of the PCL-PPC-PU under the maximum physiological conditions followed the same pattern as the normal pulmonary artery.

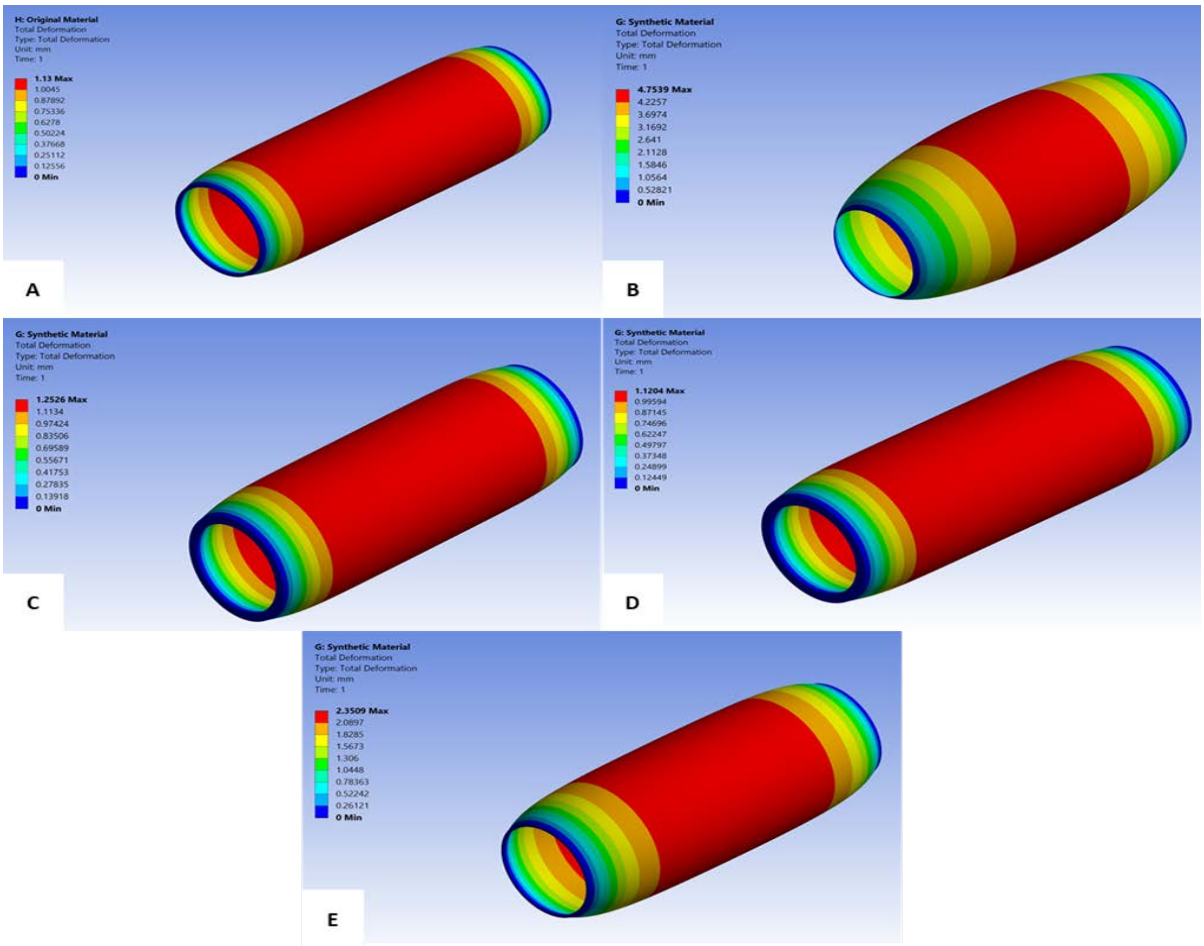

Figure 5.3 Structural analysis to compare the behavior of native tissue with the synthetic material with various thicknesses. (A) deformation of the original conduit for an internal pressure of 16.6 kPa; (B) deformation of the synthetic material with initial thickness of 0.1 mm for an internal pressure of 2.2 kPa; (C) deformation of the synthetic material with thickness of 1.3 mm for an internal pressure of 16.6 kPa; the minimum thickness of the synthetic material required to behave similar to the original tissue under the maximum pressure; (D) deformation of the synthetic material with thickness of 1.4 mm for an internal pressure of 16.6 kPa; increasing the thickness to 1.4 mm leads to even more conservative option; (E) deformation of the synthetic material with thickness of 0.5 mm for an internal pressure of 9 kPa.

5.4 Structural analysis of initial and modified geometries

In this section, the structural analysis was extended to the initial and modified geometries of each patient to compare their deformations and equivalent stresses. Here, instead of applying the maximum arterial pressure with a uniform distribution, the pressures resulting from CFD simulations are imported as loads, which creates a more realistic load condition. Fixed supports are applied at both ends of the conduit. An automatic thin sweep mesh method with solid shell elements is employed. The meshing for current clinically-used conduit for patient E is shown in Figure 5.4. To demonstrate the influence of the geometry modification, it is assumed that the same material as the current clinically-used conduit will be used for the proposed modified conduit. The mechanical properties of this material are selected to replicate the pulmonary human artery wall (Table 5.1). Total deformation and equivalent (von-Mises) stress at the beginning of a cardiac cycle, which shows a typical time, are calculated and shown in Figure 5.5 and 5.6. A significant reduction of these parameters for all modified geometries is evident from these figures. This reconfirms the conclusions made in the previous chapter.

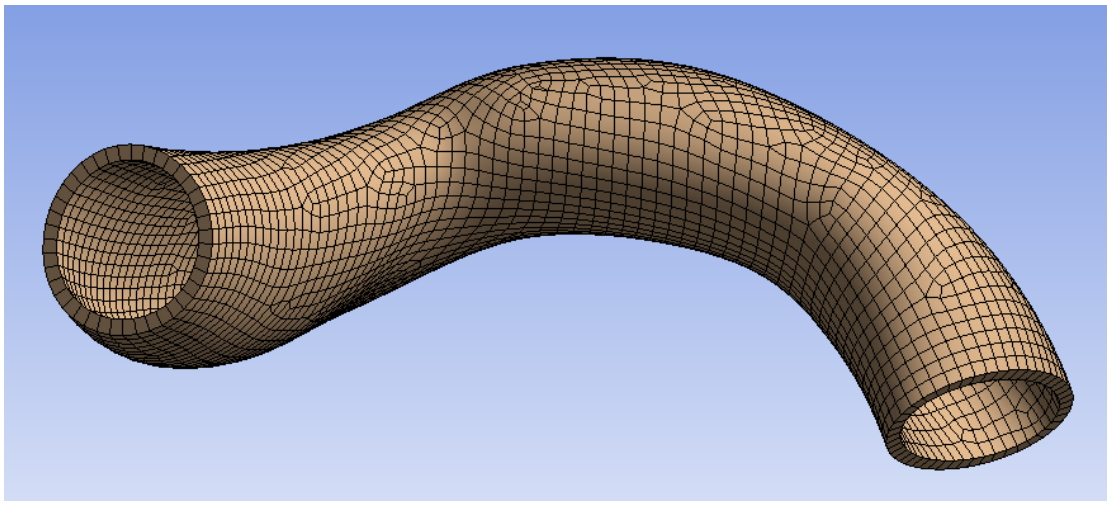

Figure 5.4 Automatic thin sweep mesh method demonstrated on initial conduit of patient E.

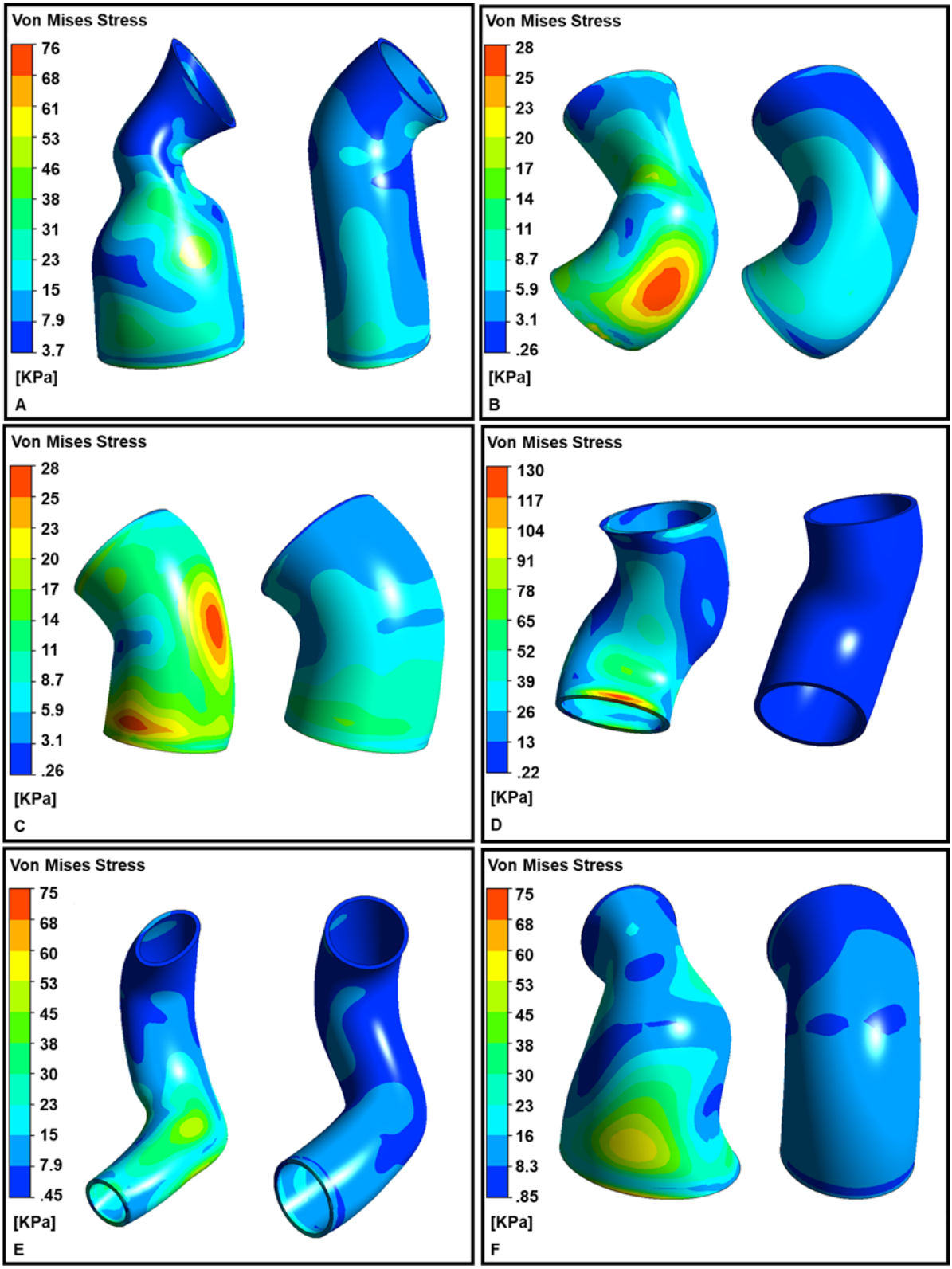

Figure 5.5 Comparison of the equivalent stress on conduit's wall between initial (left) and modified geometries (right) for patients A-F.

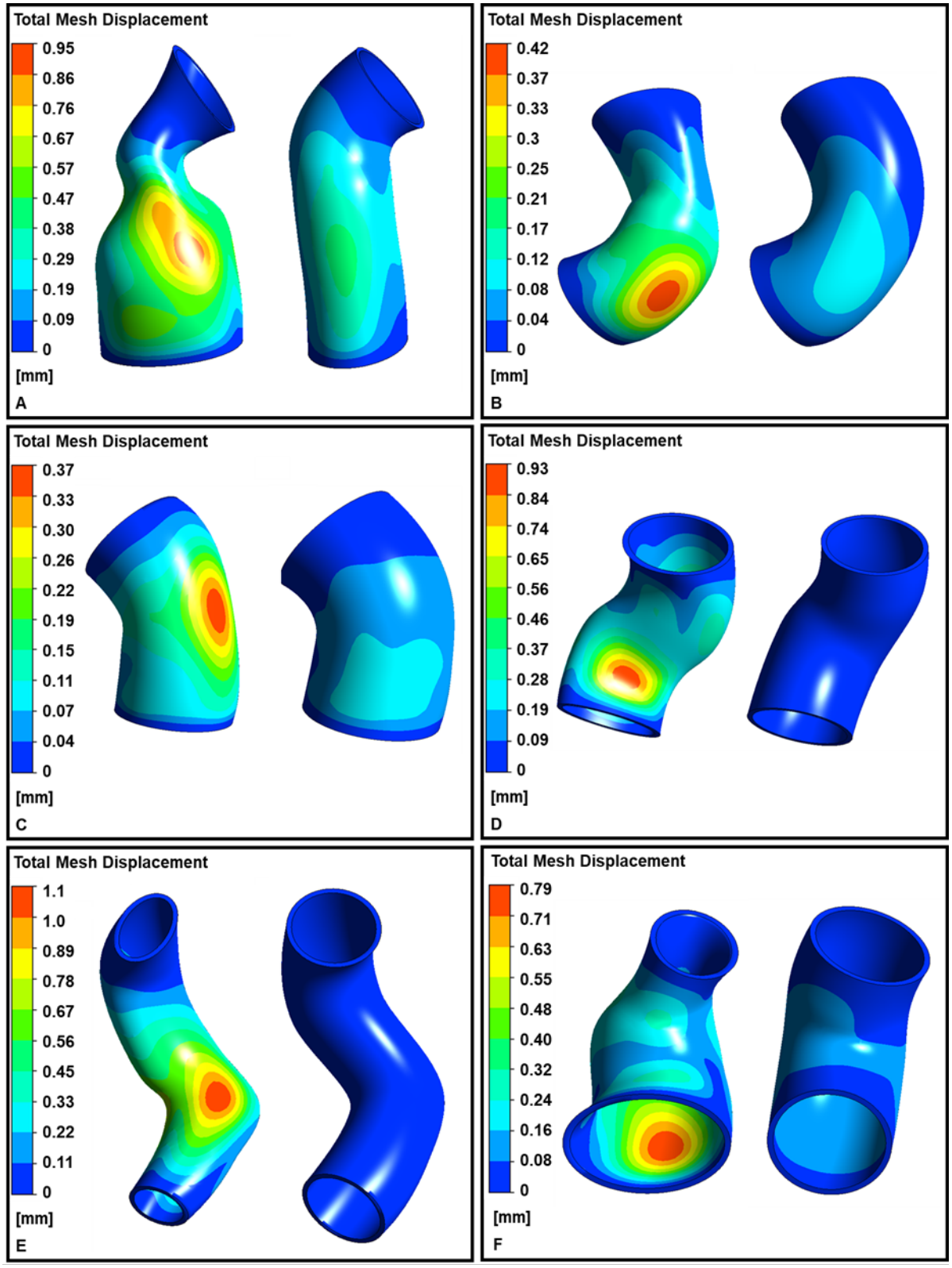

Figure 5.6 Comparison of the conduit's wall deformation between initial (left) and modified geometries (right) for patients A-F.

5.5 Conclusions

Finite Element Analysis (FEA) simulations allowed prediction of the mechanical behaviour and to obtain the optimised thickness of the material without the need to produce it at each step. Simulations minimise the time and lower the cost as the parameters could be altered instantly and the results of each step were produced rapidly, compared with experimental trial and error. One-way fluid structure analysis of the initial and modified geometries showed reduced total deformations and equivalent stresses for modified geometries. Therefore, it reconfirmed that the performance of the implant was improved in all cases.

6 Conclusions and future direction

This work was aimed to develop a methodology for patient-specific optimisation of the geometrical design of the RV-PA implant and to utilise computational modelling to expedite the material design process. Proof of concept is provided that can be extended in the future with ultimate goal of 3D printing customised conduits for each patient to be used during replacement surgery or percutaneous implantation.

Integration of clinical data with engineering techniques allowed construction of patient-specific models that can be used for optimisation of the geometrical design of the implant. Patient-specific models were constructed using the clinical data, and CFD analysis was employed for design modification. Structural analysis was also utilised to evaluate the performance and to optimise the dimensions of a tissue engineered material.

A methodology for extracting implant's geometry from segmented medical images of the heart was successfully developed. A strategy for modifying the geometrical design of the implant considering the anatomy and clinical data of patients was advanced. Models of the initial clinically-used implants and proposed modified implants were constructed and suitable boundary conditions were applied.

Simulation of blood flow through the initial and modified geometries showed significant improvements in flow patterns, total pressure loss, WSS, and mechanical energy dissipation for the modified geometries. It was demonstrated that flow was more streamlined, and the total pressure loss was reduced through the modified geometries. Average WSS on the conduit wall was reduced by between 25-56 % and mechanical energy dissipation rate was reduced by between 24-87 % in the modified geometries for patients A-F. Hence, the goal of designing a patient-specific haemodynamically improved implant was realised.

The patients were selected to be a representative spread of pathologies and conduit types. Hence, it is predicted that the proposed method would result in haemodynamic improvement

for most cases. However, the scale of improvement cannot be directly extrapolated to the wider population of patients with RV-PA connections as yet, due to a large inter-patient variability.

With current approaches, replacement of RV-PA conduits is unavoidable for patients with a reconstructed RVOT. The underlying factors that necessitate the replacement of the conduit include valve incompetence, regurgitation, stenosis, and above all conduit obstruction. It is intuitive that all these attributes contribute to mechanical energy loss. Hence, the methodology developed for evaluation of energy dissipation over the conduit could, in the future, be employed to calculate an index of energy loss, as an aide in the monitoring of patients with a conduit and to guide the timing of replacement.

Currently, the indication of re-operation is based on echocardiography measurements of RV to PA pressure gradient (pressure gradient over the conduit), or the ratio of right ventricular systolic pressure to left ventricular systolic pressure [126]. These are all subjective and sometimes not easily replicated between observers, and echocardiography windows can be poor for some patients. An index of energy loss might be very useful clinically, since it incorporates all the elements that combine to produce conduit failure. If serial MRIs were done, an index of energy low could guide timing of reoperation before the development of right ventricular failure, since symptoms of excessive RV work appear late and are usually non-specific, for instance, tiredness and exercise intolerance.

The models constructed in this study can be improved by including turbulence in blood models in geometries with higher Reynolds numbers (patients A, C, D). Effects of suture lines on the haemodynamics can also be studied. Including pulmonary artery branches in the model can be done as an extension to this study, which is predicted to have a significant effect on the results of energy dissipation and stress distribution. Moreover, the effect of the valve on the flow, energy dissipation, and WSS distribution needs to be investigated.

In addition to the conduit design, computational modelling can play a significant role in valve design – an important aspect of conduit design that has not been covered by this work. Valve competence is an important clinical outcome and clinical experience suggests that homografts – in particular – often develop regurgitation within weeks to months of implantation. Potentially, models can be constructed to compare the behaviour of a proposed design (with a proposed material) with a normal human valve.

Validation of the simulation results against clinical data is necessary. Velocities and pressures at several points in the conduit can be compared with MR or echocardiography measurements to ensure the accuracy of the results. An inherent limitation of this study is the use of pre-operative boundary conditions for evaluating the performance of a proposed modified implant. Hence, prospective paired analyses of conduit performance before and after replacement is needed to validate the conclusions. Correlation of non-invasive assumed values with invasively measured data in a subset of patients and/or animal models can also be investigated.

As an extension to this study, employment of modern geometric modelling techniques such as iso-contouring that are the basis of Iso-Geometric analysis [127] can be investigated for patient-specific modelling of RV-PA conduit. Iso-Geometric analysis can be a valuable tool in modelling deforming geometries such as valves since mesh refinements can be performed automatically in this method. These methods enhance the accuracy of geometric acquisition and may be a first step towards automating the performance assessment and design process of RV-PA valved conduits. This would have the potential to be included in post-operative monitoring and management paradigm of these patients.

In this study, haemodynamical improvement of a proposed modification of a current clinically used conduit was demonstrated. As a test of concept, the ‘ideal’ geometry can be 3D printed for temporary placement intraoperatively, to confirm that design fits and is appropriate, after

removal of the existing conduit and before placement of the new homograft or xenograft. This may assist in modification of the described techniques. For example, currently the modified geometry was lofted along the centreline of the current conduit. This is not the only design that is feasible, the performance of several independent geometrical designs for each patient can also be studied and compared in the future.

In addition to customisation of the geometrical design of the implant, computational modelling was used to compare the behaviour of a synthetic material with innate pulmonary wall tissue under the maximum arterial pressure. Accordingly, structural analysis was used to predict the appropriate thickness of the synthetic material to replicate the stiffness of the innate tissue. The synthesised material with the proposed thickness showed similar mechanical properties to pulmonary wall tissue. This method helped expediting the material design process by eliminating the need for unnecessary *in vivo* assessments. The comparison of the performance of the initial and modified geometries using structural analysis, with pressure distributions from the CFD analysis, showed significant improvements in wall deformation and equivalent stresses in proposed designs.

For evaluation of the deformations and equivalent stresses in Chapter 5, more sophisticated material models that account for anisotropy and non-linearity of the material can be utilised. Deformation of the walls can be taken into account by employing two-way FSI analysis instead of one-way structural analysis performed in this study. However, it should be noted that two-way FSI analysis is more important for simulations of more deformable structures, such as valves. The deformation of the conduit wall is relatively small, hence, FSI analysis is not critical for conduit geometry studies without a valve.

Lastly, addressing the ultimate goal of the research group, more investigation on the material biocompatibility, material physical characteristics relevant to specific age groups, valve design and the possibility of 3D printing for manufacture will be required.

References

[1] https://www.heartkids.org.au/congenital-heart-disease

[2] M. E. Oster, K. A. Lee, M. A. Honein, T. Riehle-Colarusso, M. Shin, and A. Correa, "Temporal trends in survival among infants with critical congenital heart defects," *Pediatrics,* vol. 131, no. 5, pp. e1502-e1508, 2013.

[3] N. A. Kasparian, D. S. Winlaw, and G. F. Sholler, "Congenital heart health: how psychological care can make a difference," *Medical Journal of Australia,* vol. 205, no. 3, pp. 104-107, 2016.

[4] K. Triedman John and W. Newburger Jane, "Trends in congenital heart disease," *Circulation,* vol. 133, no. 25, pp. 2716-2733, 2016.

[5] J. E. Kim, S. H. Kim, and Y. Jung, "Current status of three-dimensional printing inks for soft tissue regeneration," *Tissue Engineering and Regenerative Medicine,* vol. 13, no. 6, pp. 636-646, 2016.

[6] A. Quarteroni, A. Manzoni, and C. Vergara, "The cardiovascular system: Mathematical modelling, numerical algorithms and clinical applications," *Acta Numerica,* vol. 26, pp. 365-590, 2017.

[7] https://www.rch.org.au/cardiology/heart_defects

[8] R. Jonas, "Comprehensive surgical management of congenital heart disease," *CRC press*, 2002.

[9] http://www.crimson.software

[10] https://www.ansys.com

[11] https://www.3ds.com/products-services/simulia/products/abaqus

[12] S. Patankar, "Numerical heat transfer and fluid flow," *CRC press*, 1980.

[13] H. Versteeg and W. Malalasekera, "An introduction to computational fluid dynamic: The finite volume method," *Longman,* 1995.

[14] F. Auricchio, "Computational methods in cardiovascular mechanics," *Conference Proceedings,* 2017.

[15] T. J. R. Hughes, J. A. Cottrell, and Y. Bazilevs, "Isogeometric analysis: CAD, finite elements, NURBS, exact geometry and mesh refinement," *Computer Methods in Applied Mechanics and Engineering,* vol. 194, no. 39, pp. 4135-4195, 2005.

[16] C. S. Peskin, "The immersed boundary method," *Acta Numerica,* vol. 11, pp. 479-517, 2002.

[17] M. Ariane *et al.*, "Discrete multi-physics: A mesh-free model of blood flow in flexible biological valve including solid aggregate formation," *PloS one,* vol. 12, no. 4, p. e0174795, 2017.

[18] R. C. Orth, M. J. Wallace, and M. D. Kuo, "C-arm cone-beam CT: General principles and technical considerations for use in interventional radiology," *Journal of Vascular and Interventional Radiology,* vol. 19, no. 6, pp. 814-820, 2008.

[19] M. S. Vieira, T. Hussain, and C. A. Figueroa, "Patient-specific image-based computational modeling in congenital heart disease: A clinician perspective," *Conference Proceedings,* 2015.

[20] H. G. J. Kortman, E. J. Smit, M. T. H. Oei, R. Manniesing, M. Prokop, and F. J. A. Meijer, "4D-CTA in neurovascular disease: A review," *American Journal of Neuroradiology,* vol. 36, no. 6, pp. 1026-1033, 2015.

[21] N. S. Anavekar and J. K. Oh, "Doppler echocardiography: A contemporary review," *Journal of Cardiology,* vol. 54, no. 3, pp. 347-358, 2009.

[22] P. Peng, K. Lekadir, A. Gooya, L. Shao, S. E. Petersen, and A. F. Frangi, "A review of heart chamber segmentation for structural and functional analysis using cardiac magnetic resonance imaging," *Magma (New York)*, vol. 29, pp. 155-195, 2016.

[23] P. D. Gatehouse *et al.*, "Applications of phase-contrast flow and velocity imaging in cardiovascular MRI," *European Radiology*, vol. 15, no. 10, pp. 2172-2184, 2005.

[24] P. Janani, J. Premaladha, and K. Ravichandran, "Image enhancement techniques: A study," *Indian Journal of Science and Technology*, vol. 8, no. 22, 2015.

[25] P. Gravel, G. Beaudoin, and J. A. D. Guise, "A method for modeling noise in medical images," *IEEE Transactions on Medical Imaging*, vol. 23, no. 10, pp. 1221-1232, 2004.

[26] R. Kaur, M. Chawla, N. K. Khiva, and M. D. Ansari, "Comparative analysis of contrast enhancement techniques for medical images," *Pertanika Journal of Science & Technology*, vol. 26, no. 3, 2018.

[27] H.-Y. Lee, N. C. Codella, M. D. Cham, J. W. Weinsaft, and Y. Wang, "Automatic left ventricle segmentation using iterative thresholding and an active contour model with adaptation on short-axis cardiac MRI," *IEEE Transactions on Biomedical Engineering*, vol. 57, no. 4, pp. 905-913, 2010.

[28] N. C. Codella, J. W. Weinsaft, M. D. Cham, M. Janik, M. R. Prince, and Y. Wang, "Left ventricle: automated segmentation by using myocardial effusion threshold reduction and intravoxel computation at MR imaging," *Radiology*, vol. 248, no. 3, pp. 1004-1012, 2008.

[29] http://biomedical.materialise.com/mimics

[30] www.vmtk.org

[31] D. Dillon-Murphy, A. Noorani, D. Nordsletten, and C. A. Figueroa, "Multi-modality image-based computational analysis of haemodynamics in aortic dissection," *Biomechanics and Modeling in Mechanobiology*, vol. 15, no. 4, pp. 857-876, 2016.

[32] A. Shymchenko, V. Tereshchenko, Y. Ryabov, S. Salkutsan, and A. Borovkov, "Review of the computational approaches to advanced materials simulation in accordance with modern advanced manufacturing trends," *Materials Physics & Mechanics,* vol. 32, no. 3, 2017.

[33] A. Skvortsov, "Delaunay triangulation and its applications," 2002.

[34] R. Bevan, P. Nithiarasu, R. Van Loon, I. Sazonov, H. Luckraz, and A. Garnham, "Application of a locally conservative Galerkin (LCG) method for modeling blood flow through a patient-specific carotid bifurcation," *International Journal for Numerical Methods in Fluids,* vol. 64, no. 10-12, pp. 1274-1295, 2010.

[35] I. B. Celik, U. Ghia, and P. J. Roache, "Procedure for estimation and reporting of uncertainty due to discretization in CFD applications," *Journal of fluids Engineering of the ASME,* vol. 130, no. 7, 2008.

[36] A. Sequeira, "Hemorheology: Non-Newtonian constitutive models for blood flow simulations," *Non-Newtonian Fluid Mechanics and Complex Flow,* pp. 1-44, Springer, Cham, 2018.

[37] S. N. Doost, L. Zhong, B. Su, and Y. S. Morsi, "The numerical analysis of non-Newtonian blood flow in human patient-specific left ventricle," *Computer Methods and Programs in Biomedicine,* vol. 127, pp. 232-247, 2016.

[38] D. S. Long, M. L. Smith, A. R. Pries, K. Ley, and E. R. Damiano, "Microviscometry reveals reduced blood viscosity and altered shear rate and shear stress profiles in microvessels after hemodilution," *Proceedings of the National Academy of Sciences,* vol. 101, no. 27, pp. 10060-10065, 2004.

[39] A. Arzani, "Accounting for residence-time in blood rheology models: do we really need non-Newtonian blood flow modelling in large arteries?," *Journal of The Royal Society Interface,* vol. 15, no. 146, 2018.

[40] B. M. Johnston, P. R. Johnston, S. Corney, and D. Kilpatrick, "Non-Newtonian blood flow in human right coronary arteries: steady state simulations," *Journal of biomechanics,* vol. 37, no. 5, pp. 709-720, 2004.

[41] B. M. Johnston, P. R. Johnston, S. Corney, and D. Kilpatrick, "Non-Newtonian blood flow in human right coronary arteries: transient simulations," *Journal of biomechanics,* vol. 39, no. 6, pp. 1116-1128, 2006.

[42] J. C. Weddell, J. Kwack, P. Imoukhuede, and A. Masud, "Hemodynamic analysis in an idealized artery tree: differences in wall shear stress between Newtonian and non-Newtonian blood models," *PloS one,* vol. 10, no. 4, p. e0124575, 2015.

[43] I. Freshwater, Y. Morsi, and T. Lai, "The effect of angle on wall shear stresses in a LIMA to LAD anastomosis: numerical modelling of pulsatile flow," *Proceedings of the Institution of Mechanical Engineers, Part H: Journal of Engineering in Medicine,* vol. 220, no. 7, pp. 743-757, 2006.

[44] J. Vimmr, A. Jonášová, and O. Bublík, "Numerical analysis of non-Newtonian blood flow and wall shear stress in realistic single, double and triple aorto-coronary bypasses," *International journal for numerical methods in biomedical engineering,* vol. 29, no. 10, pp. 1057-1081, 2013.

[45] V. L. Marrero, J. A. Tichy, O. Sahni, and K. E. Jansen, "Numerical study of purely viscous non-Newtonian flow in an abdominal aortic aneurysm," *Journal of biomechanical engineering,* vol. 136, no. 10, p. 101001, 2014.

[46] A. Valencia, A. Zarate, M. Galvez, and L. Badilla, "Non-Newtonian blood flow dynamics in a right internal carotid artery with a saccular aneurysm," *International Journal for Numerical Methods in Fluids,* vol. 50, no. 6, pp. 751-764, 2006.

[47] M. G. Rabby, A. Razzak, and M. M. Molla, "Pulsatile non-Newtonian blood flow through a model of arterial stenosis," *Procedia Engineering,* vol. 56, pp. 225-231, 2013.

[48] J. Ma and A. Turan, "Pulsatile non-Newtonian haemodynamics in a 3D bifurcating abdominal aortic aneurysm model," *Computer Methods in Biomechanics and Biomedical Engineering*, vol. 14, no. 8, pp. 683-694, 2011.

[49] H. Ho, A. Bartlett, and P. Hunter, "Non-Newtonian blood flow analysis for the portal vein based on a CT image," in *International MICCAI Workshop on Computational and Clinical Challenges in Abdominal Imaging*, 2012, pp. 283-291.

[50] I. Manavitehrani, P. Ebrahimi, I. Yang, S. Daly, A. Schindeler, A. Saxena, D. G. Little, D. F. Fletcher, F. Dehghani, D. S. Winlaw, "Current challenges and emergent technologies for manufacturing artificial right ventricle to pulmonary artery (RV-PA) cardiac conduits," *Submitted to Cardiovascular Engineering and Technologies.*

[51] K. S. Iyer, "The Contegra bovine jugular valved conduit: Living up to expectations?," *Annals of pediatric cardiology*, vol. 5, no. 1, pp. 34-35, 2012.

[52] A. J. Rastan *et al.*, "Bovine jugular vein conduit for right ventricular outflow tract reconstruction: evaluation of risk factors for mid-term outcome," *The Annals of thoracic surgery*, vol. 82, no. 4, pp. 1308-1315, 2006.

[53] N. Sekarski *et al.*, "Right ventricular outflow tract reconstruction with the bovine jugular vein graft: 5 years' experience with 133 patients," *The Annals of thoracic surgery*, vol. 84, no. 2, pp. 599-605, 2007.

[54] J. W. Brown, M. Ruzmetov, M. D. Rodefeld, P. Vijay, and R. K. Darragh, "Valved bovine jugular vein conduits for right ventricular outflow tract reconstruction in children: an attractive alternative to pulmonary homograft," *The Annals of thoracic surgery*, vol. 82, no. 3, pp. 909-916, 2006.

[55] T. Shinkawa, C. Chipman, T. Bozzay, X. Tang, J. M. Gossett, and M. Imamura, "Outcome of right ventricle to pulmonary artery conduit for biventricular repair," *The Annals of Thoracic Surgery*, vol. 99, no. 4, pp. 1357-1366, 2015.

[56] T. Miyazaki *et al.*, "Expanded polytetrafluoroethylene conduits and patches with bulging sinuses and fan-shaped valves in right ventricular outflow tract reconstruction: Multicenter study in Japan," *The Journal of Thoracic and Cardiovascular Surgery,* vol. 142, no. 5, pp. 1122-1129, 2011.

[57] R. Walden, G. J. L'Italien, J. Megerman, and W. M. Abbott, "Matched elastic properties and successful arterial grafting," *Archives of Surgery,* vol. 115, no. 10, pp. 1166-1169, 1980.

[58] S. Sarkar, H. J. Salacinski, G. Hamilton, and A. M. Seifalian, "The mechanical properties of infrainguinal vascular bypass grafts: Their Role in influencing patency," *European Journal of Vascular and Endovascular Surgery,* vol. 31, no. 6, pp. 627-636, 2006.

[59] S. Guhathakurta *et al.*, "Thrombogenicity studies of three different variants of processed bovine pericardium," *IRBM,* vol. 29, no. 4, pp. 223-230, 2008.

[60] A. A. Oberai, N. H. Gokhale, and G. R. Feijóo, "Solution of inverse problems in elasticity imaging using the adjoint method," *Inverse problems,* vol. 19, no. 2, p. 297, 2003.

[61] J. Boese, M. Bock, S. Schoenberg, and L. Schad, "Estimation of aortic compliance using magnetic resonance pulse wave velocity measurement," *Physics in Medicine & Biology,* vol. 45, no. 6, p. 1703, 2000.

[62] W. Sun and M. S. Sacks, "Finite element implementation of a generalized Fung-elastic constitutive model for planar soft tissues," *Biomechanics and modeling in mechanobiology,* vol. 4, no. 2-3, pp. 190-199, 2005.

[63] J. S. Soares, K. R. Feaver, W. Zhang, D. Kamensky, A. Aggarwal, and M. S. Sacks, "Biomechanical behavior of bioprosthetic heart valve heterograft tissues:

Characterization, simulation, and performance," *Cardiovascular engineering and technology*, vol. 7, no. 4, pp. 309-351, 2016.

[64] C. Chuong and Y. Fung, "Three-dimensional stress distribution in arteries," *Journal of biomechanical engineering*, vol. 105, no. 3, pp. 268-274, 1983.

[65] J. Li, X. Luo, and Z. Kuang, "A nonlinear anisotropic model for porcine aortic heart valves," *Journal of biomechanics*, vol. 34, no. 10, pp. 1279-1289, 2001.

[66] R. Zakerzadeh, M.-C. Hsu, and M. S. Sacks, "Computational methods for the aortic heart valve and its replacements," *Expert Review of Medical Devices*, vol. 14, no. 11, pp. 849-866, 2017.

[67] A. Mahmoud, A. El-Barkouky, H. Farag, J. Graham, and A. Farag, "A non-invasive method for measuring blood flow rate in superficial veins from a single thermal image," *Proceedings of the IEEE Conference on Computer Vision and Pattern Recognition Workshops*, 2013, pp. 354-359.

[68] M. R. Nelson, J. Stepanek, M. Cevette, M. Covalciuc, R. T. Hurst, and A. J. Tajik, "Noninvasive measurement of central vascular pressures with arterial tonometry: Clinical revival of the pulse pressure waveform?," *Mayo Clinic Proceedings*, vol. 85, no. 5, pp. 460-472, 2010.

[69] C.-H. Chen *et al.*, "Estimation of central aortic pressure waveform by mathematical transformation of radial tonometry pressure: validation of generalized transfer function," *Circulation*, vol. 95, no. 7, pp. 1827-1836, 1997.

[70] I. E. Vignon-Clementel, C. A. Figueroa, K. E. Jansen, and C. A. Taylor, "Outflow boundary conditions for 3D simulations of non-periodic blood flow and pressure fields in deformable arteries," *Computer Methods in Biomechanics and Biomedical Engineering*, vol. 13, no. 5, pp. 625-640, 2010.

[71] S. Pirola, Z. Cheng, O. A. Jarral, D. P. O'Regan, J. R. Pepper, T. Athanasiou and X. Y. Xu, "On the choice of outlet boundary conditions for patient-specific analysis of

aortic flow using computational fluid dynamics," *Journal of Biomechanics,* vol. 60, p. 15-21, 2017.

[72] P. Maurovich-Horvat, M. Ferencik, S. Voros, B. Merkely, and U. Hoffmann, "Comprehensive plaque assessment by coronary CT angiography," *Nature Reviews Cardiology,* vol. 11, p. 390, 2014.

[73] S. C. Shadden and S. Hendabadi, "Potential fluid mechanic pathways of platelet activation," *Biomechanics and Modeling in Mechanobiology,* journal article vol. 12, no. 3, pp. 467-474, 2013.

[74] J. F. LaDisa, A. C. Figueroa, I. E. Vignon-Clementel, H. Jin Kim, N. Xiao, L. M. Elwein, F. P. Chan, J. A. Feinstein and C. A. Taylor, "Computational simulations for sortic coarctation: representative results from a sampling of patients," *Journal of Biomechanical Engineering,* vol. 133, 2011.

[75] D. A. de Zélicourt and V. Kurtcuoglu, "Patient-specific surgical planning, where do we stand? The example of the Fontan procedure," *Annals of Biomedical Engineering,* vol. 44, no. 1, pp. 174-186, 2016.

[76] L. P. Dasi, K. Pekkan, H. D. Katajima, and A. P. Yoganathan, "Functional analysis of Fontan energy dissipation," *Journal of Biomechanics,* vol. 41, no. 10, pp. 2246-2252, 2008.

[77] N. Lee, M. D. Taylor, and R. K. Banerjee, "Right ventricle-pulmonary circulation dysfunction: a review of energy-based approach," *Biomedical Engineering Online,* vol. 14, no. 1, p. S8, 2015.

[78] C. M. Lawley, K. M. Broadhouse, F. M. Callaghan, D. S. Winlaw, G. A. Figtree, and S. M. Grieve, "4D flow magnetic resonance imaging: role in pediatric congenital heart disease," *Asian Cardiovascular and Thoracic Annals,* vol. 26, no. 1, pp. 28-37, 2018.

[79] F. M. Callaghan, J. Karkouri, K. Broadhouse, M. Evin, D. F. Fletcher, and S. M. Grieve, "Thoracic aortic aneurysm: 4D flow MRI and computational fluid dynamics model,"

Computer Methods in Biomechanics and Biomedical Engineering, vol. 18, sup1, pp. 1894-1895, 2015.

[80] E. L. Bove *et al.*, "Use of mathematic modeling to compare and predict hemodynamic effects of the modified Blalock-Taussig and right ventricle-pulmonary artery shunts for hypoplastic left heart syndrome," *The Journal of Thoracic and Cardiovascular Surgery*, vol. 136, no. 2, pp. 312-320, 2008.

[81] P. M. Trusty *et al.*, "Fontan surgical planning: Previous accomplishments, current challenges, and future directions," *Journal of Cardiovascular Translational Research*, journal article vol. 11, no. 2, pp. 133-144, 2018.

[82] W. Jacek *et al.*, "The effects of graft geometry on the patency of a systemic-to-pulmonary shunt: A computational fluid dynamics study," *Artificial Organs*, vol. 29, no. 8, pp. 642-650, 2005.

[83] D. D. Soerensen *et al.*, "Introduction of a new optimized total cavopulmonary connection," *The Annals of Thoracic Surgery*, vol. 83, no. 6, pp. 2182-2190.

[84] D. D. Zelicourt, "A mechanical fluid assessment of anatomical models of the total cavopulmonary connection (TCPC) (MS thesis)," *Atlanta, GA: Georgia Institute of Technology.*, 2004.

[85] W. Yang, J. A. Feinstein, S. C. Shadden, I. E. Vignon-Clementel, and A. L. Marsden, "Optimization of a Y-graft design for improved hepatic flow distribution in the Fontan circulation," *Journal of Biomechanical Engineering*, vol. 135, no. 1, pp. 011002-011002-12, 2012.

[86] W. Yang, F. P. Chan, V. M. Reddy, A. L. Marsden, and J. A. Feinstein, "Flow simulations and validation for the first cohort of patients undergoing the Y-graft Fontan procedure," *The Journal of Thoracic and Cardiovascular Surgery*, vol. 149, no. 1, pp. 247-255.

[87] T. M. J. van Bakel, K. D. Lau, J. Hirsch-Romano, S. Trimarchi, A. L. Dorfman, and C. A. Figueroa, "Patient-Specific modeling of hemodynamics: Supporting surgical planning in a Fontan circulation correction," *Journal of Cardiovascular Translational Research,* 2018.

[88] A. L. Marsden *et al.*, "Evaluation of a novel Y-shaped extracardiac Fontan baffle using computational fluid dynamics," *The Journal of Thoracic and Cardiovascular Surgery,* vol. 137, no. 2, pp. 394-403, 2009.

[89] E. Tang and A. P. Yoganathan, "Optimizing hepatic flow distribution with the Fontan Y-graft: Lessons from computational simulations," *The Journal of Thoracic and Cardiovascular Surgery,* vol. 149, no. 1, pp. 255-256, 2015.

[90] M. Toloui, A. Nikparto, B. Firoozabadi and M. S. Saidi, "Numerical simulations of haemodynamic factors and hyperelastic circumferential strain/stress in the ideal and healthy-patient-specific carotid bifurcations for different rheological models," *International Journal of Biomedical Engineering and Technology,* vol. 6, pp. 387-412, 2011.

[91] D. Siallagan *et al.*, "Virtual surgical planning, flow simulation, and 3-dimensional electrospinning of patient-specific grafts to optimize Fontan hemodynamics," *The Journal of Thoracic and Cardiovascular Surgery,* vol. 155, no. 4, pp. 1734-1742.

[92] C. Capelli *et al.*, "Patient-specific simulations for planning treatment in congenital heart disease," *Interface Focus,* vol. 8, no. 1, 2018.

[93] G. D. Dangas, J. I. Weitz, G. Giustino, R. Makkar, and R. Mehran, "Prosthetic heart valve thrombosis," *Journal of the American College of Cardiology,* vol. 68, no. 24, pp. 2670-2689, 2016.

[94] P. D. Morris *et al.*, "Computational fluid dynamics modelling in cardiovascular medicine," *Heart,* vol. 102, no. 1, pp. 18-28, 2016.

[95] M. Xenos *et al.*, "Device Thrombogenicity Emulator (DTE)--Design optimization methodology for cardiovascular devices: A study in two bileaflet MHV designs," *Journal of Biomechanics,* vol. 43, no. 12, pp. 2400-2409, 2010.

[96] http://www.parameterz.com/sites/pulmonary-arteries

[97] M. Cantinotti *et al.*, "Nomograms for two-dimensional echocardiography derived valvular and arterial dimensions in Caucasian children," *Journal of Cardiology,* vol. 69, no. 1, pp. 208-215, 2017.

[98] F. Kabinejadian and D. N. Ghista, "Compliant model of a coupled sequential coronary arterial bypass graft: Effects of vessel wall elasticity and non-Newtonian rheology on blood flow regime and hemodynamic parameters distribution," *Medical Engineering & Physics,* vol. 34, no. 7, pp. 860-872, 2012.

[99] J. R. Womersley, "Method for the calculation of velocity, rate of flow and viscous drag in arteries when the pressure gradient is known," *The Journal of Physiology,* vol. 127, no. 3, pp. 553-563, 1955.

[100] R. Bird, R. Armstrong, and O. Hassager, "Dynamics of Polymeric Liquids," *Wiley,* vol. 1, 1987.

[101] H. P. Gutgesell, "Pulmonary valve insufficiency: Malignant or benign?," *Journal of the American College of Cardiology,* 1992.

[102] A. Kadner, I. I. Tulevski, U. Bauersfeld, R. Prêtre, E. R. Valsangiacomo-Buechel, and A. Dodge-Khatami, "Chronic pulmonary valve insufficiency after repaired tetralogy of Fallot: diagnostics, reoperations and reconstruction possibilities," *Expert review of cardiovascular therapy,* vol. 5, no. 2, pp. 221-230, 2007.

[103] C. M. Mery *et al.*, "Risk factors for development of endocarditis and reintervention in patients undergoing right ventricle to pulmonary artery valved conduit placement," *The Journal of thoracic and cardiovascular surgery,* vol. 151, no. 2, pp. 432-441, 2016.

[104] B. H. Morray *et al.*, "Multicenter experience evaluating transcatheter pulmonary valve replacement in bovine jugular vein (Contegra) right ventricle to pulmonary artery conduits," *Circulation: Cardiovascular Interventions,* vol. 10, no. 6, p. e004914, 2017.

[105] I. Manavitehrani, P. Ebrahimi, T. Y. Le, S. Daly, Y. Wang, P. K. Maitz, A. Schindeler, D. G. Little, D. F. Fletcher, F. Dehghani, D. S. Winlaw, "Engineering a biodegradable elastomer that mimics the properties of pulmonary artery," *Submitted to ScienceAdvances*.

[106] N. Huebsch and D. J. Mooney, "Inspiration and application in the evolution of biomaterials," *Nature,* vol. 462, no. 7272, p. 426, 2009.

[107] M. W. Laschke and M. D. Menger, "Prevascularization in tissue engineering: current concepts and future directions," *Biotechnology advances,* vol. 34, no. 2, pp. 112-121, 2016.

[108] C. E. Stowell and Y. Wang, "Quickening: Translational design of resorbable synthetic vascular grafts," *Biomaterials,* 2018.

[109] J. D. Drews, H. Miyachi, and T. Shinoka, "Tissue-engineered vascular grafts for congenital cardiac disease: clinical experience and current status," *Trends in cardiovascular medicine,* 2017.

[110] T. Shinoka, "What is the best material for extracardiac Fontan operation?," *The Journal of thoracic and cardiovascular surgery,* vol. 153, no. 6, pp. 1551-1552, 2017.

[111] T. Fukunishi *et al.*, "Preclinical study of patient-specific cell-free nanofiber tissue-engineered vascular grafts using 3-dimensional printing in a sheep model," *The Journal of thoracic and cardiovascular surgery,* vol. 153, no. 4, pp. 924-932, 2017.

[112] T. Sugiura *et al.*, "Fast-degrading bioresorbable arterial vascular graft with high cellular infiltration inhibits calcification of the graft," *Journal of vascular surgery,* vol. 66, no. 1, pp. 243-250, 2017.

[113] I. Manavitehrani, A. Fathi, Y. Wang, P. K. Maitz, and F. Dehghani, "Reinforced poly (propylene carbonate) composite with enhanced and tunable characteristics, an alternative for poly (lactic acid)," *ACS applied materials & interfaces,* vol. 7, no. 40, pp. 22421-22430, 2015.

[114] I. Manavitehrani, A. Fathi, H. Badr, S. Daly, A. Negahi Shirazi, and F. Dehghani, "Biomedical applications of biodegradable polyesters," *Polymers,* vol. 8, no. 1, p. 20, 2016.

[115] I. Manavitehrani *et al.*, "Fabrication of a biodegradable implant with tunable characteristics for bone implant applications," *Biomacromolecules,* vol. 18, no. 6, pp. 1736-1746, 2017.

[116] S. Spoljaric and J. Seppälä, "One-pot, mouldable, thermoplastic resins from poly (propylene carbonate) and poly (caprolactone triol)," *RSC Advances,* vol. 6, no. 41, pp. 34977-34986, 2016.

[117] D. V. Mistura, A. D. Messias, E. A. Duek, and M. A. Duarte, "Development, characterization, and cellular adhesion of poly (l-Lactic Acid)/Poly (caprolactone triol) membranes for potential application in bone tissue regeneration," *Artificial organs,* vol. 37, no. 11, pp. 978-984, 2013.

[118] M. A. T. Duarte, A. C. Motta, and E. A. d. R. Duek, "Mechanical properties of membranes of poly (L-co-DL-lactic acid) with Poly (caprolactone triol) and study in vivo," *International Journal of Polymer Science,* 2014.

[119] Z. Li, Z. Zhang, K. L. Liu, X. Ni, and J. Li, "Biodegradable hyperbranched amphiphilic polyurethane multiblock copolymers consisting of poly (propylene glycol), poly (ethylene glycol), and polycaprolactone as in situ thermogels," *Biomacromolecules,* vol. 13, no. 12, pp. 3977-3989, 2012.

[120] H. Daemi, S. Rajabi-Zeleti, H. Sardon, M. Barikani, A. Khademhosseini, and H. Baharvand, "A robust super-tough biodegradable elastomer engineered by supramolecular ionic interactions," *Biomaterials,* vol. 84, pp. 54-63, 2016.

[121] B. Nohra, L. Candy, J.-F. o. Blanco, C. Guerin, Y. Raoul, and Z. Mouloungui, "From petrochemical polyurethanes to biobased polyhydroxyurethanes," *Macromolecules,* vol. 46, no. 10, pp. 3771-3792, 2013.

[122] Y. Schellekens *et al.,* "Tin-free catalysts for the production of aliphatic thermoplastic polyurethanes," *Green Chemistry,* vol. 16, no. 9, pp. 4401-4407, 2014.

[123] N. Masoumi *et al.,* "Tri-layered elastomeric scaffolds for engineering heart valve leaflets," *Biomaterials,* vol. 35, no. 27, pp. 7774-7785, 2014.

[124] A. Hasan *et al.,* "Biomechanical properties of native and tissue engineered heart valve constructs," *Journal of biomechanics,* vol. 47, no. 9, pp. 1949-1963, 2014.

[125] J. Alastruey *et al.,* "Pulse wave propagation in a model human arterial network: Assessment of 1-D visco-elastic simulations against in vitro measurements," *Journal of Biomechanics,* vol. 44, no. 12, pp. 2250-2258, 2011.

[126] S. Mohammadi *et al.,* "Surgery for right ventricle to pulmonary artery conduit obstruction: risk factors for further reoperation," *European Journal of Cardio-Thoracic Surgery,* vol. 28, no. 2, pp. 217-222, 2005.

[127] Y. Zhang, Y. Bazilevs, S. Goswami, C. L. Bajaj, and T. J. R. Hughes, "Patient-specific vascular NURBS modeling for Isogeometric analysis of blood flow," *Computer methods in applied mechanics and engineering,* vol. 196, no. 29-30, pp. 2943-2959, 2007.

Appendix A

The following MATLAB code was used to obtain a smooth approximation of the velocity that can be utilised as inlet boundary condition.

```
syms n t
% Defining the the triangular velocity
T0=Period;
Endtime=4*T0;
w0=2*pi/T0;
d1=Time interval 1 (d1 in Figure 3.8);
d2=Time interval 2 (d2 in Figure 3.8);
d3=Time interval 3 (d3 in Figure 3.8);
d4=Time interval 4 (d4 in Figure 3.8);
vpos=Peak positive velocity;
vneg=Peak negative velocity;
n=1:6;
%Caluculating the Fourier series
a0=(1/T0)*(int((vpos/d1)*t,t,0,d1) + int(vpos-(vpos/d2)*(t-d1), t, d1, (d1+d2)) +
int((vneg/d3)*(t-(d1+d2)), t, (d1+d2), (d1+d2+d3)) + int(vneg-(vneg/d3)*(t (d1+d2+d3)), t,
(d1+d2+d3), (d1+d2+d3+d4)));

an=(2/T0)*(int((vpos/d1)*t*cos(n*w0*t),t,0,d1) + int((vpos-(vpos/d2)*(t-d1))*cos(n*w0*t),
t, d1, (d1+d2)) + int((vneg/d3)*(t-(d1+d2))*cos(n*w0*t), t, (d1+d2), (d1+d2+d3)) +
int((vneg-(vneg/d3)*(t-(d1+d2+d3)))*cos(n*w0*t), t, (d1+d2+d3), (d1+d2+d3+d4)));

bn=(2/T0)*(int((vpos/d1)*t*sin(n*w0*t),t,0,d1) + int((vpos-(vpos/d2)*(t-d1))*sin(n*w0*t), t,
d1, (d1+d2)) + int((vneg/d3)*(t-(d1+d2))*sin(n*w0*t), t, (d1+d2), (d1+d2+d3)) + int((vneg-
(vneg/d3)*(t-(d1+d2+d3)))*sin(n*w0*t), t, (d1+d2+d3), (d1+d2+d3+d4)));
```

```
%Plotting

figure;

xlabel('Time (s)', 'Fontsize', 14 )

ylabel('Velocity (m/s)', 'Fontsize', 14)

x=0 : 0.01 :Endtime;

f = @(x) [(vpos/d1)*x.*(0<=x & x<=d1) + (vpos-(vpos/d2)*(x-d1)).*(d1<x & x<=(d1+d2)) +
(vneg/d3)*(x-(d1+d2)).*((d1+d2)<x & x<=(d1+d2+d3)) + (vneg-(vneg/d4)*(x-
(d1+d2+d3))).*((d1+d2+d3)<x & x<=(d1+d2+d3+d4))];

pf= @(x) [f(mod(x,T0))];

line(x,pf(x),'color','b', 'linewidth', 0.5)

line(x, a0 + an(1)*cos(x*2*pi/T0) + bn(1)*sin(x*2*pi/T0), 'color', 'g', 'linewidth', 0.5)

line(x, a0 + an(1)*cos(x*2*pi/T0) + bn(1)*sin(x*2*pi/T0) + an(2)*cos(2*x*2*pi/T0) +
bn(2)*sin(2*x*2*pi/T0), 'color', 'm', 'linewidth', 0.5)

line(x, a0 + an(1)*cos(x*2*pi/T0) + bn(1)*sin(x*2*pi/T0) + an(2)*cos(2*x*2*pi/T0) +
bn(2)*sin(2*x*2*pi/T0) + an(3)*cos(3*x*2*pi/T0) + bn(3)*sin(3*x*2*pi/T0), 'color', 'k',
'linewidth', 0.5)

line(x, a0 + an(1)*cos(x*2*pi/T0) + bn(1)*sin(x*2*pi/T0) + an(2)*cos(2*x*2*pi/T0) +
bn(2)*sin(2*x*2*pi/T0) + an(3)*cos(3*x*2*pi/T0) + bn(3)*sin(3*x*2*pi/T0) +
an(4)*cos(4*x*2*pi/T0) + bn(4)*sin(4*x*2*pi/T0), 'color', 'r', 'linewidth', 0.5)

line(x, a0 + an(1)*cos(x*2*pi/T0) + bn(1)*sin(x*2*pi/T0) + an(2)*cos(2*x*2*pi/T0) +
bn(2)*sin(2*x*2*pi/T0) + an(3)*cos(3*x*2*pi/T0) + bn(3)*sin(3*x*2*pi/T0) +
an(4)*cos(4*x*2*pi/T0) + bn(4)*sin(4*x*2*pi/T0) + an(5)*cos(5*x*2*pi/T0) +
bn(5)*sin(5*x*2*pi/T0), 'color', 'y', 'linewidth', 0.5)

line(x, a0 + an(1)*cos(x*2*pi/T0) + bn(1)*sin(x*2*pi/T0) + an(2)*cos(2*x*2*pi/T0) +
bn(2)*sin(2*x*2*pi/T0) + an(3)*cos(3*x*2*pi/T0) + bn(3)*sin(3*x*2*pi/T0) +
an(4)*cos(4*x*2*pi/T0) + bn(4)*sin(4*x*2*pi/T0) + an(5)*cos(5*x*2*pi/T0) +
bn(5)*sin(5*x*2*pi/T0) + an(6)*cos(6*x*2*pi/T0) + bn(6)*sin(6*x*2*pi/T0), 'color', 'c',
'linewidth', 0.5)

xlim([0, Endtime])

legend({'Triangular wave', 'Fourier n=1', 'Fourier n=2', 'Fourier n=3', 'Fourier
n=4'},'Fontsize', 12 )

grid on

legend()
```

Appendix B

The calculation of the energy dissipation via the mechanical energy equation is described in this Appendix. To this end, starting from the differential form of the conservation of momentum equation

Equation C.1: $\frac{\partial \rho \boldsymbol{u}}{\partial t} + \nabla \cdot (\rho \boldsymbol{u} \otimes \boldsymbol{u}) = -\nabla p + \nabla \cdot \boldsymbol{\tau} + \rho \mathbf{g}$

and taking the dot product with the velocity vector $\boldsymbol{u}$, an equation for conservation of mechanical energy was obtained:

Equation C.2: $\boldsymbol{u} \cdot \left(\frac{\partial \rho \boldsymbol{u}}{\partial t} + \nabla \cdot (\rho \boldsymbol{u} \otimes \boldsymbol{u}) = -\nabla p + \nabla \cdot \boldsymbol{\tau} + \rho \mathbf{g}\right)$

This can be simplified to

Equation C.3: $\frac{\partial \frac{1}{2} \rho u^2}{\partial t} + \nabla \cdot \left(\rho \boldsymbol{u} \frac{1}{2} u^2\right) = -\boldsymbol{u} \cdot \nabla p + \boldsymbol{u} \cdot \nabla \cdot \boldsymbol{\tau} + \rho \boldsymbol{u} \cdot \mathbf{g}$

By manipulating the stress and pressure terms, equations 4.7 and 4.8 are acquired

Equation C.4: $\boldsymbol{u} \cdot \nabla p = \nabla \cdot (p \boldsymbol{u}) - p \nabla \cdot \boldsymbol{u}$

Equation C.5: $\boldsymbol{u} \cdot \nabla \cdot \boldsymbol{\tau} = \nabla \cdot (\boldsymbol{\tau} \boldsymbol{u}) - \boldsymbol{\tau} : \nabla \boldsymbol{u}$

If Φ_v is defined as $\boldsymbol{\tau} : \boldsymbol{\nabla u}$, using equation 4.6-4.8 results in

Equation C.6: $\frac{\partial \frac{1}{2} \rho u^2}{\partial t} + \nabla \cdot \left(\rho \boldsymbol{u} \frac{1}{2} u^2\right) = -(\nabla \cdot (p \boldsymbol{u}) - p \nabla \cdot \boldsymbol{u}) + \nabla \cdot (\boldsymbol{\tau} \boldsymbol{u}) - \Phi_v + \rho \boldsymbol{u} \cdot \mathbf{g}$

The viscous energy dissipation in Cartesian form is given by

Equation C.7: $\Phi_v = 2\mu \left[\left(\frac{\partial u_x}{\partial x}\right)^2 + \left(\frac{\partial u_y}{\partial y}\right)^2 + \left(\frac{\partial u_z}{\partial z}\right)^2\right] + \left(\left(\frac{\partial u_y}{\partial x}\right) + \left(\frac{\partial u_x}{\partial y}\right)\right)^2 + \left(\left(\frac{\partial u_z}{\partial y}\right) + \left(\frac{\partial u_y}{\partial z}\right)\right)^2 + \left(\left(\frac{\partial u_x}{\partial z}\right) + \left(\frac{\partial u_z}{\partial x}\right)\right)^2$

Integration of the mechanical energy conservation equation over the fluid volume and assuming *incompressible flow* in the *absence of gravity* gives

Equation C.8: $\frac{d}{dt}\int_{V_c(t)}\frac{1}{2}\rho u^2 dV + \int_{S_c(t)}\frac{1}{2}\rho u^2(\boldsymbol{u}\cdot\boldsymbol{n})\,dS =$

$$\int_{S_c(t)}(-p\boldsymbol{n})\cdot\boldsymbol{u}\,dS + \int_{S_c(t)}(\boldsymbol{\tau}\cdot\boldsymbol{n})\cdot\boldsymbol{u}\,dS - \int_{V_c(t)}\Phi_v\,dV$$

Assuming the flow domain is unchanging with time and has constant volume of *V*, time integrating these equations over a complete oscillatory cycle of duration T to obtain the total energy dissipation per cycle

Equation C.9: $\int_0^T\int_V \Phi_v\;dVdt = -\left[\int_V\frac{1}{2}\rho u^2 dV\right]_0^T + \int_0^T\int_{S_c(t)}(\boldsymbol{\tau}\cdot\boldsymbol{n})\cdot\boldsymbol{u}\,dS -$

$$\int_0^T\int_A p(\boldsymbol{n}.\boldsymbol{u})\,dS - \int_0^T\int_{S_c(t)}\frac{1}{2}\rho u^2(\boldsymbol{u}\cdot\boldsymbol{n})\,dS$$

Given a periodic velocity profile is being introduced the first two terms on the right-hand side must be zero, so the total energy dissipation is obtained by integrating the other two terms over a cardiac cycle. These terms can be defined in the CFD setup and will be explicitly evaluated in simulations and no approximation is required.

Appendix C

In this Appendix Effective WSS and energy dissipation introduced in Section 3.7 are used to benchmark the performance of the modified geometries against a straight pipe. To this end, the abovementioned parameters were evaluated using the velocity data of each patient with three straight pipes as described below, and their values were compared with the values obtained for modified geometries.

The minimum distance between inlet and outlet of the conduit, which is the minimum distance between right ventricle to pulmonary artery, was measured and set for the length of the first straight pipe. However, the minimum distance is not practically feasible, since it passes through the heart. Hence, a second straight pipe with the length equal to the length of the centreline of the modified conduit was proposed, this is a more realistic model.

Also, through the study, it was found that longer lengths result in a small increase in energy dissipation, but a larger decrease in WSS. Hence, it was concluded that with the same diameter, the conduit with the longer length, will have a better overall performance. With this in mind, the last straight pipe was characterised with the higher length (length of centreline of the modified geometry) and the maximum diameter of 22 mm (as mentioned before, this is the maximum diameter that is clinically feasible).

From the results shown in Table B.1 it can be seen that the diameter of the conduit has a significant effect on its performance. Increasing the diameter remarkably reduces WSS and energy dissipation. However, there are two main criteria that limit the size of the conduit: one is the ability of the body to accommodate the conduit, and the other is pulmonary edema. Too large conduit can result in pulmonary edema, which is a condition caused by excess fluid in the lungs. The fluid accumulates in several air sacs in the lungs and lead to difficulty in breathing. This situation can be fatal if medical attention is not sought. Thus, although from a

computational perspective, larger diameters are more appealing, clinical considerations made in Section 3.3 lead to a more suitable size. In brief, the second straight pipe is the most realistic and the third will have the minimum WSS and energy dissipation.

In cases where a large decrease in WSS and energy dissipation through the straight pipe compared with the modified geometry is noticed, running the simulations with an upsized modified conduit is suggested. The results can be shared with clinicians and they can decide if the improvement in the performance is worth the risks an oversized conduit may bring about.

Table C.1 Comparison of the performance of the straight pipe models with the modified geometries for all patients.

	Model	Length (mm)	Diameter (mm)	Change in Effective WSS (%)	Change in energy dissipation (%)
Patient A	**Pipe 1**	50	22	-14	57
	Pipe 2	66	22	-19	61
Patient B	**Pipe 1**	25	19	2	-36
	Pipe 2	43	19	-8	-32
	Pipe 3	43	22	-36	-60
Patient C	**Pipe 1**	20	22	12	12
	Pipe 2	30	22	2	16
Patient D	**Pipe 1**	20	18	7	-20
	Pipe 2	40	18	-6	-15
	Pipe 3	40	22	-42	-61
Patient E	**Pipe 1**	20	18	7	-20
	Pipe 2	40	18	-6	-15
	Pipe 3	40	22	-42	-61
Patient F	**Pipe 1**	50	17	-23	-47
	Pipe 2	80	17	-27	-43
	Pipe 3	80	22	-57	-80